

Uncertainty quantification in model discovery by distilling interpretable material constitutive models from Gaussian process posteriors

David Anton^{a,*}, Henning Wessels^a, Ulrich Römer^b, Alexander Henkes^c,
Jorge-Humberto Urrea-Quintero^a

^a*Technische Universität Braunschweig, Institute of Applied Mechanics, Pockelsstraße
3, 38106, Braunschweig, Germany*

^b*Technische Universität Braunschweig, Institute for Acoustics and Dynamics, Langer Kamp
19, 38106, Braunschweig, Germany*

^c*Eidgenössische Technische Hochschule Zürich, Computational Mechanics
Group, Tannenstrasse 3, 8092, Zürich, Switzerland*

Abstract

Constitutive model discovery refers to the task of identifying an appropriate model structure, usually from a predefined model library, while simultaneously inferring its material parameters. The data used for model discovery are measured in mechanical tests and are thus inevitably affected by noise which, in turn, induces uncertainties. Previously proposed methods for uncertainty quantification in model discovery either require the selection of a prior for the material parameters, are restricted to linear coefficients of the model library or are limited in the flexibility of the inferred parameter probability distribution. We therefore propose a partially Bayesian framework for uncertainty quantification in model discovery that does not require prior selection for the material parameters and also allows for the discovery of constitutive models with inner-non-linear parameters: First, we augment the available stress-deformation data with a Gaussian process. Second, we approximate the parameter distribution by a normalizing flow, which allows for modeling complex joint distributions. Third, we distill the parameter distribution by matching the distribution of stress-deformation functions induced by the parameters with the Gaussian process posterior. Fourth, we perform a Sobol' sensitivity analysis to obtain a sparse and interpretable model. We demonstrate the capability of our framework for both isotropic and experimental anisotropic data.

Keywords: Uncertainty quantification, Model discovery, Model distillation, Normalizing flows, Gaussian processes, Neural networks

*Corresponding author

Email addresses: d.anton@tu-braunschweig.de (David Anton),
h.wessels@tu-braunschweig.de (Henning Wessels), u.roemer@tu-braunschweig.de (Ulrich Römer), ahenke@ethz.ch (Alexander Henkes), jorge.urrea-quintero@tu-braunschweig.de (Jorge-Humberto Urrea-Quintero)

1. Introduction

In order to unlock the predictive capabilities of continuum mechanics, it is essential to discover constitutive models for the material of interest that relate stress to strain and possibly other physical quantities. The conventional approach to material modeling involves a two-step process. First, a constitutive model with fixed structure is formulated, typically expressed in terms of invariant or tensor-basis representations, and constrained to satisfy thermodynamic requirements [1, 2]. Second, the degrees of freedom of the constitutive model, also known as material parameters, are calibrated using measurement data [3, 4]. For an overview of calibration methods, the reader is referred to, e.g., [5]. However, the predictive capability of a calibrated model is decisively dependent on the suitability of the chosen constitutive model [2, 4, 6].

Constitutive model discovery: The idea of constitutive model discovery is to find a suitable structure for the constitutive model and to infer the material parameters at the same time [7]. In this process, the constitutive model is usually selected as a reduced subset of a previously defined model library of candidate terms such as, e.g., a combination of generalized Mooney-Rivlin [8] and generalized Ogden [9] models. The efficient unsupervised constitutive law identification and discovery (EUCLID) framework pioneered this approach in the discovery of interpretable hyperelastic constitutive models in an unsupervised setting [7, 10, 11]. EUCLID has also been extended to inelastic materials [12, 13, 14]. Further attempts utilize artificial neural networks (NNs) as constitutive model. Although purely data-driven approaches are generally flexible, they lack interpretability and can show non-physical and unstable material behavior [15]. To prevent non-physical behavior, recent developments incorporate physical constraints, such as thermodynamic consistency, polyconvexity, objectivity and material symmetry, directly into the NN architecture [16, 17, 18, 19, 20, 21].

In addition to satisfying fundamental physical constraints, constitutive artificial neural networks (CANNs) have been proposed to enable interpretability of the NN-based constitutive model by assigning the weights of the NN a physical meaning [22, 23, 24, 25, 26]. CANNs can also be interpreted as model libraries including linear and non-linear candidate terms. Recently, CANNs have also been combined with large language models (LLMs) [27]. There are also hybrid approaches, such as constitutive Kolmogorov-Arnold networks (CKANs) [28, 29], that aim to combine the accuracy of purely data-driven methods with the interpretability of symbolic expressions.

Uncertainty quantification in model discovery: The data used to find a suitable model are measured in mechanical tests and thus are corrupted by noise, which directly introduces uncertainties. In addition, stress-deformation measurements, in particular, may be sparse. Data sparsity, in turn, also increases uncertainty [30]. When applying deterministic methods to the experi-

mental data, uncertainty in the discovered model terms or corresponding material parameters is not quantified. Instead, we obtain information reduced to deterministic parameter values, which may lead to a false sense of confidence.

In a Bayesian statistical setting, the material parameters are treated as random variables with a prior distribution. This prior distribution is then updated to the posterior distribution according to Bayes' law by conditioning it on the data [31]. A central element and, at the same time, a prerequisite for using Bayes' law is the formulation of the prior. In [32], the Bayesian-EUCLID framework was proposed to discover hyperelastic constitutive models with uncertainties. The authors used a hierarchical Bayesian model with sparsity-promoting priors and a Markov chain Monte Carlo (MCMC) sampling strategy. Similarly to EUCLID, there is also a Bayesian statistical variant for CANNs [33], known as Bayesian CANNs. Instead of optimizing for a deterministic value of the network weights, which correspond to the material parameters, the authors used variational Bayesian inference to learn the probability density of the weights in the output layer. However, in this approach, the parameters considered uncertain lack physical interpretability and are assumed to be independently distributed.

Bayesian approaches to uncertainty quantification (UQ) for model discovery are complicated by the need to formulate informative priors. Both the large number of material parameters and the fact that the relevance of parameters is unknown before the model discovery process pose significant challenges. In a related context, UQ for learning dynamical systems faces similar difficulties and priors are mainly used to enforce sparsity, see, e.g., [34]. Similarly, for Bayesian neural networks (BNNs), the large number of parameters makes it practically impossible to formulate a well-informed prior for individual parameters [35].

Compared to Bayesian CANNs, Gaussian CANNs [36] are more interpretable and do not require the selection of a prior for the random material parameters. In addition, Gaussian CANNs allow the weights to be correlated. However, the random weights that again correspond to the material parameters are restricted to be Gaussian distributed. Furthermore, only the linear material parameters of the model library are assumed to be random variables, while the non-linear parameters are considered deterministic.

To the best of the authors' knowledge, the above-mentioned contributions are the only ones in the literature to date that have proposed methods for the statistical discovery of interpretable material constitutive models. For the sake of completeness, we would like to point out that other statistical methods have also been developed in recent years. These include, among others, a Gaussian process (GP)-based constitutive modeling framework [37] or generative models for hyperelastic strain energy density functions (SEFs) based on physics-informed probabilistic diffusion fields [38]. However, these methods do not yield sparse and interpretable constitutive models.

Our framework: Motivated by the limitations of the methods mentioned above, we propose a new four-step framework for UQ in the discovery of interpretable constitutive models that is partially Bayesian:

- First, we augment the available stress-deformation data collected in mechanical tests with a GP as one of the authors has proposed in [39] in the context of surrogate modeling.
- Second, we approximate the probability distribution of the material parameters in the model library by a normalizing flow (NF) [40, 41], which allows modeling complex and high-dimensional joint distributions [42, 43]. The distribution of material parameters, in turn, induces a distribution over stress-deformation functions through the structure of the model library for the SEF.
- Third, we distill the distribution of the material parameters by matching the distribution over stress-deformation functions induced by them with the target distribution given by the GP posterior. Therefore, we minimize the Wasserstein-1 distance between the two distributions with respect to the NF parameters.
- Fourth, we perform a Sobol’ sensitivity analysis [44], which finally yields sparse and interpretable constitutive models.

The framework we propose contributes to the current state of UQ in model discovery as follows:

- The framework is only partially Bayesian and does not require the selection of an informative prior probability distribution for the material parameters. Instead, we only need a GP prior which can be learned from the available stress-deformation data. This is particularly appealing because model discovery is motivated by the fact that the relevance of the material parameters and even the structure of the constitutive model are not known a priori.
- NFs offer a high degree of flexibility for modeling the joint probability distribution of material parameters compared to simpler distributions, such as multivariate Gaussian distributions.
- The selection of the relevant model terms is based on their total-order Sobol’ sensitivity. The sensitivity analysis provides us with an interpretable selection criterion and further insights into the selection process.

The framework is inspired by the work in [45] which deals with determining suitable priors for the parameters of BNNs. Their investigations start with the observation that the functional priors of BNNs are much easier to interpret and control than a prior defined directly for the NN parameters. Therefore, they propose to match the functional prior of the BNN with a target GP prior by minimizing their Wasserstein-1 distance with respect to the distributional parameters of the prior ansatz for the NN weights. Two key differences between our framework and the one proposed in [45] are that we use GP posteriors as target distributions while they used priors and that we minimize the Wasserstein-1

distance to distill the distribution over parameters of a model library instead of the weights of a BNN that lack interpretability.

Finally, we refer to the inference process as distillation, as we distill the distribution over the material parameters from the distribution over the stress-deformation functions encoded by the GP posterior. The distilled distribution is easier to interpret, but preserves uncertainties. The concept of distilling knowledge from data has also been coined in the context of model discovery of physical laws in [46]. Furthermore, we note that our proposed framework can be associated with generative modeling. From the generative modeling point of view, the objective of training the NF would also be to generate stress-deformation functions that follow the distribution given by the target GP posterior. However, the motivation is different. In our case, the primary motivation is again to infer the distribution of material parameters and not the generation of new stress-deformation functions.

We demonstrate the capability of our approach for the isotropic Treloar dataset [47] and an anisotropic dataset of human cardiac tissue [48]. The research code for our numerical tests is implemented in the Python programming language and published on GitHub and Zenodo [49]. Our code is mainly based on PyTorch [50]. For the implementation of the GPs, we used GPyTorch [51]. In addition, we implemented the NF and the Sobol’ sensitivity analysis using the normflows [52] and SALib [53, 54] frameworks, respectively.

2. Methodology

In this section, we present a framework for the quantification of uncertainties in the discovery of material constitutive models. The method is based on the distillation of a joint distribution over the parameters of a sparse constitutive model from GP posteriors of stress-deformation functions. First, we state the problem to be solved and present our solution approach. Second, we recapitulate the basics of hyperelastic constitutive modeling, define a general hyperelastic model library for SEFs that covers both isotropic and anisotropic materials, and introduce the notation used in this paper. Finally, we present the four-step framework for distilling a joint distribution of material parameters from the GP posteriors and further elaborate on the individual steps in more detail.

2.1. Problem statement and solution approach

For a given dataset \mathcal{D} containing stress-deformation measurements from mechanical tests, the objective is to identify an appropriate and interpretable constitutive model from a predefined constitutive model library and simultaneously infer the probability density of the material parameters. The interpretability of the discovered model is improved by reducing the initial vector of material parameters $\boldsymbol{\kappa} \in \mathbb{R}^{n_\kappa}$ of the model library to the relevant parameters $\tilde{\boldsymbol{\kappa}} \in \mathbb{R}^{\tilde{n}_\kappa}$, so that $\tilde{n}_\kappa \ll n_\kappa$.

For the sake of brevity, the following motivating discussion is kept short. Details on the derivations can be found in Appendix A. The starting point for

a Bayesian approach to model discovery is usually the joint probability density function (PDF) $p(\boldsymbol{\kappa}, \mathcal{D})$ of the material parameters $\boldsymbol{\kappa}$ and the stress-deformation data \mathcal{D} . Using Bayes' law yields the posterior density

$$p(\boldsymbol{\kappa} | \mathcal{D}) = \frac{p(\mathcal{D} | \boldsymbol{\kappa})p(\boldsymbol{\kappa})}{p(\mathcal{D})}, \quad (1)$$

where $p(\mathcal{D} | \boldsymbol{\kappa})$ denotes the likelihood function, $p(\boldsymbol{\kappa})$ the prior density, and $p(\mathcal{D})$ the evidence which can be considered constant for fixed data \mathcal{D} [31]. The sparsity of the constitutive model can generally be promoted, e.g., by using sparsifying-priors for $p(\boldsymbol{\kappa})$ as done in [32]. However, the typical use case for model discovery assumes that there is a large number of material parameters, and a priori very little is known about the relevance of the individual material parameters and also the structure of the constitutive model. Therefore, it is challenging to formulate a suitable prior $p(\boldsymbol{\kappa})$, even if the prior is mainly used for sparsification. When using non-informative, i.e., very vague or diffuse priors, the posterior density $p(\boldsymbol{\kappa} | \mathcal{D})$ in (1) is almost entirely determined by the likelihood function $p(\mathcal{D} | \boldsymbol{\kappa})$. Consequently, the benefits of Bayesian regularization are lost, and the posterior reduces to frequentist estimates [55].

Instead of targeting the posterior (1) directly, we introduce an intermediate GP with stress values \mathbf{f} . This latent GP is conditioned on \mathcal{D} and subsequently serves as a data surrogate for inferring $\boldsymbol{\kappa}$. As shown in Appendix A, this two-step approach can be expressed as

$$p(\boldsymbol{\kappa} | \mathcal{D}) = \int p(\boldsymbol{\kappa}, \mathbf{f} | \mathcal{D}) d\mathbf{f} = \int p(\boldsymbol{\kappa} | \mathbf{f}) p(\mathbf{f} | \mathcal{D}) d\mathbf{f}. \quad (2)$$

Since the integral in (2) is cumbersome to compute, we instead solve a variational problem to approximate $p(\boldsymbol{\kappa} | \mathcal{D})$ as follows

$$p_{\kappa}^*(\boldsymbol{\kappa}) = \arg \min_{p_{\kappa}(\boldsymbol{\kappa})} D(\mathbf{T}_{M\#} p_{\kappa}(\mathbf{f}), p(\mathbf{f} | \mathcal{D})). \quad (3)$$

Here, $\mathbf{T}_M : \boldsymbol{\kappa} \mapsto \mathbf{g}$ represents the model library, taking parameter values $\boldsymbol{\kappa}$ to the discrete GP space and $\mathbf{T}_{M\#} p_{\kappa}(\mathbf{f})$ is the PDF of the push-forward measure of $p_{\kappa}(\boldsymbol{\kappa})$ implied by the deterministic model library. Furthermore, D denotes a distance between PDFs. In Appendix A, we show that for a perfect model library, covering the entire set of GP paths, \mathbf{T}_M being bijective, a suitable choice of D and a sufficiently rich variational set for PDF $p_{\kappa}(\boldsymbol{\kappa})$, $p_{\kappa}^*(\boldsymbol{\kappa}) = p(\boldsymbol{\kappa} | \mathcal{D})$. Hence, the variational approach targets the posterior (2). However, we will apply (3) in much more general and realistic settings as a variational substitute for the full Bayesian approach, effectively removing the need to formulate a prior for the material parameters. Note that for an imperfect model library or a lack of expressiveness of $p_{\kappa}(\boldsymbol{\kappa})$, the distance in (3) does not fully vanish, and there is a mismatch between the densities $p_{\kappa}^*(\boldsymbol{\kappa})$ and $p(\boldsymbol{\kappa} | \mathcal{D})$. In the variational approach, the sparsity of $p_{\bar{\kappa}}(\bar{\boldsymbol{\kappa}})$ can then be achieved, e.g., in a downstream step in which a sensitivity analysis is performed and non-sensitive parameters are removed. In Section 2.4, we propose a framework for solving the variational

problem (3) and reducing the inferred density $p_\kappa(\boldsymbol{\kappa})$ to the relevant material parameters.

2.2. Hyperelastic constitutive modeling

In the framework of continuum solid mechanics, the first Piola-Kirchhoff stress tensor \mathbf{P} is derived from a scalar-valued SEF W as follows

$$\mathbf{P} = \frac{\partial W(\mathbf{F}; \boldsymbol{\kappa})}{\partial \mathbf{F}} \quad (\text{compressible case}). \quad (4)$$

Here, $\mathbf{F} = \text{Grad } \mathbf{x}$ denotes the deformation gradient and $\mathbf{x} \in \mathbb{R}^3$ corresponds to the position of a material point in the current configuration. Furthermore, $\boldsymbol{\kappa} \in \mathbb{R}^{n_\kappa}$ is a vector of material parameters with n_κ components. In the special case of incompressibility, the constraint $\det \mathbf{F} = 1$ is enforced via a Lagrange multiplier which can be identified as the hydrostatic pressure p . Accordingly, (4) modifies to

$$\mathbf{P} = \frac{\partial \bar{W}(\mathbf{F}; \boldsymbol{\kappa})}{\partial \mathbf{F}} - p \mathbf{F}^{-\top} \quad (\text{incompressible case}). \quad (5)$$

Note that in this special case, \bar{W} denotes only the isochoric part of the SEF. The hydrostatic pressure p in (5) is usually determined from global equilibrium in combination with loading and boundary conditions. The identification of a suitable SEF $\bar{W}(\mathbf{F}; \boldsymbol{\kappa})$ in (5) from stress-deformation data constitutes a supervised regression problem that requires the formulation of a suitable ansatz for \bar{W} . In the context of continuum mechanics, it is of utmost importance that such an ansatz is compatible with fundamental constraints, such as thermodynamic consistency, objectivity, material and Cauchy stress symmetry, non-negativity and polyconvexity. For more details, the reader is referred to standard textbooks, e.g., [2].

In the present work, we consider isochoric hyperelastic SEFs \bar{W} that fulfill the aforementioned constraints by construction and can be written as a linear combination of the model terms $\{\phi^{(j)}\}_{j=1}^{n_\phi}$ as follows

$$\bar{W}(\mathbf{F}, \{\mathbf{M}^{(i)}\}_{i=1}^{n_M}; \boldsymbol{\kappa}) = \sum_{j=1}^{n_\phi} c^{(j)} \phi^{(j)}(\mathbf{F}, \{\mathbf{M}^{(i)}\}_{i=1}^{n_M}; \mathbf{w}^{(j)}). \quad (6)$$

Here, $c^{(j)}$ and $\mathbf{w}^{(j)}$ denote the outer-linear and inner-non-linear material parameters, respectively, composed as $\boldsymbol{\kappa} = [c^{(1)}, \dots, c^{(n_\phi)}, \mathbf{w}^{(1)\top}, \dots, \mathbf{w}^{(n_\phi)\top}]^\top$. In addition, $\{\mathbf{M}^{(i)}\}_{i=1}^{n_M}$ denotes a set of structural tensors that describe the class of material symmetry. A reduced representation of the input arguments \mathbf{F} and $\{\mathbf{M}^{(i)}\}_{i=1}^{n_M}$ in (6) is obtained with their invariants I_i . The explicit formulations of the constitutive models used will be presented together with the numerical test cases in Section 3.

The general form of the model library (6) expresses the isochoric hyperelastic SEF as a sum over possibly non-linear model terms and includes many classical and modern approaches. For example, in the context of EUCLID [7], constitutive models of type (6) were considered, but with linear coefficients only. Even CANNs, originally introduced in [22], can be formulated in the general form given in (6), resulting in model libraries with non-linear parameters, see [56].

2.3. Dataset and notation

We consider a dataset $\mathcal{D} = \{ \{ \mathbf{F}^{(t,d)}, \{ P^{(t,q,d)} \}_{q=1}^{n_q^{(t)}} \}_{d=1}^{n_d^{(t)}} \}_{t=1}^{n_t}$ composed of pairwise stress-deformation measurements from n_t mechanical tests. In the test t , $n_d^{(t)}$ deformation gradients and stress tensors are measured. Typically, in each mechanical test t , only a subset of $n_q^{(t)} \leq 9$ components of the stress tensor \mathbf{P} are observed. Throughout this paper, deformation related quantities are mainly indexed by a double-index, such as the deformation gradients $\mathbf{F}^{(t,d)}$ in \mathcal{D} . Similarly, the stress components are indexed by a triple-index of the form $P^{(t,q,d)}$. Here, t, q, d are the indices for the mechanical test, the observed stress component, and the measurement, respectively. For simplicity, the integer value of the index t is sometimes replaced by its respective abbreviation, such as UT for a uniaxial tension test. Moreover, if there is no dependence on the measurement point, the respective index d will be omitted.

We introduce the observation map $\mathbf{O}^{(t,q)} : \mathbb{R}^{3 \times 3} \rightarrow \mathbb{R}$ that filters out the stress component $q \in \{1, \dots, n_q^{(t)}\}$ observed in the respective mechanical test t . For the uniaxial tension (UT) test in the Treloar dataset [47], e.g., the observation map is defined as $\mathbf{O}^{(\text{UT},1)}(\mathbf{P}) = P_{11}$. The specific definitions of the observation maps for all the numerical test cases we consider in this paper are provided in Appendix B.1.

Furthermore, $\mathcal{P}^{(t)}$ is the set of all observed stress components for the mechanical test t with the cardinality of the set $|\mathcal{P}^{(t)}| = n_q^{(t)}$. The set of observed stress components is indexed by the observed stress index q . For example, for the UT test in the Treloar dataset, $\mathcal{P}^{(\text{UT})} = \{P_{11}\}$ and $\mathcal{P}_{q=1}^{(\text{UT})} = P_{11}$. The set of all observed stress components for the dataset \mathcal{D} is the union of all $\mathcal{P}^{(t)}$ for all tests t , which is $\mathcal{P} = \mathcal{P}^{(1)} \cup \dots \cup \mathcal{P}^{(t)}$ with $|\mathcal{P}| = n_q \leq 9$. Please note that throughout this paper, we index the sets $\mathcal{P}^{(t)}$ to refer to specific observed components of the stress tensor.

Finally, similar to the observation map, we use deformation filters $\mathbf{F}_{\mathcal{P}_q^{(t)}}$ that filter out the reduced deformation vectors $\mathbf{\Lambda}^{(t,q)} = \mathbf{F}_{\mathcal{P}_q^{(t)}}(\mathbf{F}) \in \mathbb{R}^{n_{\Lambda}^{(t,q)}}$ from the deformation gradient. The reduced deformation vector $\mathbf{\Lambda}^{(t,q)}$ only contains the deformation components that are relevant to predict the stress component $\mathcal{P}_q^{(t)}$. In the Treloar dataset, e.g., the stress component P_{11} depends only on the deformation components F_{11} and F_{22} , such that $\mathbf{\Lambda}^{(\text{UT},1)} = \mathbf{F}_{P_{11}}(\mathbf{F}) = [F_{11}, F_{22}]^{\top}$. The remaining components of \mathbf{F} are irrelevant with regard to P_{11} , taking into account all mechanical tests carried out to collect the dataset. For the specific definitions of the deformation filters $\mathbf{F}_{\mathcal{P}_q^{(t)}}$, we refer to Appendix B.2.

A central idea of our framework is that we do not consider individual stress-deformation tensor pairs in isolation, but rather consider stress-deformation functions as entities. However, the various steps in our framework require the functions to be discretized. The vector $\mathbf{f}^{(t,q)} \in \mathbb{R}^{n_s^{(t)}}$ represents the discretized scalar-valued stress-deformation function for the t -th mechanical test, which contains the q -th stress component at a total of $n_s^{(t)}$ points. The corresponding functions for all tests can then be stacked in one vector as follows

$$\mathbf{f} = \begin{bmatrix} \mathbf{f}^{(t=1,q=1)} \\ \vdots \\ \mathbf{f}^{(t=1,q=n_q^{(1)})} \\ \vdots \\ \mathbf{f}^{(t=n_t,q=1)} \\ \vdots \\ \mathbf{f}^{(t=n_t,q=n_q^{(n_t)})} \end{bmatrix} \in \mathbb{R}^{n_s} \quad \text{with} \quad n_s = \sum_{t=1}^{n_t} n_q^{(t)} n_s^{(t)}, \quad \mathbf{f}^{(t,q)} \in \mathbb{R}^{n_s^{(t)}}, \quad (7)$$

where n_s is the total number of discretization points. Furthermore, the stresses in $\mathbf{f}^{(t,q)}$ are associated with the deformation gradients in $\mathbf{F}_f^{(t)} = [\mathbf{F}^{(t,s=1)^T}, \dots, \mathbf{F}^{(t,s=n_q^{(t)})^T}]^T \in \mathbb{R}^{3n_q^{(t)} \times 3}$. If the dataset comprises several mechanical tests, the total number of discretized functions is $n_f = \sum_{t=1}^{n_t} n_q^{(t)}$.

The number of discretization points per test $n_s^{(t)}$ is a hyperparameter which determines the resolution of the discretized stress-deformation functions $\mathbf{f}^{(t,q)}$ and is generally not the same as $n_d^{(t)}$. Accordingly, the deformation gradients used to discretize the stress-deformation functions are not identical to the deformation gradients in \mathcal{D} . Instead, we intentionally introduce a discretization of the stress-deformation functions that is totally independent of the measurements and provides us with the following advantages: First, we can choose the resolution of the function discretization independently of the measurement data, e.g., based on their expected smoothness. Second, we can also add discretization points between measurement points that may be sparse to augment the data and in consequence the resolution of the stress-deformation functions. Throughout this contribution, deformations are evenly distributed between the minimum and maximum deformation values for the respective mechanical test t taken from the dataset. Finally, the index-notation introduced in this section is summarized in Table 1.

2.4. Distilling statistical constitutive models from GP posteriors

We propose a framework for UQ in model discovery that solves the variational problem in (3) and further reduces the inferred PDF $p_{\kappa}(\boldsymbol{\kappa})$ to the most relevant material parameters in four subsequent steps:

- (i) For each observed stress component in \mathcal{P} , we train a GP on a subset of the dataset \mathcal{D} . In the following, we refer to the set of GPs for the different observed stress components as an independent multi-output GP.

Table 1: Summary of the notation.

t	index for mechanical test
q	index for observed stress component
d	index for measurement
n_t	number of mechanical tests
$n_q^{(t)}$	number of observed stress components in test t ($n_q^{(t)} \leq 9$)
n_q	total number of observed stress components ($n_q \leq 9$)
$n_d^{(t)}$	number of measurements in test t
$\mathbf{F}^{(t,d)}$	deformation gradient for measurement d in test t
$P^{(t,q,d)}$	observed stress component q for measurement d in test t
$O^{(t,q)}$	observation map for observed stress component q in test t
$\mathcal{P}^{(t)}$	set of observed stress components in test t ($ \mathcal{P}^{(t)} = n_q^{(t)}$)
\mathcal{P}	union of all sets of observed stress components $\mathcal{P}^{(t)}$ ($ \mathcal{P} = n_q$)
$\mathcal{P}_q^{(t)}$	observed stress component q from set $\mathcal{P}^{(t)}$
$F_{\mathcal{P}_q^{(t)}}^{(t)}$	deformation filter for observed stress component q in set $\mathcal{P}^{(t)}$
$\mathbf{\Lambda}^{(t,q)}$	reduced deformation vector for stress component q in test t
$\mathbf{f}^{(t,q)}$	discretized stress-deformation function for observed stress component q in test t
n_f	number of discretized stress-deformation functions
\mathbf{f}	discretized stress-deformation function for all tests and observed stress components
s	index for discretization point
$n_s^{(t)}$	number of discretization points in test t
n_s	total number of discretization points
$\mathbf{F}^{(t,s)}$	deformation gradient for discretization point s in test t

The inferred GP posterior $p_{\text{GP}}(\mathbf{f})$ models the probability distribution over stress-deformation functions conditioned on the data \mathcal{D} , i.e., $p_{\text{GP}}(\mathbf{f}) \approx p(\mathbf{f} \mid \mathcal{D})$, which is required for the variational problem formulation in (3). In subsequent steps, we use the GP posterior for data augmentation, drawing on the idea of generative modeling. Note that the GP posterior may not be physically consistent. Thus, stress-deformation functions \mathbf{f}_{GP} sampled from the GP, i.e., $\mathbf{f}_{\text{GP}} \sim p_{\text{GP}}(\mathbf{f})$, may violate the aforementioned physical constraints, such as thermodynamic consistency.

- (ii) We distill a physically consistent and interpretable statistical constitutive model from the GP posterior. For this purpose, we match the distribution $p_{\text{GP}}(\mathbf{f})$ on the one hand and the distribution defined by the statistical constitutive model $p_{\text{M}}(\mathbf{f})$ on the other by solving the variational problem (3). Note that the distribution $p_{\text{M}}(\mathbf{f})$ over stress-deformation functions corresponds to the PDF of the push-forward measure $\mathbf{T}_{\text{M}\#} p_{\kappa}(\mathbf{f})$ in (3) and is induced by the distribution of the material parameters $p_{\kappa}(\boldsymbol{\kappa})$. Throughout this paper, $p_{\text{M}}(\mathbf{f})$ is determined by $p_{\text{M}}(\mathbf{f}) = \int \delta(\mathbf{f} - \mathbf{T}_{\text{M}}(\boldsymbol{\kappa})) p_{\kappa}(\boldsymbol{\kappa}) d\boldsymbol{\kappa}$, where δ is the Dirac delta function. The deterministic map $\mathbf{T}_{\text{M}} : \boldsymbol{\kappa} \mapsto \mathbf{g} \in \mathbb{R}^{n_{\text{s}}}$ is implicitly defined by (5) and the generalized model library for the SEF in (6). In this contribution, we approximate the distribution of the material parameters by a NF $p_{\kappa}(\boldsymbol{\kappa}; \boldsymbol{\Phi})$ parameterized in $\boldsymbol{\Phi}$, i.e., $p_{\kappa}(\boldsymbol{\kappa}) \approx p_{\kappa}(\boldsymbol{\kappa}; \boldsymbol{\Phi})$. In comparison to standard distributions, such as multivariate Gaussian distributions, using NFs also enables us to approximate more complex, high-dimensional joint distributions. The distribution of material parameters, in turn, induces a parameterized distribution over stress-deformation functions as follows

$$p_{\text{M}}(\mathbf{f}; \boldsymbol{\Phi}) = \int \delta(\mathbf{f} - \mathbf{T}_{\text{M}}(\boldsymbol{\kappa})) p_{\kappa}(\boldsymbol{\kappa}; \boldsymbol{\Phi}) d\boldsymbol{\kappa}. \quad (8)$$

In order to match the distributions, we minimize the Wasserstein-1 distance $\mathcal{W}_1(p_{\text{GP}}(\mathbf{f}), p_{\text{M}}(\mathbf{f}; \boldsymbol{\Phi}))$ between them with respect to the distributional parameters $\boldsymbol{\Phi}$ according to the variational problem formulation (3). An advantageous property of the Wasserstein-1 distance is that this metric can be estimated solely from samples of both distributions, which in our case can be easily generated. Moreover, in view of (8) and for n_{κ} smaller than n_{s} , the density $p_{\text{M}}(\mathbf{f}; \boldsymbol{\Phi})$ will be a low-dimensional sub-manifold of n_{s} . Hence, the measures associated to $p_{\text{M}}(\mathbf{f}; \boldsymbol{\Phi})$ and $p_{\text{GP}}(\mathbf{f})$ will be mutually singular. The Wasserstein-1 distance is still applicable in this setting, whereas the Kullback-Leibler divergence and other distances are not. Since the deterministic map \mathbf{T}_{M} satisfies all aforementioned constraints by construction, all functions $\mathbf{f}_{\text{M}} \sim p_{\text{M}}(\mathbf{f}; \boldsymbol{\Phi})$ are physically consistent. However, after this step, the model does not necessarily have to be sparse and $p_{\kappa}(\boldsymbol{\kappa}; \boldsymbol{\Phi})$ is defined as a joint distribution of all parameters that were originally included in the model library. The sparsity of $p_{\kappa}(\boldsymbol{\kappa}; \boldsymbol{\Phi})$ is induced in the next step.

- (iii) We reduce the joint distribution $p_{\kappa}(\boldsymbol{\kappa}; \boldsymbol{\Phi})$ to the most relevant material

parameters to promote interpretability and generalization. Therefore, we perform a sensitivity analysis with respect to the material parameters $\boldsymbol{\kappa} \sim p_{\kappa}(\boldsymbol{\kappa}; \boldsymbol{\Phi})$ and remove all non-relevant parameters from the joint distribution $p_{\kappa}(\boldsymbol{\kappa}; \boldsymbol{\Phi})$. As a measure of sensitivity, we consider the total-order Sobol’ indices of the material parameters. We then remove all material parameters whose total sensitivity indices fall below a predefined threshold.

- (iv) We perform a recalibration of the constitutive model discovered in steps (i)-(iii) by repeating step (ii) but now using only the relevant model terms and corresponding material parameters. Finally, we obtain the interpretable, physically consistent and sparse statistical constitutive model

$$\overline{W}(\mathbf{F}, \{\mathbf{M}^{(i)}\}_{i=1}^{n_M}; \tilde{\boldsymbol{\kappa}}) = \sum_{j=1}^{\tilde{n}_{\phi}} c^{(j)} \phi^{(j)}(\mathbf{F}, \{\mathbf{M}^{(i)}\}_{i=1}^{n_M}; \mathbf{w}^{(j)}), \quad \tilde{\boldsymbol{\kappa}} \sim p_{\tilde{\kappa}}(\tilde{\boldsymbol{\kappa}}; \boldsymbol{\Phi}), \quad (9)$$

where $\tilde{n}_{\phi} \ll n_{\phi}$ denotes the number of relevant model terms $\phi^{(j)}$ and $\tilde{\boldsymbol{\kappa}} \in \mathbb{R}^{\tilde{n}_{\kappa}}$ the sparse vector of material parameters with $\tilde{n}_{\kappa} \ll n_{\kappa}$. Recalibration aims to refine the statistical model and eliminate possible dependencies on terms removed in step (iii). In general, it can be assumed that the accuracy of the approximation $p_{\tilde{\kappa}}(\tilde{\boldsymbol{\kappa}}; \boldsymbol{\Phi})$ increases for smaller \tilde{n}_{κ} since with the number of parameters also the complexity of the joint distribution decreases. It is generally possible that even after recalibration some material parameters render non-sensitive and can be removed. In this case, a further recalibration step may be useful.

The framework outlined above remains generic and particularly suitable for model discovery. Instead of a fully Bayesian approach, we propose a partially Bayesian two-step inference procedure that does not require prior selection for the material parameters. In the first step, a GP posterior is inferred from the available stress-deformation data. In a second step, we then distill a physically consistent and interpretable statistical constitutive model from the GP posterior. Furthermore, NFs are very flexible and enable the approximation of complex high-dimensional distributions. Therefore, we do not need to make strong assumptions about the type of distribution of the material parameters or their correlation. In addition, NFs can be directly used for both sampling and density estimation [42], whereas MCMC-based methods provide only samples of material parameters. Finally, the Sobol’ sensitivity analysis in step (iii) provides further insights into the model selection process as we show in our numerical tests. It is worth noting that, in general, our framework can also be used for model calibration. In this special case, steps (iii) and (iv) are omitted. The complete four-step approach to UQ in model discovery is visualized in Fig. 1. Steps (i)-(iii) and the corresponding methods are explained in more detail in the following subsections.

Remark: The two-step inference procedure introduces an additional approximation step, and the associated error must be carefully controlled. In a one-step approach, instead one could consider the model $p_{\text{GP}}(\mathbf{f}) = \mathcal{N}(\mathbf{T}_M(\boldsymbol{\kappa}), \mathbf{K})$ and infer $\boldsymbol{\kappa}$ as hyperparameters of the GP. Although this procedure would be more principled from a statistical point of view, assigning a prior and inferring $\boldsymbol{\kappa}$ within this framework poses a significant challenge. Using a NF to approximate the distribution over the material parameters would add another hierarchy and additional complexity. We therefore prefer to omit formulating a prior and inferring $\boldsymbol{\kappa}$ as hyperparameters.

2.4.1. Gaussian process posterior

We infer an independent multi-output GP posterior from the dataset \mathcal{D} which is used for data augmentation in the subsequent steps. In the following, we consider the components of the stress tensor to be independent of each other and model each component that is observed at least in one mechanical test separately with a single-output GP. Furthermore, we use the reduced deformation vectors $\boldsymbol{\Lambda}^{(t,q)} = \mathbb{F}_{\mathcal{P}_q^{(t)}}(\mathbf{F}) \in \mathbb{R}^{n_\Lambda^{(t,q)}}$, introduced in Section 2.3, as input to the GP for the stress component $\mathcal{P}_q^{(t)}$. This allows us to reduce the number of GP hyperparameters. For the specific definitions of the deformation filters $\mathbb{F}_{\mathcal{P}_q^{(t)}}$, we refer to Appendix B.2.

In the following, we explain the inference of the GP posterior for a single stress component. However, for the sake of clarity, we omit the explicit dependence on indices t and q in the notation such that $\boldsymbol{\Lambda} := \boldsymbol{\Lambda}^{(t,q)}$, $\mathcal{N} := \mathcal{N}_{\mathcal{P}_q^{(t)}}$, $n_d := n_d^{(t)}$, $n_\Lambda = n_\Lambda^{(t,q)}$, etc. For simplicity, we take the mean functions of the GPs to be zero, i.e., $m(\boldsymbol{\Lambda}) = 0$. The GPs are further specified by a covariance function $k(\boldsymbol{\Lambda}, \boldsymbol{\Lambda}'; \boldsymbol{\zeta})$ with hyperparameters $\boldsymbol{\zeta}$. We choose scaled squared-exponential covariance functions which are defined as follows

$$k(\boldsymbol{\Lambda}, \boldsymbol{\Lambda}'; \boldsymbol{\zeta}) = \sigma^2 \exp\left(-\frac{1}{2} \sum_{i=1}^{n_\Lambda} \left(\frac{\Lambda_i - \Lambda'_i}{l_i}\right)^2\right), \quad (10)$$

since sample paths and the mean functions of GPs with squared exponential kernel functions are smooth [57]. Here, $\mathbf{l} \in \mathbb{R}^{n_\Lambda}$ comprises the length scales for each input dimension and $\sigma \in \mathbb{R}$ is the output scale, i.e., $\boldsymbol{\zeta} = [\mathbf{l}^\top, \sigma]^\top$. Finally, the joint distribution of all stresses corresponding to the n_d deformation states that comprise the random vector $\mathbf{P} = [P^{(1)}, \dots, P^{(n_d)}]^\top$ is

$$\mathbf{P} \sim \mathcal{N}(\mathbf{0}, \mathbf{K}(\boldsymbol{\Lambda}, \boldsymbol{\Lambda}; \boldsymbol{\zeta})), \quad (11)$$

with $\mathbf{P} : \Omega_{\mathbf{P}} \rightarrow \mathbb{R}^{n_d}$, where $\Omega_{\mathbf{P}}$ is the sample space of \mathbf{P} . Furthermore, $\boldsymbol{\Lambda} = [\boldsymbol{\Lambda}^{(1)}, \dots, \boldsymbol{\Lambda}^{(n_d)}] \in \mathbb{R}^{n_\Lambda \times n_d}$ denotes the matrix of all reduced deformation inputs and \mathbf{K} is the covariance matrix with $\mathbf{K}_{i,j} = k(\boldsymbol{\Lambda}^{(i)}, \boldsymbol{\Lambda}^{(j)}; \boldsymbol{\zeta})$.

GP prior: First, we fit the hyperparameters $\{\boldsymbol{\zeta}_{\mathcal{P}_q}\}_{q=1}^{n_q}$ of the n_q GPs to the dataset \mathcal{D} . In order to fit the GPs to the training data, we select the hyperpa-

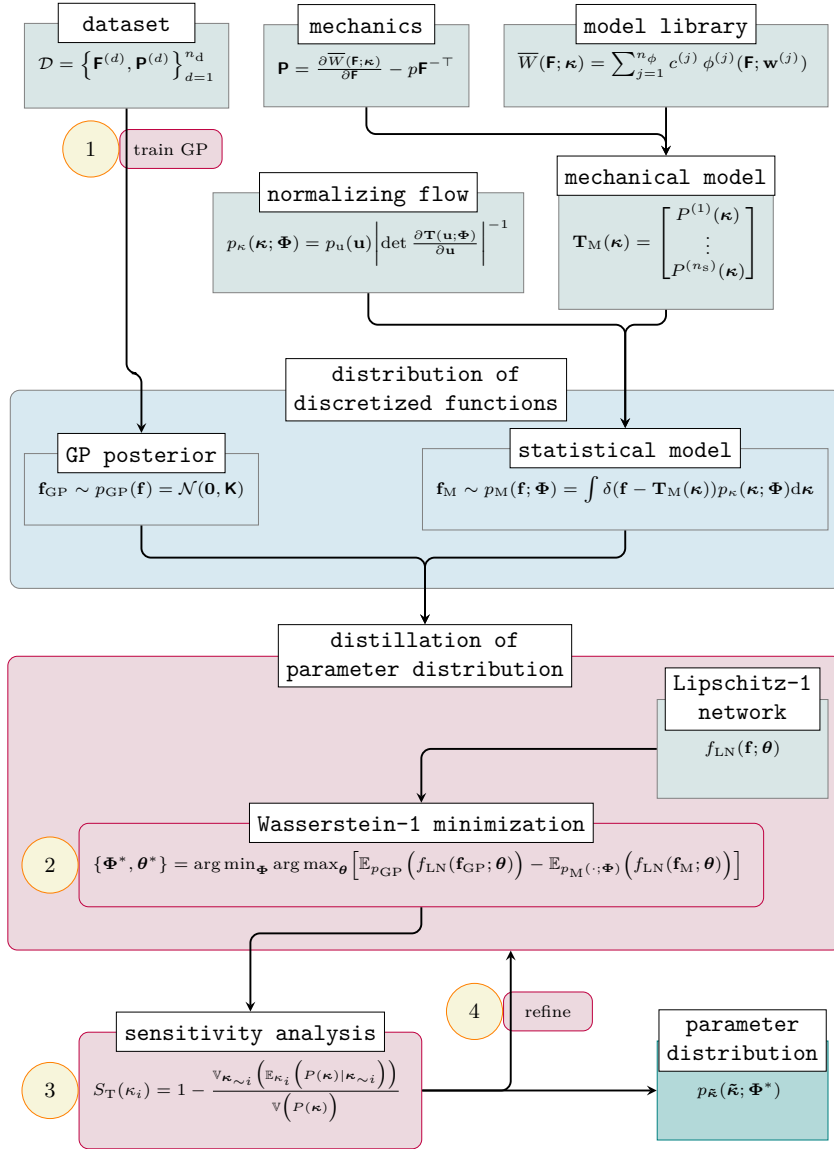


Fig. 1: Workflow for the quantification of uncertainty in model discovery by distilling interpretable material constitutive models from GP posteriors. In above workflow, the color \blacksquare encodes components, such as the data or the model library, \blacksquare the distributions over discretized stress-deformation functions, \blacksquare processes, such as the Wasserstein-1 minimization or the sensitivity analysis, and \blacksquare the resulting joint distribution over the relevant material parameters. The numbers 1 to 4 in yellow refer to the four steps of the proposed framework which are (1) GP training (Section 2.4.1), (2) model distillation (Section 2.4.2 and Section 2.4.3), (3) sensitivity analysis and model sparsification (Section 2.4.4), and (4) model recalibration.

rameters $\zeta_{\mathcal{P}_q}$ by maximizing the marginal logarithmic likelihood [57], which is also known as the empirical Bayes method.

In our statistical framework, we assume that the measured stresses \mathbf{P} are noisy observations of the true but hidden stresses \mathbf{P}^* with independent additive Gaussian noise $\boldsymbol{\varepsilon}$. Since the measured stress-deformation curves vary for different samples of the same material, the data model contains an additional term $\boldsymbol{\eta}$ that describes the variability for different samples, i.e., $\mathbf{P} = \mathbf{P}^* + \boldsymbol{\varepsilon} + \boldsymbol{\eta}$. The sample variability term is also assumed to be Gaussian distributed. Depending on the tested material and the mechanical test, the uncertainty resulting from $\boldsymbol{\eta}$ may exceed the measurement noise $\boldsymbol{\varepsilon}$. Both the measurement noise and the sample variability represent inherent randomness in mechanical testing and thus are aleatoric uncertainties. In this contribution, we assume $\boldsymbol{\eta}$ to consist of independent entries that are also independent of $\boldsymbol{\varepsilon}$ and combine both measurement noise $\boldsymbol{\varepsilon}$ and sample variability $\boldsymbol{\eta}$ into one Gaussian error term $\boldsymbol{\epsilon} = \boldsymbol{\varepsilon} + \boldsymbol{\eta}$. Furthermore, we assume that both the measurement noise and the sample variability are functions of the amount of stress. Thus, for the total error term $\boldsymbol{\epsilon}$, we use a heteroscedastic Gaussian error model

$$\boldsymbol{\epsilon} = \mathcal{N}(\mathbf{0}, \boldsymbol{\Sigma}_{\boldsymbol{\epsilon}}(\sigma_{\min}, \sigma_{\text{r}}, \mathbf{P}^*)), \quad (12)$$

with zero mean and a positive definite covariance matrix $\boldsymbol{\Sigma}_{\boldsymbol{\epsilon}}$. The covariance matrix is a function of the minimum error standard deviation σ_{\min} , the relative error standard deviation σ_{r} and the stresses. It is defined as

$$\boldsymbol{\Sigma}_{\boldsymbol{\epsilon}}(\sigma_{\min}, \sigma_{\text{r}}, \mathbf{P}^*) = \text{diag}(\max\{\sigma_{\min}^2 \mathbf{1}, \sigma_{\text{r}}^2 \mathbf{P}^{*2}\}), \quad (13)$$

where \mathbf{P}^{*2} are the element-wise squares of the true stresses, $\mathbf{1} \in \mathbb{R}^{n_{\text{d}}}$ is a vector of ones, and \max is the operator which selects the element-wise maximum of the two passed vectors. Thus, the data model simplifies to $\mathbf{P} \approx \mathbf{P}^* + \boldsymbol{\epsilon}$. We are aware that our assumptions about the error model might not fully reflect reality, since, in particular, the variability term is generally neither Gaussian nor additive. However, we expect that the datasets we use in our numerical tests contain the averaged stress measurements for several samples. Since the error contribution of each sample is lower on average, we can model the error contributions more roughly, and the effects of our simplified data model are limited. Ultimately, since the numerical tests did not reveal any problems with our assumptions, we consider these assumptions reasonable for the model discovery task presented in this work.

As the GP corresponds to a multivariate Gaussian distribution and the assumptions on the noise defined in (12) and (13) also lead to a Gaussian likelihood, there exists a closed form for the logarithmic marginal likelihood which yields

$$\log p(\mathbf{P} \mid \boldsymbol{\Lambda}; \boldsymbol{\zeta}) = -\frac{1}{2} \mathbf{P}^{\top} \tilde{\mathbf{K}}(\boldsymbol{\Lambda}, \boldsymbol{\Lambda}; \boldsymbol{\zeta})^{-1} \mathbf{P} - \frac{1}{2} \log \det \tilde{\mathbf{K}}(\boldsymbol{\Lambda}, \boldsymbol{\Lambda}; \boldsymbol{\zeta}) - \frac{n_{\text{d}}}{2} \log 2\pi, \quad (14)$$

with $\tilde{\mathbf{K}}(\boldsymbol{\Lambda}, \boldsymbol{\Lambda}; \boldsymbol{\zeta}) = \mathbf{K}(\boldsymbol{\Lambda}, \boldsymbol{\Lambda}; \boldsymbol{\zeta}) + \boldsymbol{\Sigma}_{\boldsymbol{\epsilon}}(\sigma_{\min}, \sigma_{\text{r}}, \mathbf{P}^*)$. In order to find an appropriate

point estimate for the hyperparameters ζ , for each GP, we define the optimization problem

$$\zeta^* = \arg \max_{\zeta} \log p(\mathbf{P} \mid \mathbf{A}; \zeta), \quad (15)$$

and optimize their hyperparameters using the AdamW gradient-based optimization algorithm [58]. However, we observed that the length scales obtained by solving the optimization problem in (15) tend to be too large. Excessively large length scales eventually induce a class of stress-deformation functions that vary only slowly with their input and, in fact, may cause an underestimation of the uncertainty. In general, the uncertainty intervals become narrower as the length scales increase, see [57]. Therefore, we reduce the optimized length scales by a factor of 0.6. This factor is determined manually, striking a balance between physical consistency and the coverage of the GP posterior as a measure of how well it quantifies the uncertainty in the data. For a definition of the coverage, see Appendix C. For completeness, we would like to point out that in our implementation we normalize the reduced deformation inputs to the range $[0, 1]$. Finally, the GPs with the selected hyperparameters then represent our prior belief about the stochastic processes behind the observed stress-deformation functions.

GP posterior: Second, we condition the GP prior on the corresponding subset of the observed data points in \mathcal{D} and thus infer the GP posterior. Through conditioning, the mean and covariance functions change as follows

$$\begin{aligned} \bar{\mathbf{m}}(\bar{\mathbf{A}}; \zeta^*) &= \mathbf{K}(\bar{\mathbf{A}}, \mathbf{A}; \zeta^*) \tilde{\mathbf{K}}(\mathbf{A}, \mathbf{A}; \zeta^*)^{-1} \mathbf{P}, \\ \bar{\mathbf{K}}(\bar{\mathbf{A}}, \bar{\mathbf{A}}; \zeta^*) &= \mathbf{K}(\bar{\mathbf{A}}, \bar{\mathbf{A}}; \zeta^*) - \mathbf{K}(\bar{\mathbf{A}}, \mathbf{A}; \zeta^*) \tilde{\mathbf{K}}(\mathbf{A}, \mathbf{A}; \zeta^*)^{-1} \mathbf{K}(\mathbf{A}, \bar{\mathbf{A}}; \zeta^*), \end{aligned} \quad (16)$$

where \mathbf{A}, \mathbf{P} denote the training data and $\bar{\mathbf{A}}, \bar{\mathbf{P}}$ the unseen data. From the function space view, the GP posterior describes a distribution over functions conditioned on the measured data [57]. Since we are interested in the posterior over the stress-deformation functions and not in noisy predictions, we consider the GP posterior instead of the predictive GP posterior; please refer to [57] for more details. The covariance of the GP posterior in (16) decreases when more training data is used. From this, we can conclude that the uncertainty of the GP posterior is epistemic.

Finally, from the GP posteriors, we can sample discretized stress-deformation

functions stacked in one random vector according to (7) as follows

$$\mathbf{f}_{\text{GP}} \sim \begin{bmatrix} \mathcal{N}_{\mathcal{P}_1^{(t=1)}} \left(\bar{\mathbf{m}}(\boldsymbol{\Lambda}^{(1,1)}), \bar{\mathbf{K}}(\boldsymbol{\Lambda}^{(1,1)}, \boldsymbol{\Lambda}^{(1,1)}); \boldsymbol{\zeta}_{\mathcal{P}_1^{(1)}}^* \right) \\ \vdots \\ \mathcal{N}_{\mathcal{P}_{n_q^{(1)}}^{(t=1)}} \left(\bar{\mathbf{m}}(\boldsymbol{\Lambda}^{(1,n_q^{(1)})}), \bar{\mathbf{K}}(\boldsymbol{\Lambda}^{(1,n_q^{(1)})}, \boldsymbol{\Lambda}^{(1,n_q^{(1)})}); \boldsymbol{\zeta}_{\mathcal{P}_{n_q^{(1)}}^{(1)}}^* \right) \\ \vdots \\ \mathcal{N}_{\mathcal{P}_1^{(t=n_t)}} \left(\bar{\mathbf{m}}(\boldsymbol{\Lambda}^{(n_t,1)}), \bar{\mathbf{K}}(\boldsymbol{\Lambda}^{(n_t,1)}, \boldsymbol{\Lambda}^{(n_t,1)}); \boldsymbol{\zeta}_{\mathcal{P}_1^{(n_t)}}^* \right) \\ \vdots \\ \mathcal{N}_{\mathcal{P}_{n_q^{(n_t)}}^{(t=n_t)}} \left(\bar{\mathbf{m}}(\boldsymbol{\Lambda}^{(n_t,n_q^{(n_t)})}), \bar{\mathbf{K}}(\boldsymbol{\Lambda}^{(n_t,n_q^{(n_t)})}, \boldsymbol{\Lambda}^{(n_t,n_q^{(n_t)})}); \boldsymbol{\zeta}_{\mathcal{P}_{n_q^{(n_t)}}^{(n_t)}}^* \right) \end{bmatrix}, \quad (17)$$

with $\mathbf{f}_{\text{GP}} : \Omega_{\mathbf{f}_{\text{GP}}} \rightarrow \mathbb{R}^{n_s}$, where $\Omega_{\mathbf{f}_{\text{GP}}}$ is the sample space of \mathbf{f}_{GP} . Furthermore, $\boldsymbol{\Lambda}^{(t,q)} = [\mathbf{F}_{\mathcal{P}_q^{(t)}}(\mathbf{F}^{(t,1)}), \dots, \mathbf{F}_{\mathcal{P}_q^{(t)}}(\mathbf{F}^{(t,n_s^{(t)})})] \in \mathbb{R}^{n_\lambda^{(t,q)} \times n_s^{(t)}}$ is the matrix comprising all reduced deformation inputs for the q -th observed stress component in the t -th mechanical test. Again, $n_s^{(t)}$ indicates the number of points at which the stress-deformation function for the test t is discretized and n_s the total number of points for all n_f functions stacked in \mathbf{f}_{GP} . For simplicity, in (17), we use $\mathcal{N}(\bar{\mathbf{m}}(\boldsymbol{\Lambda}), \bar{\mathbf{K}}(\boldsymbol{\Lambda}, \boldsymbol{\Lambda}); \boldsymbol{\zeta})$ as short form for $\mathcal{N}(\bar{\mathbf{m}}(\boldsymbol{\Lambda}; \boldsymbol{\zeta}), \bar{\mathbf{K}}(\boldsymbol{\Lambda}, \boldsymbol{\Lambda}; \boldsymbol{\zeta}))$.

Remark: It is worth noting that, for hyperelastic materials, all stress components are derived from the SEF and are coupled. However, in the present work, for a given deformation state, the data typically provide measurements only for a small subset of stress components. Therefore, the observations available to identify the correlation between the stress components are very limited. As a consequence, adopting a correlated multi-output GP would necessitate additional structural assumptions or strong priors on the correlation, which are typically also very limited in model discovery. For these reasons, we adopt independent multi-output GPs for the observed stress components as a pragmatic choice for constructing the target distribution used in the distillation step. Importantly, physical coupling is reintroduced at the distillation stage. Developing a surrogate model that incorporates physically informed cross-component correlations remains an important direction for future work.

2.4.2. Normalizing flows

We approximate the joint distribution $p_{\boldsymbol{\kappa}}(\boldsymbol{\kappa})$ using a NF which enables modeling of complex, high-dimensional and multi-modal distributions and potential dependencies between the material parameters [42].

The idea of NFs is to express the random vector $\boldsymbol{\kappa}$ with values in \mathbb{R}^{n_κ} via a bijective transport map based on another n_κ -dimensional random vector \mathbf{u} . However, the vector \mathbf{u} can be sampled from the base distribution which is generally simpler than the one expected for $\boldsymbol{\kappa}$. A common choice for the base distribution is a standard multivariate normal distribution [42], which we

also choose in our numerical tests. The transformation \mathbf{T} with distributional parameters Φ then induces a distribution over the random vector κ as follows

$$\kappa = \mathbf{T}(\mathbf{u}; \Phi) \quad \text{with} \quad \mathbf{u} \sim \mathcal{N}(\mathbf{0}, \mathbf{I}), \quad (18)$$

where $\mathbf{0} \in \mathbb{R}^{n_\kappa}$ is a vector of zeros and $\mathbf{I} \in \mathbb{R}^{n_\kappa \times n_\kappa}$ is the identity matrix, respectively [42]. Provided that the transformation \mathbf{T} is invertible and both \mathbf{T} and \mathbf{T}^{-1} are differentiable, the probability density $p_\kappa(\kappa; \Phi)$ can be obtained by a change of variables [59, 60] as follows

$$p_\kappa(\kappa; \Phi) = p_u(\mathbf{u}) \left| \det \frac{\partial \mathbf{T}(\mathbf{u}; \Phi)}{\partial \mathbf{u}} \right|^{-1} = p_u(\mathbf{T}^{-1}(\kappa; \Phi)) \left| \det \frac{\partial \mathbf{T}^{-1}(\kappa; \Phi)}{\partial \kappa} \right|, \quad (19)$$

where $\mathbf{T}^{-1}(\kappa; \Phi)$ is the inverse transformation. In general, the parameters of the base distribution, such as the standard deviation, can also be trainable. However, in theory, the parameters of the base distribution can be absorbed in the transformation and thus be considered to be fixed.

The transformation \mathbf{T} is usually a composition of a finite number of sub-transformations with the general form

$$\begin{aligned} \mathbf{T} : \mathbb{R}^{n_\kappa} &\rightarrow \mathbb{R}^{n_\kappa}, \\ \mathbf{u} &\mapsto \mathbf{T}(\mathbf{u}; \Phi) = (\mathbf{T}^{(n_T+1)}(\bullet; \Phi^{(n_T+1)}) \circ \dots \circ \mathbf{T}^{(1)}(\bullet; \Phi^{(1)}))(\mathbf{u}). \end{aligned} \quad (20)$$

Here, \bullet denotes the input of the sub-transformation which corresponds to the output of the next inner sub-transformation. Each sub-transformation in the composition (20) is defined as

$$\begin{aligned} \mathbf{T}^{(k)} : \mathbb{R}^{n_\kappa} &\rightarrow \mathbb{R}^{n_\kappa}, \\ \mathbf{z}^{(k-1)} &\mapsto \mathbf{T}^{(k)}(\mathbf{z}^{(k-1)}; \Phi^{(k)}) = \mathbf{z}^{(k)}, \quad k = 1, \dots, n_T + 1, \end{aligned} \quad (21)$$

where we assume that $\mathbf{z}^{(0)} = \mathbf{u}$ and $\mathbf{z}^{(n_T+1)} = \kappa$, respectively. Finally, the parameters of all $\mathbf{T}^{(k)}$ can be combined in $\Phi = \{\Phi^{(k)}\}_{1 \leq k \leq n_T+1}$.

In this paper, we use inverse autoregressive flows (IAFs) [61] to estimate the joint probability density $p_\kappa(\kappa)$. In IAFs, the transformations $\mathbf{T}^{(k)}$ in (21) are based on (inverse) autoregressive transformations defined as

$$\mathbf{T}^{(k)}(\mathbf{z}^{(k-1)}; \Phi^{(k)}) = \mathbf{z}^{(k)} = \mathbf{l}^{(k)}(\mathbf{z}^{(k-1)}; \Phi^{(k)}) + \mathbf{s}_c^{(k)}(\mathbf{z}^{(k-1)}; \Phi^{(k)}) \odot \mathbf{z}^{(k-1)}, \quad (22)$$

for each sub-transformation $k = 1, \dots, n_T$. Here, $\mathbf{l}^{(k)} \in \mathbb{R}^{n_\kappa}$ and $\mathbf{s}_c^{(k)} \in \mathbb{R}^{n_\kappa}$, short for $\mathbf{l}^{(k)}(\mathbf{z}^{(k-1)}; \Phi^{(k)})$, $\mathbf{s}_c^{(k)}(\mathbf{z}^{(k-1)}; \Phi^{(k)})$, are the location and constrained scale vectors of the affine transformation where the latter is obtained from the unconstrained scale vector \mathbf{s} as $\mathbf{s}_c = \text{sigmoid}(\mathbf{s})$. In addition, \odot denotes the elementwise Hadamard product. The k -th location and unconstrained scale vectors are functions of the output $\mathbf{z}^{(k-1)}$ of the previous sub-transformation,

parameterized in $\Phi^{(k)}$ and implemented using masked autoencoder for distribution estimation (MADE) networks [62]. MADE networks with $L - 1$ hidden layers have the general form

$$\mathbf{h}^{(l)} = \mathbf{a}(\mathbf{b}^{(l)} + (\mathbf{M}^{(l)} \odot \mathbf{W}^{(l)})\mathbf{h}^{(l-1)}), \quad l = 1, \dots, L, \quad (23)$$

where we assume that $\mathbf{h}^{(0)} = \mathbf{z}^{(k-1)}$, $\mathbf{h}^{(L)} = [\mathbf{l}^{(k)\top}, \mathbf{s}^{(k)\top}]^\top$ and $\mathbf{h}^{(l)} \in \mathbb{R}^{n_h^{(l)}}$ for $l = 1, \dots, L - 1$, respectively. Note that instead of two separate MADE networks for the location vector and the unconstrained scale vector, we only use one network with double output size. The hyperparameter $n_h^{(l)} \in \mathbb{N}$ controls the size of the l -th hidden layer. Furthermore, \mathbf{a} denotes an elementwise activation function and all weight matrices $\mathbf{W}^{(l)}$ and bias vectors $\mathbf{b}^{(l)}$ can be summarized in $\Phi^{(k)} = \{\mathbf{W}^{(l)}, \mathbf{b}^{(l)}\}_{1 \leq l \leq L}$. The binary matrices $\mathbf{M}^{(l)}$ with indices u and v are assembled as

$$M_{u,v}^{(l)} = \begin{cases} 1, & \text{if } m^{(l)}(u) \geq m^{(l-1)}(v) \\ 0, & \text{otherwise} \end{cases}, \quad (24)$$

and ensure the autoregressive property of the IAF. Here, the scalar-valued bijective functions $m^{(l)}$ are defined as $m^{(0)}(v) = v$ with $v \in \{1, \dots, n_\kappa\}$ and $m^{(L)}(u) = u - 1$ with $u \in \{1, \dots, n_\kappa\}$ or assign a pre-set or random integer from the range $[1, \dots, n_\kappa - 1]$ for all $m^{(l)}$ with $l = 1, \dots, L - 1$. Since we use one MADE network with double output size, the binary mask of the output layer is composed of two separate sub-masks, one for the location vector and one for the unconstrained scale vector.

The autoregressive property enables modeling the dependencies between the material parameters while estimating the joint density $p_\kappa(\boldsymbol{\kappa})$. Furthermore, under mild assumptions, it can be shown that autoregressive flows are universal approximators [63]. We choose IAFs in particular because they are fast to evaluate and scale well to high-dimensional distributions [61]. However, note that there are other flow-based models which include both additional autoregressive models, such as masked autoregressive flows (MAFs) [64] or real-valued non-volume preserving (real NVP) flows [65], as well as non-autoregressive models, like Residual Flows [66]. For more details on NFs, the reader is referred to [42].

In order to ensure that the SEF (9) parameterized by $\boldsymbol{\kappa} \sim p_\kappa(\boldsymbol{\kappa}; \Phi)$ remains physically admissible, we assume the parameters to be non-negative. To enforce the non-negativity constraint numerically, we use an exponential function as the last sub-transformation, which is defined as

$$\mathbf{T}^{(n_T+1)}(\mathbf{z}^{(n_T)}; \Phi^{(n_T+1)}) = \exp(\mathbf{z}^{(n_T)}) = \boldsymbol{\kappa}, \quad (25)$$

where \exp is applied element-wise. Note that the exponential function is invertible and both the exponential and its inverse function are differentiable, so that the overall transformation \mathbf{T} is still a bijective transport map.

To fit the flow-based model to the target distribution, which we refer to as distillation of the distribution over the material parameters, the NF parameters Φ must be optimized. For this purpose, a divergence or distance between the

target distribution and the distribution estimated by the NF is generally minimized. In our case, the NF parameters Φ are optimized so that they minimize the Wasserstein-1 distance between the GP posterior and the distribution of stress-deformation functions induced by $p_\kappa(\kappa; \Phi)$, as we will elaborate in the following subsection.

2.4.3. Wasserstein-1 distance minimization

We distill the parameter distribution $p_\kappa(\kappa; \Phi)$ by minimizing the Wasserstein-1 distance between the target distribution $p_{\text{GP}}(\mathbf{f})$ defined in (17) and our statistical model $p_{\text{M}}(\mathbf{f}; \Phi)$. As can be seen from (8), the distribution $p_{\text{M}}(\mathbf{f}; \Phi)$ is induced by the parameter distribution $p_\kappa(\kappa; \Phi)$. Furthermore, the mapping $\mathbf{T}_{\text{M}} : \kappa \mapsto \mathbf{g} \in \mathbb{R}^{n_s}$ in (8) is deterministically defined by the stress-deformation relation (5) and the generalized ansatz for the SEF in (6).

Given a realization of the material parameters $\hat{\kappa}$ from their distribution $p_\kappa(\kappa; \Phi)$, we can calculate the discretized stress-deformation function \mathbf{f} induced by $\hat{\kappa}$ as follows

$$\mathbf{T}_{\text{M}}(\hat{\kappa}) = \begin{bmatrix} P^{(1,1,1)}(\hat{\kappa}) \\ \vdots \\ P^{(1,n_q^{(1)},n_s^{(1)})}(\hat{\kappa}) \\ \vdots \\ P^{(n_t,1,1)}(\hat{\kappa}) \\ \vdots \\ P^{(n_t,n_q^{(n_t)},n_s^{(n_t)})}(\hat{\kappa}) \end{bmatrix} \in \mathbb{R}^{n_s}, \quad (26)$$

where $P^{(t,q,s)}(\hat{\kappa})$ is, according to (5), calculated as

$$P^{(t,q,s)}(\hat{\kappa}) = \mathbf{O}^{(t,q)} \left(\frac{\partial \bar{W}(\mathbf{F}^{(t,s)}; \hat{\kappa})}{\partial \mathbf{F}} - p\mathbf{F}^{(t,s)-\top} \right). \quad (27)$$

Here, $\mathbf{O}^{(t,q)}$ denotes the observation map as defined in Section 2.3 and $\mathbf{F}^{(t,s)}$ are the s -th deformation gradients for the t -th test which are identical to those at which \mathbf{f}_{GP} is sampled. Please note that the statistical model $p_{\text{M}}(\mathbf{f}; \Phi)$ will never generate function samples that violate physics as long as the model library (6) is compatible with the principles of continuum mechanics, see Section 2.2.

Our ultimate goal is to find the distribution over the material parameters $\kappa \sim p_\kappa(\kappa; \Phi)$ that induces a distribution of discretized functions $p_{\text{M}}(\mathbf{f}; \Phi)$ whose Wasserstein-1 distance to $p_{\text{GP}}(\mathbf{f})$ is minimal. In the following, we frame the problem of matching the two probability distributions as an optimization problem in terms of the parameters Φ .

Here, we employ the dual form of the Wasserstein-1 distance according to the Kantorovich-Rubinstein theorem, which reads

$$\mathcal{W}_1(p_{\text{GP}}, p_{\text{M}}) = \sup_{\|\phi\|_{\text{L}} \leq 1} \mathbb{E}_{p_{\text{GP}}}(\phi(\mathbf{f}_{\text{GP}})) - \mathbb{E}_{p_{\text{M}}}(\phi(\mathbf{f}_{\text{M}})), \quad (28)$$

where for a density p on \mathbb{R}^{n_s} , the expectation operator is defined as

$$\mathbb{E}_p(\phi(\mathbf{f})) = \int_{\mathbb{R}^{n_s}} \phi(\mathbf{f})p(\mathbf{f})d\mathbf{f}. \quad (29)$$

The supremum in (28) is taken over all Lipschitz-1 functions ϕ . In fact, the dual form leads to a functional maximization over ϕ on the difference of two expectations of ϕ with respect to p_{GP} and p_{M} . For a derivation of the above dual form of the Wasserstein-1 distance, the reader is referred to [67].

In order to optimize the parameters Φ , we consider the optimization problem

$$\{\Phi^*, \theta^*\} = \arg \min_{\Phi} \arg \max_{\theta} [\mathbb{E}_{p_{\text{GP}}} (f_{\text{LN}}(\mathbf{f}_{\text{GP}}; \theta)) - \mathbb{E}_{p_{\text{M}}(\cdot; \Phi)} (f_{\text{LN}}(\mathbf{f}_{\text{M}}; \theta))], \quad (30)$$

where $f_{\text{LN}}(\mathbf{f}; \theta) : \mathbb{R}^{n_s} \rightarrow \mathbb{R}$ is a Lipschitz-1 continuous function implemented as a feedforward NN that is parameterized in θ [68, 69]. The Lipschitz-1 continuity constraint is enforced by a gradient penalty as proposed by [70].

The optimization problem defined in (30) yields a minimax problem which is solved alternately for the optimal parameters Φ^* and θ^* . While one of the two parameter sets is optimized, the other set is kept constant and denoted as Φ_c and θ_c , respectively. First, we start with maximizing the loss $\mathcal{L}_L(\Phi_c, \theta)$ with respect to θ for n_{iters}^L iterations, where $\mathcal{L}_L(\Phi_c, \theta)$ is defined as

$$\mathcal{L}_L(\Phi_c, \theta) = \mathcal{L}_W(\Phi_c, \theta) + \lambda_L \mathbb{E}_{p_{\hat{\mathbf{f}}}} \left[\left(\left\| \nabla_{\hat{\mathbf{f}}} f_{\text{LN}}(\hat{\mathbf{f}}; \theta) \right\| - 1 \right)^2 \right]. \quad (31)$$

Here, $\mathcal{L}_W(\Phi_c, \theta)$ is the loss for the Wasserstein-1 distance defined below and the second part is the Lipschitz-1 gradient penalty. The hyperparameter λ_L controls the weight of the penalty term. The function $\hat{\mathbf{f}} \sim p_{\hat{\mathbf{f}}}(\hat{\mathbf{f}})$ is defined as $\hat{\mathbf{f}} = \alpha \mathbf{f}_{\text{M}} + (1 - \alpha) \mathbf{f}_{\text{GP}}$ where α is uniformly distributed in the interval $[0, 1]$. In addition, $\nabla_{\hat{\mathbf{f}}} f_{\text{LN}}(\hat{\mathbf{f}}; \theta)$ is the gradient of the NN with respect to its input $\hat{\mathbf{f}}$. Second, we minimize the loss $\mathcal{L}_W(\Phi, \theta_c)$ with respect to the parameters Φ in one iteration. The loss $\mathcal{L}_W(\Phi, \theta_c)$ is defined as follows

$$\mathcal{L}_W(\Phi, \theta_c) = \mathbb{E}_{p_{\text{GP}}} (f_{\text{LN}}(\mathbf{f}_{\text{GP}}; \theta_c)) - \mathbb{E}_{p_{\text{M}}(\cdot; \Phi)} (f_{\text{LN}}(\mathbf{f}_{\text{M}}; \theta_c)). \quad (32)$$

We repeat this optimization procedure for a total of n_{iters}^W iterations. In both (31) and (32), we follow [45] and estimate the expectation operators by Monte Carlo sampling. In order to sample from $p_{\text{M}}(\mathbf{f}; \Phi)$, we first sample a random material parameter from $p_{\kappa}(\kappa; \Phi)$ and then calculate the stress-deformation function induced by these material parameters according to (26). Furthermore, we use the spectral norm [71] for the hidden layers of the Lipschitz-1 NN, as we observed that it accelerates convergence and stabilizes the training dynamics. For more details on the Wasserstein-1 distance optimization, see [45, 70].

Remark: Finally, we would like to make three important remarks: First, since the statistical model is constrained to physically admissible functions by construction but the GP posterior is not, these two distributions cannot be matched

exactly. This means that the Wasserstein-1 distance between the two distributions generally converges toward a positive value greater than zero during the optimization process described above. However, this mismatch is intended as we aim to distill a distribution of physically admissible stress-deformation functions from a distribution over functions that may not be physically admissible. Second, we need to distinguish between the physical consistency of the distilled model and the validity of the quantified uncertainty. In principle, the discovered model is physically consistent by construction, but there is no guarantee that the quantified uncertainty is valid. Therefore, we propose to assess the validity of the quantified uncertainty based on coverage tests, as detailed in Appendix C. Third, since the GP posterior models epistemic uncertainty and represents the target distribution, the uncertainties in the material parameters are also epistemic.

2.4.4. Sobol' sensitivity analysis and model refinement

We analyze the sensitivity of the statistical model (9) with respect to the material parameters $\boldsymbol{\kappa} \sim p_{\boldsymbol{\kappa}}(\boldsymbol{\kappa}; \boldsymbol{\Phi})$ and remove all non-sensitive parameters from the joint distribution $p_{\boldsymbol{\kappa}}(\boldsymbol{\kappa}; \boldsymbol{\Phi})$. To this end, we carry out a global, variance-based sensitivity analysis and consider the total-order Sobol' index [44]. This sensitivity index measures the total effect of the parameters κ_i with $i \in [1, \dots, n_{\boldsymbol{\kappa}}]$ on the variance of the statistical model output and also takes the interactions with the other parameters into account. The total-order Sobol' index for the s -th deformation gradient and the q -th observed stress component in the t -th mechanical test with respect to κ_i is defined as

$$S_{\text{T}}^{(t,q,s)}(\kappa_i) = 1 - \frac{\mathbb{V}_{\boldsymbol{\kappa}_{\sim i}}\left(\mathbb{E}_{\kappa_i}(P^{(t,q,s)}(\boldsymbol{\kappa}) \mid \boldsymbol{\kappa}_{\sim i})\right)}{\mathbb{V}(P^{(t,q,s)}(\boldsymbol{\kappa}))}, \quad (33)$$

with the stress component $P^{(t,q,s)}(\boldsymbol{\kappa})$ calculated according to (27). In addition, \mathbb{V} is the variance operator and $\mathbb{E}_{\kappa_i}(P^{(t,q,s)}(\boldsymbol{\kappa}) \mid \boldsymbol{\kappa}_{\sim i})$ is the conditional expectation. Here, $\boldsymbol{\kappa}_{\sim i}$ includes all material parameters except κ_i . In this contribution, we calculate the total-order Sobol' indices (33) using the Saltelli sampling method [72, 73]. As sampling bounds, we use the minimum and maximum values of each parameter which we estimate from the distribution $p_{\boldsymbol{\kappa}}(\boldsymbol{\kappa}; \boldsymbol{\Phi})$.

In order to obtain a global sensitivity measure for the material parameters in all tests $t = \{1, \dots, n_t\}$, all $n_q^{(t)}$ observed stress components, and $n_s^{(t)}$ deformation gradients, we propose averaging the total-order Sobol' index as follows

$$\bar{S}_{\text{T}}(\kappa_i) = \frac{1}{n_t} \sum_{t=1}^{n_t} \frac{1}{n_q^{(t)} n_s^{(t)}} \sum_{q=1}^{n_q^{(t)}} \sum_{s=1}^{n_s^{(t)}} S_{\text{T}}^{(t,q,s)}(\kappa_i). \quad (34)$$

In this paper, we assign the same weight to each test and each stress component. In principle, it would also be possible to give certain tests a greater weight.

After the averaged total-order Sobol' sensitivities have been calculated for all material parameters $\boldsymbol{\kappa}$, we remove those parameters from the joint distribution

that fall below a specified threshold, and are therefore considered non-sensitive. Finally, we again optimize the Wasserstein-1 distance with the remaining model terms $\{\phi^{(j)}\}_{j=1}^{\tilde{n}_\phi}$ and parameters $\tilde{\boldsymbol{\kappa}} \in \mathbb{R}^{\tilde{n}_\kappa}$ to eliminate potential dependencies of the selected parameters on the removed ones. By removing the non-sensitive parameters, we induce sparsity and favor interpretability.

We admit that one weakness of Sobol’ sensitivity analysis is that it does not provide a clear distinction between relevant and non-relevant parameters. Instead, a threshold for the total-order Sobol’ index must be selected depending on the use case. Parameters whose total-order Sobol’ index falls below that threshold are considered non-relevant. However, a strong reason for the Sobol’ sensitivity analysis is that it provides further information on the model selection process as we show in our numerical tests. The threshold for the total-order Sobol’ index is set to $1 \cdot 10^{-4}$ which leads to a reasonable trade-off between the sparsity of the discovered statistical model and its ability to quantify uncertainty for all numerical tests. For more details on the threshold selection, the reader is referred to Appendix D.

3. Results

In this section, we demonstrate the proposed framework for experimental datasets with incompressible hyperelastic materials. We start with an isotropic rubber material in Section 3.1 and then consider an anisotropic human cardiac tissue in Section 3.2. In each test case, we study the sensitivity of the individual model terms. Sensitivities are used to select the relevant terms from the model library while promoting sparsity. Throughout this paper, we quantify the uncertainty in the stress-deformation functions using centered 95 %-intervals and validate the uncertainty based on the coverage of the synthetic data and the estimated coverage of the experimental data. For further details on these criteria, see Appendix C. The hyperparameters of the GP prior, NF, Wasserstein-1 minimization and the Sobol’ sensitivity analysis are specified in Appendix D for all numerical test cases. Therein, we also present the considerations on which we base the hyperparameter selection and qualitatively discuss the influence of the hyperparameters on runtime. In order to take into account the effect of the random initialization of the NNs used in the NF and as Lipschitz-1 function, we tested five random initializations for each numerical test case. The results of this sensitivity analysis are summarized in Appendix E. In the following, we present representative results for each numerical test case.

3.1. Isotropic experimental data

First, we consider the Treloar dataset [47]. This dataset comprises one UT, equibiaxial tension (EBT) and pure shear (PS) test of isotropic incompressible vulcanized rubber material with $n_d^{(\text{UT})} = 25$, $n_d^{(\text{EBT})} = 14$ and $n_d^{(\text{PS})} = 14$ data points. In all $n_t = 3$ mechanical tests, only the first principal stress component P_{11} is measured, such that the number of measured scalar-valued stress-deformation functions is $n_f = 3$. Given the controlled stretches for the specific

tests, i.e., $\lambda_1^{\text{UT}} = \lambda_1^{\text{EBT}} = \lambda_2^{\text{EBT}} = \lambda_1^{\text{PS}} = \lambda$, the remaining stretch components are obtained under consideration of the geometry, isotropy and incompressibility conditions: $\lambda_2^{\text{UT}} = \lambda_3^{\text{UT}} = 1/\sqrt{\lambda}$, $\lambda_3^{\text{EBT}} = 1/\lambda^2$, $\lambda_2^{\text{PS}} = 1$, $\lambda_3^{\text{PS}} = 1/\lambda$. In the following, our aim is to estimate a joint distribution over the material parameters that correspond to a physically admissible and interpretable statistical constitutive model.

We start with the formulation of a general model library for the isochoric SEF of isotropic hyperelastic materials. Our model library combines both generalized Mooney-Rivlin (MR) [8] and Ogden [9] features and yields

$$\bar{W}(\mathbf{F}; \boldsymbol{\kappa}) = \sum_{\substack{m,k \geq 0 \\ 1 \leq m+k \leq n_\phi^{\text{MR}}}} c^{(m,k)} \phi_{\text{MR}}^{(m,k)}(\mathbf{F}) + \sum_{l=1}^{n_\phi^{\text{O}}} c^{(l)} \phi_{\text{O}}^{(l)}(\mathbf{F}). \quad (35)$$

Here, n_ϕ^{MR} is the degree of the generalized MR model, i.e., the maximum degree of the polynomial, and n_ϕ^{O} denotes the number of Ogden terms. Note that under the assumption of isotropy, the general model library (6) is simplified since we can neglect the structural tensors $\{\mathbf{M}^{(i)}\}_{i=1}^{n_{\text{M}}}$. Furthermore, the specific library (35) does not contain any inner-non-linear parameters $\mathbf{w}^{(j)}$. The terms of the generalized MR model are defined by the first and second invariants of the right Cauchy-Green tensor $\mathbf{C} = \mathbf{F}^\top \mathbf{F}$ which are calculated as

$$\begin{aligned} I_1 &= \text{tr}(\mathbf{C}), \\ I_2 &= \frac{1}{2} \left((\text{tr}(\mathbf{C}))^2 - \text{tr}(\mathbf{C}^2) \right). \end{aligned} \quad (36)$$

The terms of the generalized Ogden model are defined through the principal stretches λ_1 , λ_2 and λ_3 . Ultimately, the explicit form of the generalized MR and Ogden terms is

$$\begin{aligned} \phi_{\text{MR}}^{(m,k)}(I_1, I_2) &= (I_1 - 3)^m (I_2 - 3)^k, \\ \phi_{\text{O}}^{(l)}(\lambda_1, \lambda_2, \lambda_3) &= \lambda_1^{\alpha^{(l)}} + \lambda_2^{\alpha^{(l)}} + \lambda_3^{\alpha^{(l)}} - 3, \end{aligned} \quad (37)$$

where $\alpha^{(l)}$ is the exponent of the Ogden term $\phi_{\text{O}}^{(l)}$.

For our numerical test, we set $n_\phi^{\text{MR}} = 3$ and $n_\phi^{\text{O}} = 8$ with fixed Ogden exponents $\alpha^{(l)} \in \{-5, -4, -3, -1, 1, 3, 4, 5\}$. We omit the Ogden terms with exponents $\alpha^{(l)} = -2$ and $\alpha^{(l)} = 2$ since they correspond to the MR terms $\phi_{\text{MR}}^{(0,1)}$ and $\phi_{\text{MR}}^{(1,0)}$, respectively [2]. The vector of material parameters is

$$\boldsymbol{\kappa} = [c^{(0,1)}, c^{(1,0)}, \dots, c^{(n_\phi^{\text{MR}}, 0)}, c^{(1)}, \dots, c^{(n_\phi^{\text{O}})}]^\top \in \mathbb{R}^{n_\kappa}, \quad (38)$$

with $n_\kappa = 17$. When optimizing the GP hyperparameters and inferring the GP posterior, we assume that the minimum and relative error standard deviation are $\sigma_{\text{min}} = 0.01$ kPa and $\sigma_r = 5\%$, respectively. Ultimately, the runtime for

distilling the distribution of material parameters on a NVIDIA graphics processing unit (GPU) A100 is approximately 3.5 hours. In the remainder of this subsection, we report and discuss the results of this numerical test.

GP posterior: The GP posterior for all mechanical tests included in the Treloar dataset is illustrated in Fig. 2. The total estimated coverage of the centered 95 %-interval of the GP posterior reported in Fig. 2 is $EC_{95\%} = 96.23\%$, which is very close to 95 %, implying that the uncertainty in the GP posterior is well estimated.

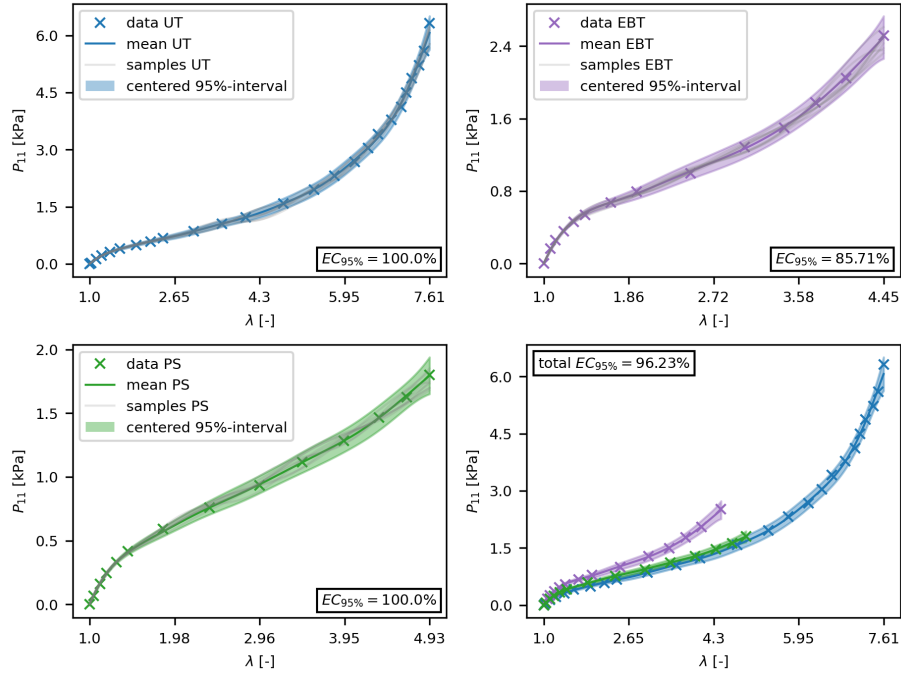


Fig. 2: Treloar test case: GP posterior. The illustrations show the GP posterior mean, the centered 95 %-intervals, some random stress-deformation function samples and the estimated coverages for the UT, EBT and PS test as well as the total estimated coverage. The GP posterior is used for data augmentation in the subsequent steps of the proposed framework.

Discovered model: As a result of our statistical model discovery framework, we ultimately obtain the distribution over the material parameters $\tilde{\boldsymbol{\kappa}}$ shown in Fig. 3. The associated, discovered SEF has the following form

$$\begin{aligned} \overline{W}(\mathbf{F}; \tilde{\boldsymbol{\kappa}}) &= c^{(0,1)}(I_2 - 3) + c^{(1,0)}(I_1 - 3) + c^{(3,0)}(I_1 - 3)^3 \\ &\quad + c^{(-1)}(\lambda_1^{-1} + \lambda_2^{-1} + \lambda_3^{-1} - 3) + c^{(1)}(\lambda_1^1 + \lambda_2^1 + \lambda_3^1 - 3), \end{aligned} \quad (39)$$

where the distribution of the reduced material parameters is approximated by the NF $p_{\tilde{\boldsymbol{\kappa}}}(\tilde{\boldsymbol{\kappa}}; \Phi^*)$, i.e., $\tilde{\boldsymbol{\kappa}} \sim p_{\tilde{\boldsymbol{\kappa}}}(\tilde{\boldsymbol{\kappa}}; \Phi^*)$. For better assignment of the parame-

ters to the terms, we do not consecutively number the Ogden parameters, but we name each parameter $c^{(l)}$ in the form $c^{(\alpha^{(l)})}$. The sensitivity analysis with respect to the initialization of the involved NNs summarized in Table E.3 underscores that the model discovery converges robustly to a very similar model structure. For three initializations, the model reported in (39) was discovered and for the other two initializations a four-term model without the term $c^{(0,1)}(I_2 - 3)$ was distilled.

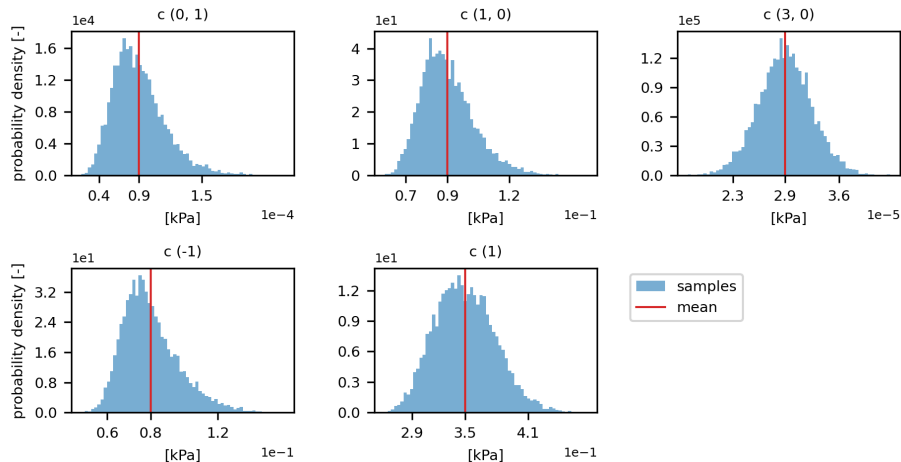


Fig. 3: Treloar test case: Distilled distribution of the material parameters after the sensitivity analysis and model refinement. The distribution over stress-deformation functions induced by this parameter distribution is shown in Fig. 4.

In the literature, the Treloar dataset is a frequently used benchmark test for incompressible hyperelastic constitutive models. Our discovered model (39) is compatible with the literature and matches the structure of well established hyperelastic models, which are primarily constructed of first invariant-based polynomials and a few Ogden terms, see, e.g., [2, 3]. Compared to most of the constitutive models available in the literature, such as the models reported in [3, 4, 22, 74], our model is less complex, remains linear in the material parameters, and is therefore easier to interpret.

The distribution of stress-deformation functions is illustrated in Fig. 4. The high coefficient of determination (R^2) of $R^2 = 0.9964$ and the low root mean squared error (RMSE) of $RMSE = 0.0942$ indicate a very good fit of the mean function. In addition, from the estimated coverage $EC_{95\%} = 92.45\%$, we can conclude that the uncertainty in the distribution of stress-deformation functions and thus the distribution of material parameters is well estimated. The estimated coverage and validation metrics R^2 and RMSE also show similarly good values for the other four initializations of the NNs that were tested. Only for one initialization, the results are slightly worse, but with $EC_{95\%} = 86.79\%$, $R^2 = 0.9964$ and $RMSE = 0.0947$ still in an acceptable range. Nevertheless,

especially the distributions for the UT and EBT tests exhibit some counterintuitive effects, see Fig. 4. In the range of medium deformation, the 95 %-intervals first become larger and then narrow again, although we assume a heteroscedastic error model. However, the described effect also occurs, e.g., in [75] for a similar setup. Since the effect does not occur exclusively in our results, we suspect that it is not an artifact of our approach, but rather that it is an attribute of the model library or the discovered model.

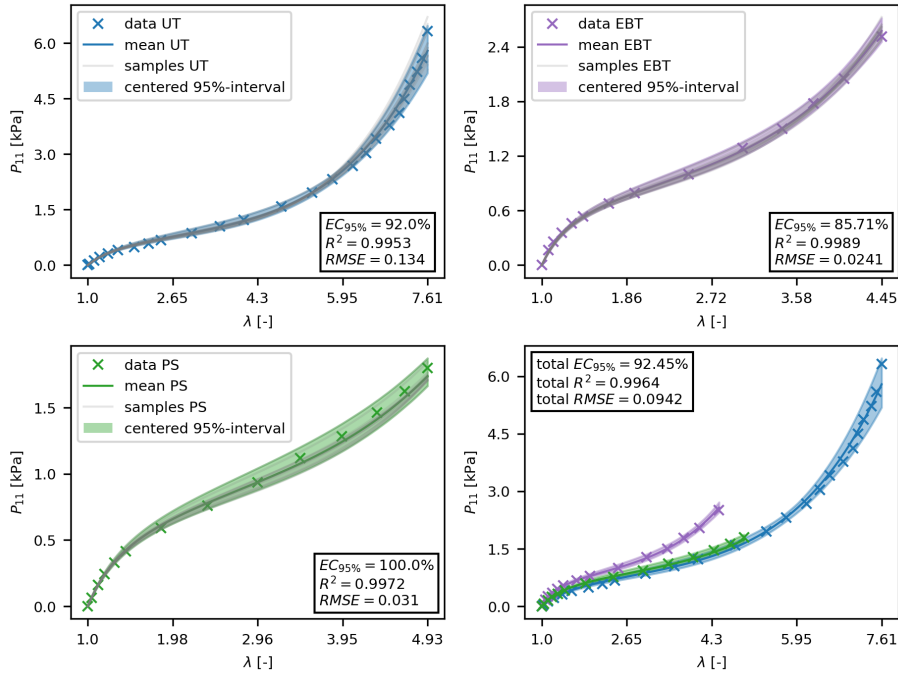


Fig. 4: Treloar test case: Distilled interpretable statistical model. The illustrations show the mean stress-deformation functions, the centered 95 %-intervals, some random stress-deformation function samples as well as the individual and total validation metrics. The RMSE and the R^2 refer to the mean stress-deformation functions, respectively, and show a good fit. Additionally, the results of the coverage estimation prove that the uncertainty is well estimated.

Sensitivity-based model selection: For more information on the model selection process, we refer the reader to Fig. 5. This figure illustrates the averaged total-order Sobol' indices of all material parameters in the model library in their descending order and visualizes how coverage develops as the model size increases.

Fig. 6 illustrates the development of the total-order Sobol' indices as a measure of the sensitivity against the principal stretches. To the best of the authors' knowledge, deformation-dependent Sobol' indices analysis has not been previ-

ously used to analyze the individual contributions of the model terms to the overall stress response. Interestingly, the results of the analysis in Fig. 6 reveal that each term of the model contributes differently depending on the type of mechanical test and the level of deformation. This could explain the diversity of the models proposed or discovered for the Treloar dataset in the past, see, e.g., [3, 4, 29, 56]. The results also give a hint of why some classical hyperelastic models fail to capture Treloar’s UT, EBT, and PS data with a single parameter set, see, e.g., [3].

The figure shows that the stress component P_{11} predicted by the discovered model is most sensitive with respect to the Neo-Hookean term $c^{(1,0)}(I_1 - 3)$. However, in the UT and EBT tests, the sensitivity of the Neo-Hookean term decreases significantly for larger deformations. This is consistent with the classical interpretation of rubber elasticity as an entropic response of Gaussian polymer chains. It explains why simple constitutive models, such as the Neo-Hookean model, are able to capture the initial slope in UT, EBT, and PS tests [76]. With increasing deformation, however, the Sobol’ indices reveal a mode-dependent activation of higher-order terms: in UT and EBT, the MR term $c^{(3,0)}(I_1 - 3)^3$ contributions become more dominant. This could reflect the transition to chain alignment and the finite extensibility effects that produce strain stiffening and curvature in the stress–deformation response [77, 78]. The deformation-dependent Sobol’ indices provide a quantitative interpretation of these observations. They clearly indicate which constitutive contributions dominate the stress response at a given deformation level and deformation mode. It becomes visually apparent why calibration over limited deformation ranges or deformation modes promotes the inclusion or exclusion of specific model terms or invariants.

3.2. Anisotropic data

In the following numerical tests, we consider data from anisotropic human cardiac tissue [48]. Compared to isotropic materials, the discovery of anisotropic constitutive models is substantially more complex because the mechanical responses of anisotropic materials are direction-dependent. For the underlying dataset, the three mutually orthogonal preferred directions are assumed to be \mathbf{f}_0 , \mathbf{s}_0 and \mathbf{n}_0 which are defined in the reference configuration according to [26] and correspond to the local fiber (f), sheet (s), and normal (n) directions, respectively. The directions are finally encoded in the structural tensors

$$\mathbf{M}_f = \mathbf{f}_0 \otimes \mathbf{f}_0, \quad \mathbf{M}_s = \mathbf{s}_0 \otimes \mathbf{s}_0, \quad \mathbf{M}_n = \mathbf{n}_0 \otimes \mathbf{n}_0, \quad (40)$$

where \otimes is the tensor product. Considering the structural tensors defined in (40) as input to the SEF, the class of material symmetry is taken into account.

The dataset comprises the measured deformation and stress data from a total of six simple shear (SS) and five biaxial tension (BT) tests. In the six SS tests, the respective shear strains increase from $\gamma_{\min} = 0.0$ to $\gamma_{\max} = 0.5$ and the principal stretches remain equal to 1.0. Depending on the direction of the shear deformation, the associated shear stress component of the Cauchy stress tensor

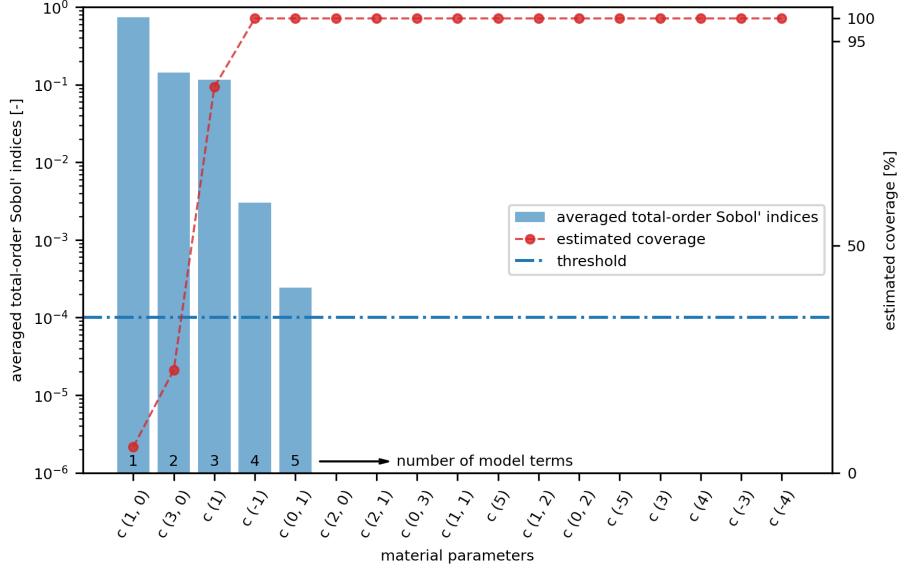


Fig. 5: Treloar test case: Illustration of the model selection process based on the sensitivity analysis. The bars show the total-order Sobol' indices for each material parameter averaged over all mechanical tests, observed stress components and discretization points in their descending order, calculated according to (34). The blue dashed-dotted line indicates the threshold of the total-order Sobol' index below which the material parameters are considered non-relevant. The numbers at the bottom of the bars indicate the total number of model terms when the model term associated with the corresponding material parameter is added to the discovered model. In addition, the red dotted line illustrates how the empirical coverage develops with increasing model size. Note that the estimated coverage may differ slightly after the refinement of the discovered model in the fourth step of the framework.

was measured. For example, in the test in which shear strain γ_{fs} is controlled, Cauchy shear stress σ_{sf} is measured. In the five BT tests, the relative stretch λ is increased from $\lambda_{\min} = 1.0$ to $\lambda_{\max} = 1.1$. The absolute stretches in the fiber and the normal direction are controlled by the ratio $\lambda_f^* : \lambda_n^*$ of the parameters λ_f^* and λ_n^* and are calculated as follows

$$\lambda_f = 1 + \lambda_f^*(\lambda - 1), \quad \lambda_n = 1 + \lambda_n^*(\lambda - 1). \quad (41)$$

For $\lambda_f^* : \lambda_n^*$, the ratios 1:1, 1:0.75, 0.75:1, 1:0.5 and 0.5:1 are considered. In each test, the principal Cauchy stresses σ_{ff} and σ_{nn} were measured. In total, the dataset thus includes $n_t = 11$ mechanical tests, but $n_f = 16$ measured scalar-valued stress-deformation functions as defined in Section 2.3. For each of these stress-deformation functions, $n_d = 11$ data points were measured.

The human cardiac tissue under consideration is assumed to be perfectly incompressible. Under this assumption, the Cauchy stress tensor is derived from the scalar-valued isochoric SEF \bar{W} as follows

$$\boldsymbol{\sigma} = J^{-1} \mathbf{P} \mathbf{F}^T = \frac{\partial \bar{W}(\mathbf{F}, \{\mathbf{M}^{(i)}\}_{i=1}^{n_M}; \boldsymbol{\kappa})}{\partial \mathbf{F}} \mathbf{F}^T - p \mathbf{I}. \quad (42)$$

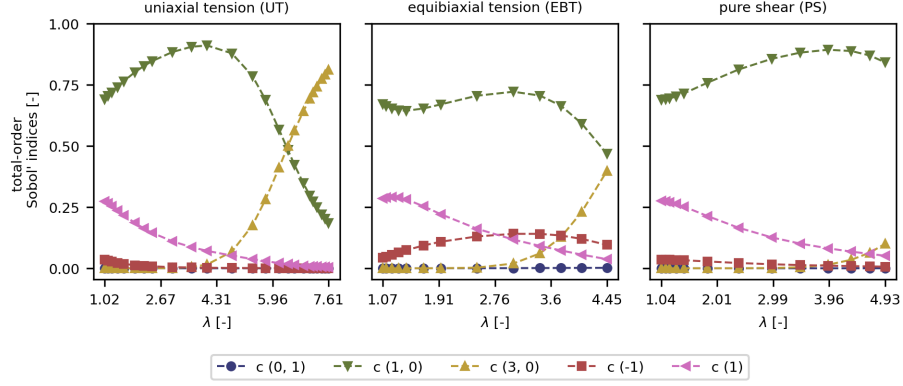


Fig. 6: Treloar test case: Development of total-order Sobol' indices over the course of the mechanical tests. The results show that the stress component P_{11} predicted by the statistical model is most sensitive to the terms linearly parameterized in $c^{(1,0)}$ (Neo-Hookean term) and $c^{(3,0)}$. However, the effect of the terms differs for the different deformation modes and usually changes with increasing deformation.

Here, \mathbf{I} denotes the identity matrix. The incompressibility constraint $J = \det \mathbf{F} = 1$ is again enforced by a Lagrange multiplier, see (5).

For our numerical tests, we adopt a modified version of the model library from [26]. In addition to the isotropic invariants defined in (36), this library also contains terms which are functions of the anisotropic fourth or eighth invariants formed by combining the Cauchy-Green tensor \mathbf{C} with the structural tensors defined in (40). The stretch-related fourth invariants are

$$\begin{aligned}
 I_{4f}(\mathbf{C}, \mathbf{M}_f) &= \mathbf{f}_0 \cdot \mathbf{C} \mathbf{f}_0, \\
 I_{4s}(\mathbf{C}, \mathbf{M}_s) &= \mathbf{s}_0 \cdot \mathbf{C} \mathbf{s}_0, \\
 I_{4n}(\mathbf{C}, \mathbf{M}_n) &= \mathbf{n}_0 \cdot \mathbf{C} \mathbf{n}_0.
 \end{aligned} \tag{43}$$

The eighth invariants considering the coupling between directions are defined as

$$\begin{aligned}
 I_{8fs}(\mathbf{C}, \mathbf{M}_f, \mathbf{M}_s) &= \mathbf{f}_0 \cdot \mathbf{C} \mathbf{s}_0, \\
 I_{8fn}(\mathbf{C}, \mathbf{M}_f, \mathbf{M}_n) &= \mathbf{f}_0 \cdot \mathbf{C} \mathbf{n}_0, \\
 I_{8sn}(\mathbf{C}, \mathbf{M}_s, \mathbf{M}_n) &= \mathbf{s}_0 \cdot \mathbf{C} \mathbf{n}_0.
 \end{aligned} \tag{44}$$

Based on the invariants in (36), (43) and (44), the model library for the isochoric

SEF yields

$$\begin{aligned}
\overline{W}(\mathbf{F}, \{\mathbf{M}^{(i)}\}_{i=1}^{n_M}; \boldsymbol{\kappa}) = & c^{(2,1)} [I_1 - 3] + c^{(2,2)} \left(\exp(w^{(1,2)} [I_1 - 3]) - 1 \right) \\
& + c^{(2,3)} [I_1 - 3]^2 + c^{(2,4)} \left(\exp(w^{(1,4)} [I_1 - 3]^2) - 1 \right) \\
& + c^{(2,5)} [I_2 - 3] + c^{(2,6)} \left(\exp(w^{(1,6)} [I_2 - 3]) - 1 \right) \\
& + c^{(2,7)} [I_2 - 3]^2 + c^{(2,8)} \left(\exp(w^{(1,8)} [I_2 - 3]^2) - 1 \right) \\
& + c^{(2,11)} [\bar{I}_{4f} - 1]^2 + c^{(2,12)} \left(\exp(w^{(1,12)} [\bar{I}_{4f} - 1]^2) - 1 \right) \\
& + c^{(2,15)} [\bar{I}_{4s} - 1]^2 + c^{(2,16)} \left(\exp(w^{(1,16)} [\bar{I}_{4s} - 1]^2) - 1 \right) \\
& + c^{(2,19)} [\bar{I}_{4n} - 1]^2 + c^{(2,20)} \left(\exp(w^{(1,20)} [\bar{I}_{4n} - 1]^2) - 1 \right) \\
& + c^{(2,23)} [I_{8fs}]^2 + c^{(2,24)} \left(\exp(w^{(1,24)} [I_{8fs}]^2) - 1 \right) \\
& + c^{(2,27)} [I_{8fn}]^2 + c^{(2,28)} \left(\exp(w^{(1,28)} [I_{8fn}]^2) - 1 \right) \\
& + c^{(2,31)} [I_{8sn}]^2 + c^{(2,32)} \left(\exp(w^{(1,32)} [I_{8sn}]^2) - 1 \right).
\end{aligned} \tag{45}$$

Here, $\bar{I}_{4f} = \max\{I_{4f}, 1\}$, $\bar{I}_{4s} = \max\{I_{4s}, 1\}$, and $\bar{I}_{4n} = \max\{I_{4n}, 1\}$ such that the terms based on the fourth invariants are activated only for tensile stretches. In the literature, the SEF in (45) is known as CANN [22]. Compared to the original SEF proposed in [26], in (45), we remove the terms based on the corrected fourth invariants $[\bar{I}_{4f} - 1]$, $[\bar{I}_{4s} - 1]$ and $[\bar{I}_{4n} - 1]$ and the terms based on the eighth invariants I_{8fs} , I_{8fn} and I_{8sn} , since these terms may induce stresses in deformation-free states. For a better comparison with the results in [26], we stick to the numbering of material parameters from [26]. However, when naming the parameters, we distinguish between linear parameters c and non-linear parameters w . Ultimately, the model library in (45) has a total of $n_\kappa = 30$ material parameters.

When optimizing the GP hyperparameters and inferring the GP posterior, we assume that the minimum and relative error standard deviation are $\sigma_{\min} = 0.01$ kPa and $\sigma_r = 5\%$, respectively. The runtime for distilling the distribution of material parameters on a NVIDIA GPU A100 is approximately 6 hours for both synthetic (Section 3.2.1) and experimental data (Section 3.2.2).

3.2.1. Synthetic data

In order to ensure controlled conditions, we start validating our framework using a synthetic dataset. The structure of the synthetic dataset is identical to the experimental one, which is defined at the beginning of this section. For data generation, we use the deterministic four-term model discovered from the

experimental dataset in [26], which is reported as

$$\begin{aligned}
\bar{W}_{4\text{-term}}(\mathbf{F}, \{\mathbf{M}^{(i)}\}_{i=1}^{n_M}; \boldsymbol{\kappa}) &= 5.162 [I_2 - 3]^2 \\
&+ 0.081 \left(\exp(21.151 [\bar{I}_{4f} - 1]^2) - 1 \right) \\
&+ 0.315 \left(\exp(4.371 [\bar{I}_{4n} - 1]^2) - 1 \right) \\
&+ 0.486 \left(\exp(0.508 [I_{8fs}]^2) - 1 \right).
\end{aligned} \tag{46}$$

After generating the data, we added heteroscedastic Gaussian noise to the data according to the data model defined in Section 2.4.1. Here, we also assume a minimum and a relative error standard deviation of $\sigma_{\min} = 0.01$ kPa and $\sigma_r = 5\%$, respectively.

Discovered model: We discover an isochoric SEF of the form

$$\begin{aligned}
\bar{W}(\mathbf{F}, \{\mathbf{M}^{(i)}\}_{i=1}^{n_M}; \tilde{\boldsymbol{\kappa}}) &= c^{(2,3)} [I_1 - 3]^2 \\
&+ c^{(2,7)} [I_2 - 3]^2 + c^{(2,8)} \left(\exp(w^{(1,8)} [I_2 - 3]^2) - 1 \right) \\
&+ c^{(2,12)} \left(\exp(w^{(1,12)} [\bar{I}_{4f} - 1]^2) - 1 \right) \\
&+ c^{(2,19)} [\bar{I}_{4n} - 1]^2 + c^{(2,20)} \left(\exp(w^{(1,20)} [\bar{I}_{4n} - 1]^2) - 1 \right) \\
&+ c^{(2,24)} \left(\exp(w^{(1,24)} [I_{8fs}]^2) - 1 \right) \\
&+ c^{(2,27)} [I_{8fn}]^2.
\end{aligned} \tag{47}$$

The distribution of the reduced material parameters $\tilde{\boldsymbol{\kappa}}$ is approximated by the NF $p_{\tilde{\boldsymbol{\kappa}}}(\tilde{\boldsymbol{\kappa}}; \boldsymbol{\Phi}^*)$ and is shown in Fig. 7. Compared to the four-term model used for data generation, the discovered model contains four additional terms, but only two of them are based on invariants which were not considered for data generation, namely the first invariant I_1 and the eighth invariant I_{8fn} . The results of the sensitivity analysis with respect to the initialization of the involved NNs are reported in Table E.4. For all five initializations, isochoric SEFs similar to (47) were discovered: the five model structures discovered have a total of between eight and ten terms, with seven terms in common. All five models contain the four terms used for data generation.

The results show that for none of the five initializations of the NNs, the constitutive model used for data generation was discovered and that all five discovered models have more than four terms. One key reason for this is that we do not aim to fit the model to the specific stress-deformation function defined in (46). Instead, we aim to match a parameterized statistical model to the distribution defined by the GP posterior. By some probability, this distribution may yield some stress-deformation functions with deviating characteristics that can only be described by slightly different constitutive models. Even in a deterministic setting, noise can make the problem ill-posed or at least complicate the identifiability, see, e.g., [11]. Therefore, we assume that additional

terms are needed to achieve the required flexibility of the statistical model. Another possible reason is the collinearity between the different terms, which may also complicate model discovery [56, 79] and cause identifiability problems [80]. Eventually, collinearity prevents the discovery of a unique model.

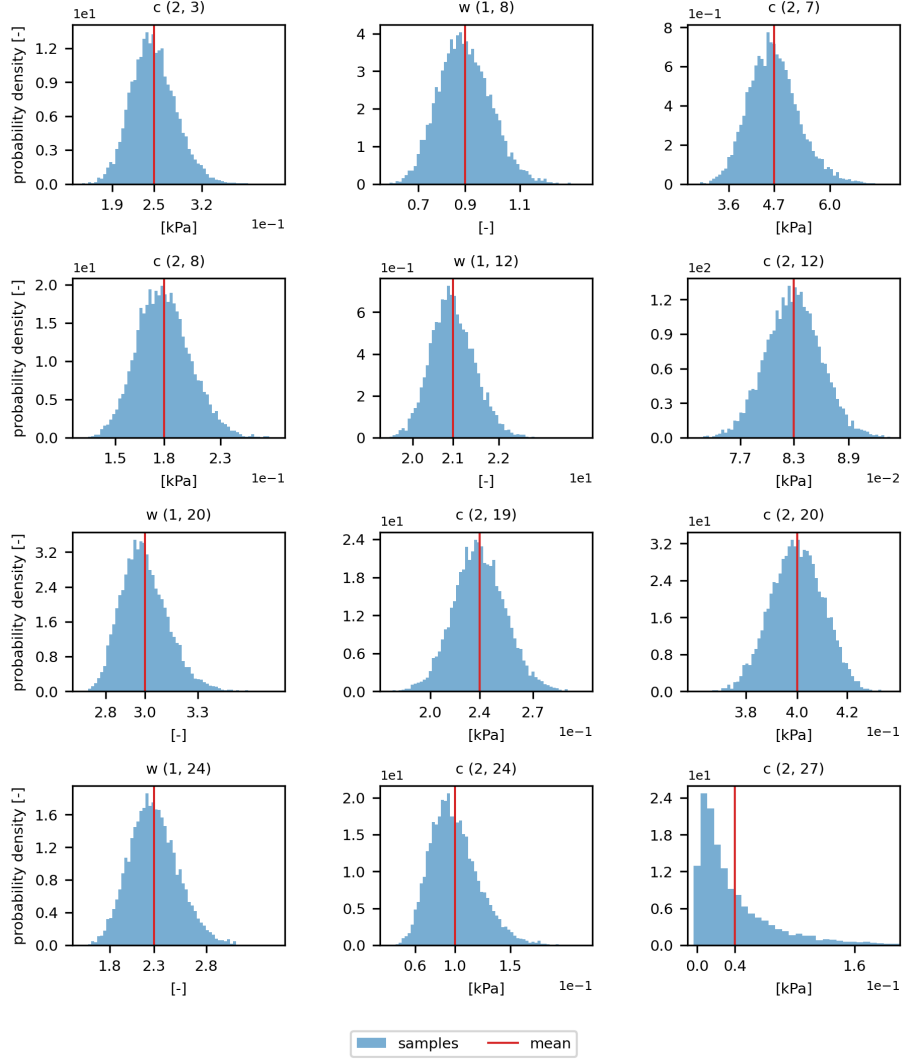


Fig. 7: Synthetic anisotropic test case: Distilled distribution of the material parameters after the sensitivity analysis and model refinement. The distribution over stress-deformation functions induced by this parameter distribution is shown in Fig. 8.

The distribution of stress-deformation functions induced by the distribution over material parameters is shown in Fig. 8. In contrast to the experimental

datasets, the true stress values are known for the synthetic test case. The validation metrics R^2 , RMSE, and the coverage are therefore calculated using the true stress values. Please note, however, that the reported coverages are still only estimates, as they are calculated based on relatively few data points, see Appendix C. Both the high $R^2 = 0.9997$ and the low $\text{RMSE} = 0.0207$ values prove a very good fit of the mean stress-deformation function to the true data. The coverage of the true data $C_{95\%} = 96.59\%$ is close to the optimal value of 95%. With the four other NN initializations, for which similar constitutive models were distilled, comparable validation metrics are achieved, see Table E.4. The **GP posterior** representing the target distribution has a coverage of $C_{95\%} = 89.77\%$, as shown in Fig. F.15. The coverages of the five discovered models reported in Table E.4 are slightly higher. However, the overestimation of the uncertainty measured in the coverage is for all five initializations only between 5.68% and 9.09%. We suspect that the slight overestimation is not only affected by the initialization, but also by the choice of model library and the hyperparameters listed in Appendix D.

Sensitivity-based model selection: For an illustration of the model selection process, see Fig. 9. In Fig. 10, we illustrate the development of the total-order Sobol’ indices for increasing deformation for all 11 tests and associated measured stress components. From the results, we can observe that the stresses in the various mechanical tests are sensitive to different terms in the SEF. This is expected due to the direction-dependent properties of the anisotropic material. In the BT tests, the stress component σ_{ff} in the fiber-direction is dominated by the term based on the invariant I_{4f} and the component σ_{nn} in the normal direction is more sensitive to the term based on the invariant I_{4n} and the isotropic invariant I_2 . The shear stresses in the fiber-shear plane σ_{fs} and σ_{sf} and fiber-normal plane σ_{fn} and σ_{nf} clearly show sensitivity to the respective eighth invariants I_{8fs} and I_{8fn} for small to medium deformation ranges. As deformations increase, the influence of terms based on the eighth invariants decreases, and in particular the terms based on I_2 and \bar{I}_{4f} gain importance. In contrast, the sensitivity of the shear stresses in the shear-normal plane σ_{sn} and σ_{ns} is clearly dominated by the isotropic second invariant I_2 . Similar to the isotropic test case, the sensitivities are generally not constant and may vary with increasing deformation.

3.2.2. Experimental data

Finally, we apply the framework presented in Section 2 to the experimental dataset collected in mechanical tests with anisotropic human cardiac tissue. The structure of the dataset is described at the beginning of the section and is identical to that of the synthetic dataset that we considered before in Section 3.2.1.

GP posterior: The GP posterior for all mechanical tests is shown in the appendix, see Fig. F.16. The coverage estimation results in a total estimated coverage of the centered 95%-interval of $EC_{95\%} = 93.75\%$ and thus indicates that the GP posterior correctly reflects the uncertainty in the measured data.

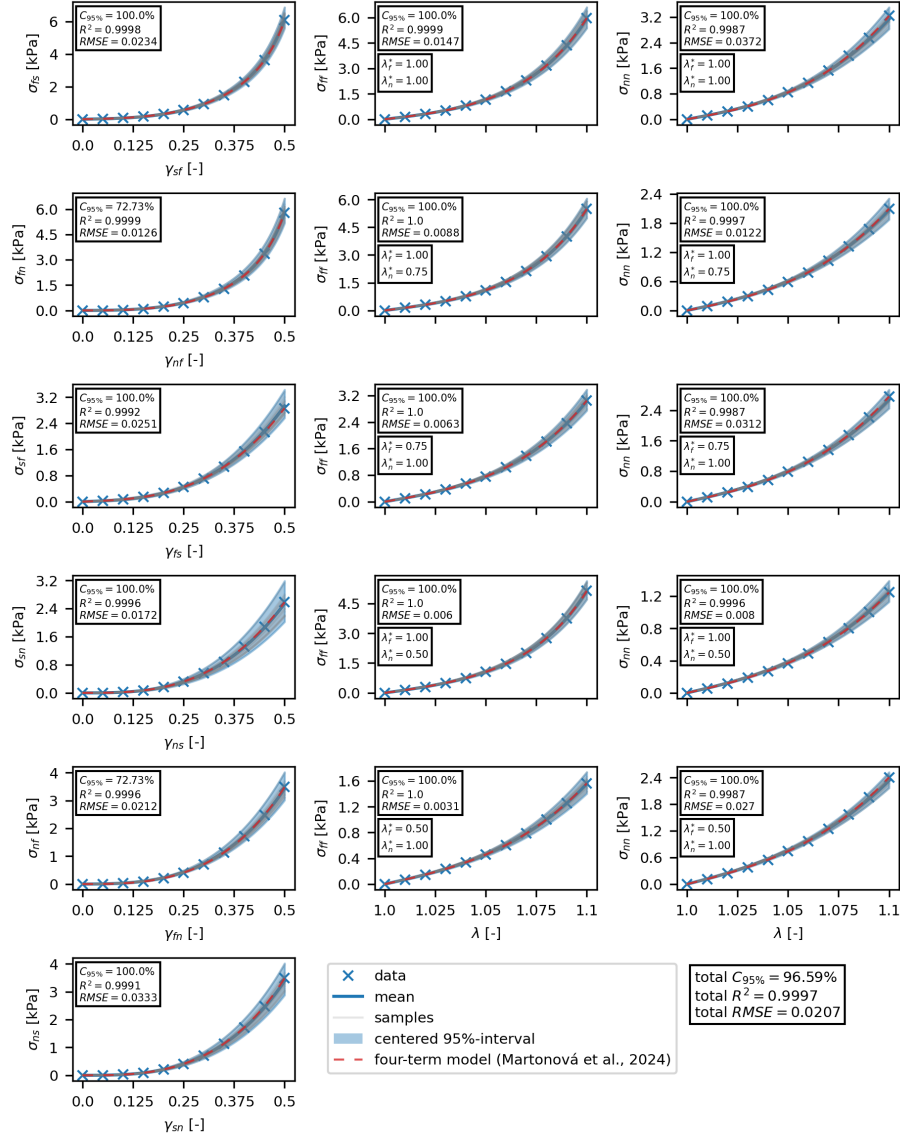


Fig. 8: Synthetic anisotropic test case: Distilled interpretable statistical model. The illustrations show the mean stress-deformation functions, the centered 95%-intervals, some random stress-deformation function samples as well as the individual and total validation metrics for the six SS and five BT tests. The RMSE and the R^2 refer to the mean stress-deformation functions, respectively, and show a good fit. In addition, the total estimated coverage is close to 95% and thus indicates a good estimation of the uncertainty.

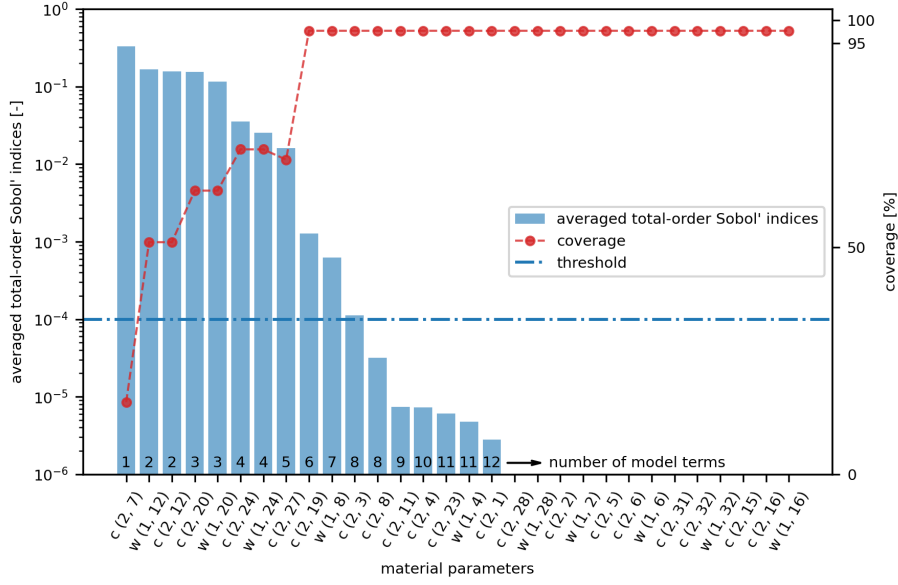


Fig. 9: Synthetic anisotropic test case: Illustration of the model selection process based on the sensitivity analysis. The bars show the total-order Sobol' indices for each material parameter averaged over all mechanical tests, observed stress components and discretization points in their descending order, calculated according to (34). The blue dashed-dotted line indicates the threshold of the total-order Sobol' index below which the material parameters are considered non-relevant. The numbers at the bottom of the bars indicate the total number of model terms when the model term associated with the corresponding material parameter is added to the discovered model. In addition, the red dotted line illustrates how the coverage develops with increasing model size. Note that the estimated coverage may differ slightly after the refinement of the discovered model in the fourth step of the framework.

Note that the GP posterior is not physically consistent in a few cases, e.g., in the BT test for $\lambda_f^* = 1.0$ and $\lambda_n^* = 0.5$. A non-physical GP posterior may lead to a mismatch between the distributions, i.e., a Wasserstein-1 distance greater than zero, but the statistical model is ultimately physically consistent by construction of the model library for the SEF, see Section 2.

Discovered model: The minimization of the Wasserstein-1 distance between the GP posterior and the statistical model yields the following explicit form of

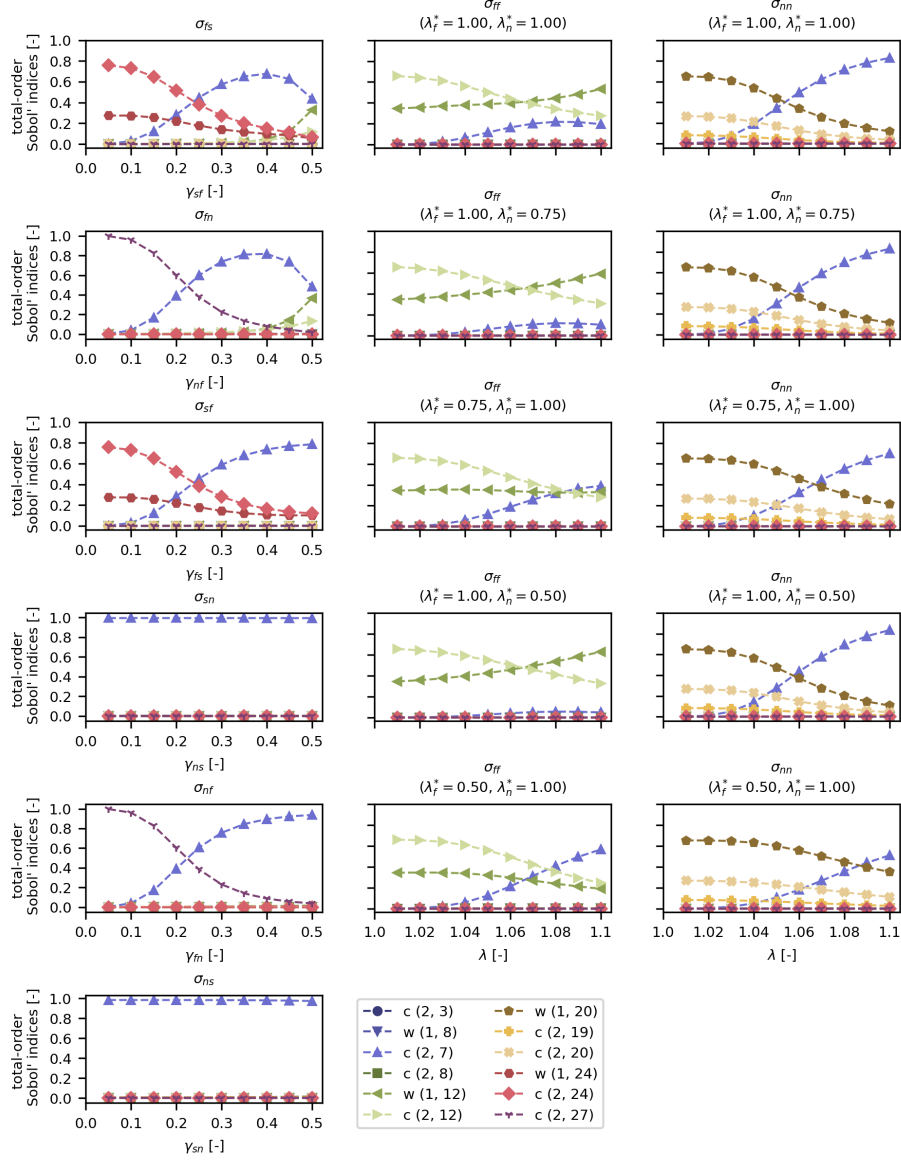


Fig. 10: Synthetic anisotropic test case: Development of total-order Sobol' indices over the course of the mechanical tests. From the results we can make the following observations: **(i)** Different mechanical tests activate different subsets of SEF terms, i.e., terms that are negligible in one deformation mode can dominate in another, and **(ii)** term importance varies with deformation level. Overall, the deformation-dependent Sobol' analysis clarifies how anisotropic mechanisms emerge under different loading paths and illustrates that the discovered model structure is shaped by both deformation mode and deformation range.

the isochoric SEF

$$\begin{aligned}
\overline{W}(\mathbf{F}, \{\mathbf{M}^{(i)}\}_{i=1}^{n_M}; \tilde{\boldsymbol{\kappa}}) = & c^{(2,5)} [I_2 - 3] + c^{(2,6)} \left(\exp(w^{(1,6)} [I_2 - 3]) - 1 \right) \\
& + c^{(2,7)} [I_2 - 3]^2 \\
& + c^{(2,12)} \left(\exp(w^{(1,12)} [\bar{I}_{4f} - 1]^2) - 1 \right) \\
& + c^{(2,16)} \left(\exp(w^{(1,16)} [\bar{I}_{4s} - 1]^2) - 1 \right) \\
& + c^{(2,20)} \left(\exp(w^{(1,20)} [\bar{I}_{4n} - 1]^2) - 1 \right) \\
& + c^{(2,23)} [I_{8fs}]^2,
\end{aligned} \tag{48}$$

where the distribution of the reduced material parameters is approximated by the NF $p_{\tilde{\boldsymbol{\kappa}}}(\tilde{\boldsymbol{\kappa}}; \Phi^*)$ and is shown in Fig. 11. The sensitivity analysis with respect to the initialization of the NNs demonstrates the robustness of the proposed framework for the experimental anisotropic dataset. For all five initializations of the NNs involved, the same model structure defined in (48) was consistently discovered, see Table E.5.

The distribution of the stress-deformation functions induced by the parameter distribution is illustrated in Fig. 12. The quality of the fit is with $R^2 = 0.9352$ and $\text{RMSE} = 0.3441$ comparable to the one observed with the four-term model (46) previously discovered in [26] ($R^2 = 0.9239$, $\text{RMSE} = 0.3729$). However, the estimated coverage of the centered 95%-interval is only $\text{EC}_{95\%} = 34.66\%$ and thus significantly lower than the target value of 95%. Almost identical values for the validation metrics are obtained for the remaining four initializations.

Recall that for the synthetic anisotropic dataset with artificial noise, we achieved both a good mean fit and good coverage, as reported in Section 3.2.1. We have thus demonstrated that our framework is generally capable of reliably discovering statistical anisotropic constitutive models. However, in the synthetic test case, we generated the dataset using terms from the same model library that was subsequently used for model discovery.

In contrast, for the experimental dataset, the same model library may lack flexibility to some extent. A lack of flexibility is strongly related to possibly incorrect modeling assumptions or missing physics. An example of an incorrect assumption would be that the actual orientation of the tissue fibers does not exactly match the orientation assumed in the model library. In addition, the tested cardiac tissue may exhibit viscous effects that are not taken into account in the model library. If the assumptions made when formulating the model library do not accurately reflect reality, then the library's flexibility is insufficient, and the incorrect assumptions will likely induce a model-reality mismatch. For a discussion on the modeling assumptions and missing physics in the constitutive model formulation, we refer to [81, 82]. Other possible reasons for the slight deterioration in mean fit and low estimated coverage compared to the synthetic dataset could be measurement artifacts.

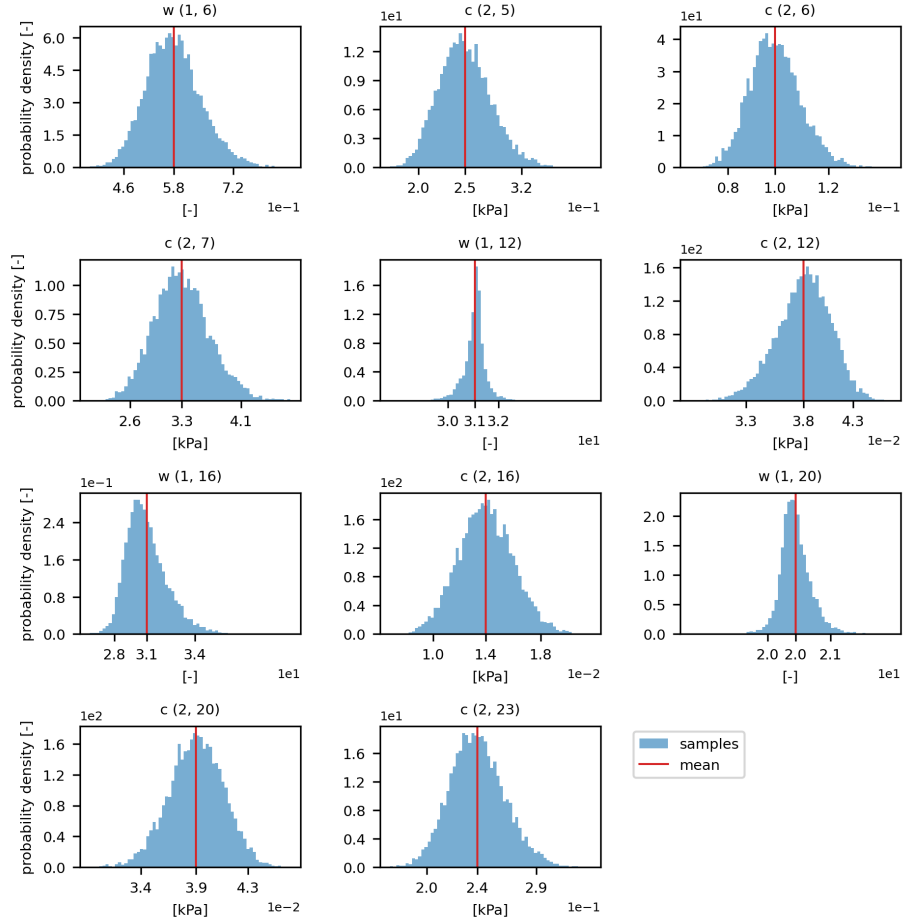


Fig. 11: Experimental anisotropic test case: Distilled distribution of the material parameters after the sensitivity analysis and model refinement. The distribution over stress-deformation functions induced by this parameter distribution is shown in Fig. 12.

Furthermore, we point out that a reasonable mean fit is not a sufficient condition for accurate coverage. The requirements for the flexibility of the model library are significantly higher for uncertainty quantification than for achieving a good mean fit. For uncertainty quantification, the model library must be flexible enough to model all physically admissible stress-deformation functions from the GP posterior, not just the one function that represents a good mean fit.

Sensitivity-based model selection: For information on the model selection process, the reader is referred to Fig. 13. In Fig. 14, we illustrate the development of the total-order Sobol' indices with increasing deformation for all 11 mechanical tests and associated stress components. The results show that the

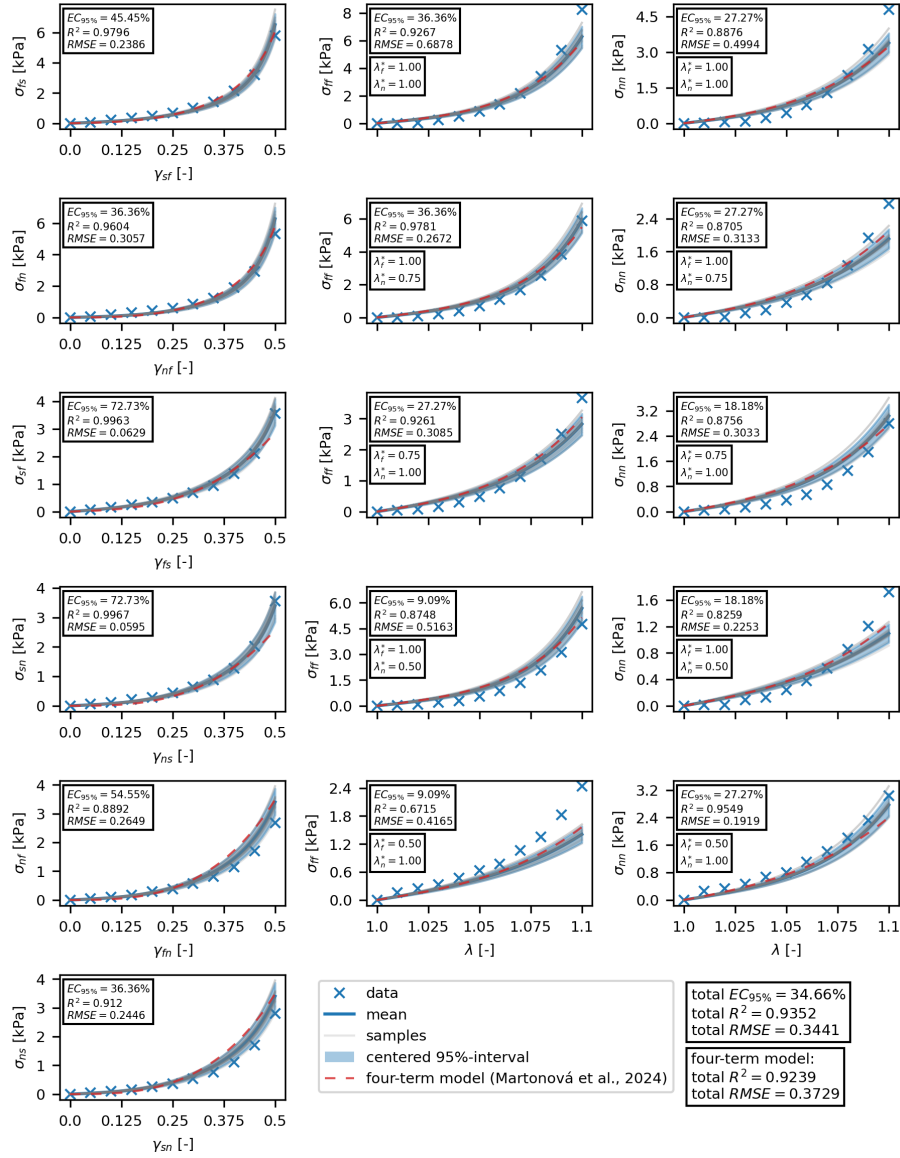


Fig. 12: Experimental anisotropic test case: Distilled interpretable statistical model. The illustrations show the mean stress-deformation functions, the centered 95 %-intervals, some random stress-deformation function samples as well as the individual and total validation metrics for the six SS and five BT tests. The RMSE and the R^2 refer to the mean stress-deformation functions, respectively. For comparison, we also show the four-term model from (46) that was discovered for the experimental dataset in [26].

relevance of individual terms in the SEF is strongly dependent on the deformation mode, loading direction, and deformation level, reflecting the anisotropic behavior of the cardiac tissue. Across the BT tests, the Sobol’ indices exhibit a hierarchy of dominant mechanisms. The normal stress σ_{ff} in the fiber-direction is primarily governed by the fiber reinforcement term $\bar{I}_{4\text{f}}$, whereas the transverse normal stress σ_{nn} is primarily governed by the corresponding transverse reinforcement term $\bar{I}_{4\text{n}}$. This behavior is consistent with the experimentally observed preferential stiffness along the myocardial fiber-direction. In addition, there is evidence that, under loading transverse to the fibers, the load is shared by secondary structural directions (sheet and sheet-normal) that increasingly contribute at higher stretches. This motivates the use of separate direction-specific reinforcement terms in constitutive models [83, 84]. In contrast to this anisotropic dominance, both stress components show an almost identical deformation-dependent isotropic pattern with respect to I_2 . In the small-deformation regime the linear contribution is most influential, whereas at larger stretches the non-linear contribution of I_2 becomes dominant, reflecting an amplification of higher-order isotropic non-linearities with increasing deformation. That is, the Sobol’ indices analysis suggests a progressive activation of non-linear stress contributions.

For all shear components, the response at small shear strains is governed by the linear isotropic contribution of I_2 , while at intermediate shear strains its quadratic form becomes most influential. Toward the largest shear deformations, the contribution of I_2 decreases again. This coincides with an increase in the sensitivity of model terms based on anisotropic invariants, so that anisotropic mechanisms become non-negligible precisely in the high-shear regime. The observed relevance of direction-specific reinforcement terms is standard for myocardium and other fibrous soft tissues to represent interactions between preferred directions under shear [83, 84]. Our analysis suggests that the coupling term $I_{8\text{fs}}$ enters only as a secondary contribution, rather than acting as the primary driver of the shear response in these experiments. This is consistent with reported myocardial shear measurements [85, 86]. In this context, the deformation-dependent Sobol’ analysis provides an interpretation of how different structural mechanisms encoded in the invariant formulation are emphasized under different loading paths and highlights that the specific form of the discovered constitutive model is not only influenced by the deformation modes but by the deformation range explored in the experimental setup.

4. Conclusion and outlook

In this contribution, we proposed a versatile and general statistical framework for uncertainty quantification in supervised model discovery. The key idea behind this framework is to distill the information and uncertainty encoded in a Gaussian process posterior that augments the available noisy stress-deformation data into a material constitutive model. Sparsity of the discovered model is promoted by a Sobol’ sensitivity analysis. As a result, we ultimately obtain interpretable and sparse material constitutive models and a joint probability

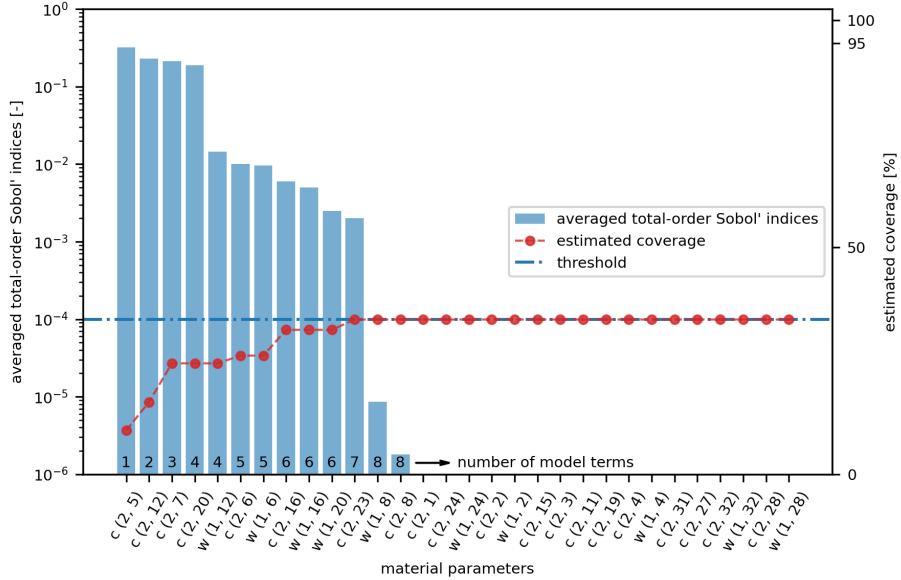


Fig. 13: Experimental anisotropic test case: Illustration of the model selection process based on the sensitivity analysis. The bars show the total-order Sobol' indices for each material parameter averaged over all mechanical tests, observed stress components and discretization points in their descending order, calculated according to (34). The blue dashed-dotted line indicates the threshold of the total-order Sobol' index below which the material parameters are considered non-relevant. The numbers at the bottom of the bars indicate the total number of model terms when the model term associated with the corresponding material parameter is added to the discovered model. In addition, the red dotted line illustrates how the empirical coverage develops with increasing model size. Note that the estimated coverage may differ slightly after the refinement of the discovered model in the fourth step of the framework.

distribution of their material parameters, which can be used for uncertainty quantification.

The proposed framework is only partially Bayesian and does not require the selection of a prior for the material parameters. Note that the absence of prior knowledge is the original motivation for model discovery. By using normalizing flows for density estimation, the framework is able to represent complex and high-dimensional joint probability distributions of the sought material parameters.

We demonstrated the capability of our framework for several test cases, including experimental datasets with isotropic and anisotropic hyperelastic materials. The results for the experimental isotropic and synthetic anisotropic data clearly show that the mean stress-deformation functions of the discovered statistical models are close to the data with only minor deviations. The coverage estimation also indicated a well-calibrated estimate of the uncertainties. For the experimental anisotropic dataset, the quality of the mean fit is comparable to

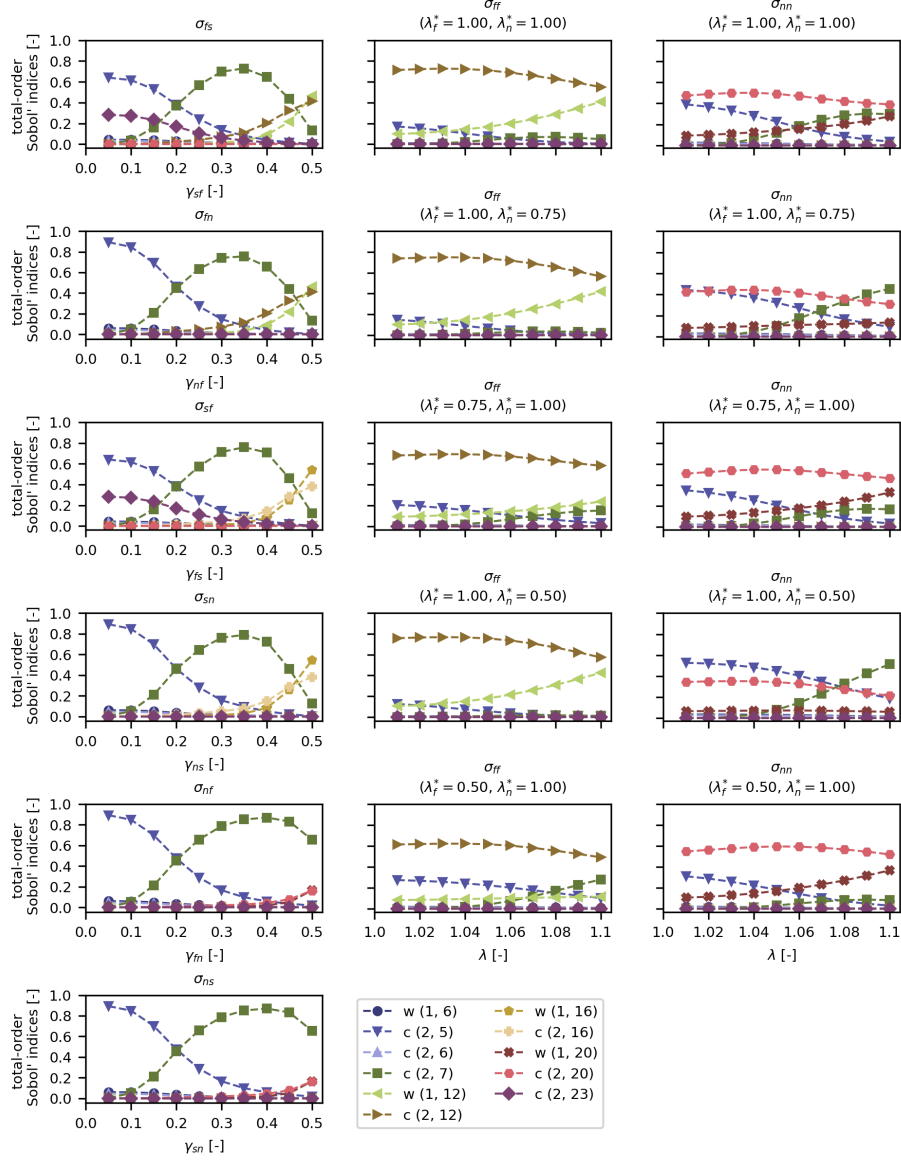


Fig. 14: Experimental anisotropic test case: Development of total-order Sobol' indices over the course of the mechanical tests. From the results we can make the following observations: **(i)** Different mechanical tests activate different subsets of SEF terms, i.e., terms that are negligible in one deformation mode can dominate in another, and **(ii)** term importance varies with deformation level. For the anisotropic test case, this deformation-dependent sensitivity of the model terms provides a data-driven interpretation of which isotropic and direction-specific mechanisms are actually supported by the dataset.

the reference solution reported in [26]. However, the mean fit has a lower accuracy compared to our synthetic test case and uncertainties are underestimated. Possible reasons for the observed accuracy and coverage deterioration could be measurement artifacts and incorrect modeling assumptions, e.g., with regard to fiber orientation. In particular, we suspect incorrect modeling assumptions and missing physics, such as viscous effects, to cause a lack of flexibility of the model library. In order to better capture the uncertainties in the experimental anisotropic test case, model libraries with more flexibility are required that take into account any missing physics and also fiber dispersion, as proposed, e.g., in [87]. For a discussion on the modeling assumptions and missing physics in the constitutive model formulation, the reader is referred to [81, 82].

In addition, our sensitivity analyses show that the contributions of the selected model terms vary for different mechanical tests but also for different levels of deformation in the same test. We therefore believe that Sobol’ indices are a promising technique to get further insights into the model selection process and to support informed decisions in model discovery. Moreover, sensitivity analysis also allows us to optimize the design of the model discovery problem, including the experimental setup and the formulation of the model library.

We believe that our framework is a promising approach to uncertainty quantification in model discovery with potential for further developments and applications beyond continuum solid mechanics. Unlike the model library, the Gaussian process posterior is currently not yet constrained to physically admissible stress-deformation functions but is only conditioned on data. Therefore, future work is required to add physical constraints to the Gaussian process posterior which may improve the framework’s performance. The monotonicity constraint of the stress-deformation function, e.g., could be fulfilled by using monotonic Gaussian process flows [88]. One possible approach to correlate the stress components with each other is to model the strain energy density function by a correlated multi-output GP, as proposed, e.g., by [37]. The stresses could then be obtained by deriving the correlated multi-output GP with respect to the kinematic quantities. However, this approach is not straightforward and requires further investigations.

Furthermore, future research should focus on ensuring that the Gaussian process posterior correctly estimates the uncertainty in the data, since the Gaussian process ultimately represents the target distribution. We believe that it could be promising to infer all hyperparameters of the GP posterior, including those of the error model, in a full Bayesian setting. The kernel length scales would then no longer need to be adopted, and the error parameters would no longer be assumed to be known. However, the full Bayesian approach requires the selection of priors for both the error model parameters and the kernel hyperparameters, which is not straightforward. There is also no guarantee that the full Bayesian approach results in well-calibrated uncertainty of the GP posterior.

We also aim to improve the error model for the measurement data. We currently assume that the contribution of sample variability to the overall error is independently distributed, which generally does not fully reflect reality. One

option for modeling the variability term in the error model more accurately is to use non-stationary Gaussian processes, as done, e.g., in [89].

We expect that our framework can generally be applied to any constitutive model library formulated as a series expansion with linear and non-linear parameters, c.f. (9). In addition, the application to neural network-based constitutive models that rely on function composition is expected to be possible. However, in the future, it still needs to be investigated whether normalizing flows can also approximate the distribution over material parameters for model libraries and neural networks with a large number of parameters. Finally, we intend to extend the current framework to inelastic material behavior and the unsupervised setting.

CRedit authorship contribution statement

David Anton: Conceptualization, Methodology, Software, Validation, Investigation, Data Curation, Writing - Original Draft, Writing - Review & Editing, Visualization **Henning Wessels:** Conceptualization, Resources, Writing - Original Draft, Writing - Review & Editing, Supervision, Funding acquisition **Ulrich Römer:** Methodology, Writing - Original Draft, Writing - Review & Editing, Supervision **Alexander Henkes:** Methodology, Writing - Review & Editing, Supervision **Jorge-Humberto Urrea-Quintero:** Conceptualization, Methodology, Investigation, Writing - Original Draft, Writing - Review & Editing, Supervision

Declaration of competing interest

The authors declare that they have no known competing financial interests or personal relationships that could have appeared to influence the work reported in this paper.

Acknowledgments

David Anton and Henning Wessels acknowledge support in the project DFG 501798687: *"Monitoring data driven life cycle management with AR based on adaptive, AI-supported corrosion prediction for reinforced concrete structures under combined impacts"* which is a subproject of SPP 2388: *"Hundred plus - Extending the Lifetime of Complex Engineering Structures through Intelligent Digitalization"* funded by the DFG. Alexander Henkes acknowledges support by an ETH Zurich Postdoctoral Fellowship. The authors also acknowledge the valuable comments of the anonymous reviewers, which led to substantial improvements of the manuscript.

Data availability

Our research code is available on GitHub and Zenodo [49].

Appendix A. Details on variational perspective

Instead of targeting $p(\boldsymbol{\kappa} \mid \mathcal{D})$ directly, we now detail the two-step approach with a GP data surrogate. We assume that there is an unknown, true, stress-deformation function f such that the data is generated as

$$P^{(i)} = f(\mathbf{F}^{(i)}) + \epsilon^{(i)}, \quad i = 1, \dots, n_d, \quad (\text{A.1})$$

and $\mathcal{D} = \{(\mathbf{F}^{(i)}, P^{(i)})\}_{i=1}^{n_d}$. Moreover $\mathbf{f} \in \mathbb{R}^{n_s}$ represents f evaluated at a different grid of n_s deformation tensors. The library induces a model of \mathbf{f} , given by $\mathbf{T}_M : \boldsymbol{\kappa} \mapsto \mathbf{T}_M(\boldsymbol{\kappa}) \in \mathbb{R}^{n_s}$. Our only aim here is to motivate the variational approach and to establish connections and therefore, we introduce some strong simplifying assumptions. We model f , resp. \mathbf{f} as a GP and assume that the model library is expressive enough so that for a specific $\boldsymbol{\kappa}^*$, $\mathbf{f} = \mathbf{T}_M(\boldsymbol{\kappa}^*)$ holds for all possible GP realizations. We also assume that \mathbf{T}_M is bijective.

We proceed by factoring the joint probability distribution $p(\boldsymbol{\kappa}, \mathcal{D}, \mathbf{f})$ as

$$p(\boldsymbol{\kappa}, \mathcal{D}, \mathbf{f}) = p(\boldsymbol{\kappa}, \mathbf{f} \mid \mathcal{D}) p(\mathcal{D}) \quad (\text{A.2a})$$

$$= p(\boldsymbol{\kappa} \mid \mathbf{f}, \mathcal{D}) p(\mathbf{f}, \mathcal{D}) \quad (\text{A.2b})$$

$$= p(\boldsymbol{\kappa} \mid \mathbf{f}) p(\mathbf{f} \mid \mathcal{D}) p(\mathcal{D}), \quad (\text{A.2c})$$

where we additionally assume conditional independence of $\boldsymbol{\kappa}$ and \mathcal{D} , given \mathbf{f} , for simplicity. From equating (A.2a) and (A.2b), we obtain the joint posterior

$$p(\boldsymbol{\kappa}, \mathbf{f} \mid \mathcal{D}) = \frac{p(\boldsymbol{\kappa} \mid \mathbf{f}, \mathcal{D}) p(\mathbf{f}, \mathcal{D})}{p(\mathcal{D})} \quad (\text{A.3a})$$

$$= p(\boldsymbol{\kappa} \mid \mathbf{f}) p(\mathbf{f} \mid \mathcal{D}), \quad (\text{A.3b})$$

where (A.3b) is obtained using (A.2c) and $p(\mathbf{f} \mid \mathcal{D})$ is the GP posterior distribution.

For the following argument, as a distance in the variational approach (3), we consider the Kullback-Leibler divergence $D = \text{KL}$. For a bijective and sufficiently smooth \mathbf{T}_M , the density $\mathbf{T}_{M\#} p_{\boldsymbol{\kappa}}(\mathbf{f})$ can be characterized as

$$\mathbf{T}_{M\#} p_{\boldsymbol{\kappa}}(\mathbf{f}) = p_{\boldsymbol{\kappa}}(\mathbf{T}_M^{-1}(\mathbf{f})) |\det \mathbf{J}_{\mathbf{T}_M^{-1}}(\mathbf{f})|. \quad (\text{A.4})$$

Then, the KL-divergence can be recast as

$$\text{KL}(\mathbf{T}_{M\#} p_{\boldsymbol{\kappa}}(\mathbf{f}), p(\mathbf{f} \mid \mathcal{D})) = \int_{\mathcal{K}} p_{\boldsymbol{\kappa}}(\boldsymbol{\kappa}) \log \frac{p_{\boldsymbol{\kappa}}(\boldsymbol{\kappa})}{p(\mathbf{f} = \mathbf{T}_M(\boldsymbol{\kappa}) \mid \mathcal{D}) \cdot |\det \mathbf{J}_{\mathbf{T}_M}(\boldsymbol{\kappa})|} d\boldsymbol{\kappa}, \quad (\text{A.5})$$

after pulling the integral back to the parameter domain \mathcal{K} . Hence, the minimizer is obtained as

$$p_{\boldsymbol{\kappa}}^*(\boldsymbol{\kappa}) = p(\mathbf{f} = \mathbf{T}_M(\boldsymbol{\kappa}) \mid \mathcal{D}) \cdot |\det \mathbf{J}_{\mathbf{T}_M}(\boldsymbol{\kappa})|. \quad (\text{A.6})$$

At the same time, by the change of variables formula

$$p(\boldsymbol{\kappa} \mid \mathcal{D}) = p(\mathbf{f} = \mathbf{T}_M(\boldsymbol{\kappa}) \mid \mathcal{D}) |\det \mathbf{J}_{\mathbf{T}_M}(\boldsymbol{\kappa})| \quad (\text{A.7})$$

and hence $p(\boldsymbol{\kappa} \mid \mathcal{D}) = p_{\boldsymbol{\kappa}}^*(\boldsymbol{\kappa})$. Note that in the general case, the push-forward density can easily concentrate on a lower dimensional set and the Kullback-Leibler divergence in (A.5) becomes infinite. Since we apply (A.5) in a much more general and realistic setting than assumed in the above argument, we use the Wasserstein-1 distance throughout this paper instead.

Appendix B. Observation maps and deformation filters definitions

This appendix provides the definitions of the observation maps and deformation filters for all numerical test cases. For an introduction to our notation, the reader is referred to Section 2.3.

Appendix B.1. Observation maps definitions

The observation map $\mathbf{O}^{(t,q)} : \mathbb{R}^{3 \times 3} \rightarrow \mathbb{R}$ is used to filter out the stress components $q \in \{1, \dots, n_q^{(t)}\}$ observed in the respective mechanical test $t \in \{1, \dots, n_t\}$. In Appendix B.1.1 and Appendix B.1.2, we define the observation maps that we use for the Treloar and the anisotropic datasets, respectively.

Appendix B.1.1. Treloar dataset

The Treloar dataset comprises one uniaxial tension (UT), equibiaxial tension (EBT) and pure shear (PS) test. For a clear assignment of the tests, the integer values of the index for the mechanical test t are replaced by their respective abbreviations such that $t \in \{\text{UT}, \text{EBT}, \text{PS}\}$. In all three mechanical tests, only the principal Piola-Kirchhoff stress component P_{11} is observed, i.e., $n_q^{(\text{UT})} = n_q^{(\text{EBT})} = n_q^{(\text{PS})} = 1$. The observation maps are thus defined as

$$\begin{aligned} \mathbf{O}^{(\text{UT},1)}(\mathbf{P}) &= P_{11}, \\ \mathbf{O}^{(\text{EBT},1)}(\mathbf{P}) &= P_{11}, \\ \mathbf{O}^{(\text{PS},1)}(\mathbf{P}) &= P_{11}. \end{aligned} \tag{B.1}$$

Appendix B.1.2. Anisotropic dataset

The anisotropic dataset we consider in this paper includes a total of six simple shear (SS) and five biaxial tension (BT) tests. According to [48], the three mutually orthogonal directions of the anisotropic human cardiac tissue are the fiber (f), shear (s) and normal (n) directions. In each SS test, the corresponding shear stress component of the Cauchy stress tensor is observed, and $n_q^{(\text{SS})} = 1$. We again assign the corresponding abbreviations to the integer values of the mechanical test index t . The observation maps for the shear tests are then defined as follows

$$\begin{aligned} \mathbf{O}^{(\text{SS}_{\text{sf}},1)}(\boldsymbol{\sigma}) &= \sigma_{\text{fs}}, & \mathbf{O}^{(\text{SS}_{\text{fs}},1)}(\boldsymbol{\sigma}) &= \sigma_{\text{sf}}, \\ \mathbf{O}^{(\text{SS}_{\text{nf}},1)}(\boldsymbol{\sigma}) &= \sigma_{\text{fn}}, & \mathbf{O}^{(\text{SS}_{\text{fn}},1)}(\boldsymbol{\sigma}) &= \sigma_{\text{nf}}, \\ \mathbf{O}^{(\text{SS}_{\text{ns}},1)}(\boldsymbol{\sigma}) &= \sigma_{\text{sn}}, & \mathbf{O}^{(\text{SS}_{\text{sn}},1)}(\boldsymbol{\sigma}) &= \sigma_{\text{ns}}. \end{aligned} \tag{B.2}$$

In the BT tests, the principal stresses in the fiber and in the normal direction are measured, so that $n_q^{(\text{BT})} = 2$. The observation maps for all five BT tests are identical and yield

$$\mathbf{O}^{(\text{BT},1)}(\boldsymbol{\sigma}) = \sigma_{\text{ff}}, \quad \mathbf{O}^{(\text{BT},2)}(\boldsymbol{\sigma}) = \sigma_{\text{nn}}. \quad (\text{B.3})$$

Appendix B.2. Deformation filters definitions

In order to reduce the number of GP inputs and thus hyperparameters, we introduce the reduced deformation vector $\boldsymbol{\Lambda}^{(t,q)} = \mathbf{F}_{\mathcal{P}_q^{(t)}}(\mathbf{F}) \in \mathbb{R}^{n_\Lambda^{(t,q)}}$. The reduced deformation vector $\boldsymbol{\Lambda}^{(t,q)}$ contains only the deformation gradient components that are relevant to predict the stress component $\mathcal{P}_q^{(t)}$ for the components $q \in \{1, \dots, n_q^{(t)}\}$ observed in the respective mechanical test $t \in \{1, \dots, n_t\}$. In Appendix B.2.1 and Appendix B.2.2, we define the deformation filters $\mathbf{F}_{\mathcal{P}_q^{(t)}}$ used for the Treloar and the anisotropic datasets, respectively.

Appendix B.2.1. Treloar dataset

In the case of the Treloar dataset, in all three mechanical tests, only the stress component P_{11} is measured. Accordingly, only one deformation filter is required, which is defined as follows

$$\mathbf{F}_{P_{11}}(\mathbf{F}) = [F_{11}, F_{22}]^\top. \quad (\text{B.4})$$

Note that for incompressible materials, the deformation gradient component F_{33} can be uniquely derived from the other two and is therefore not independent.

Appendix B.2.2. Anisotropic dataset

The anisotropic dataset includes six simple shear (SS) and five biaxial tension (BT) tests and we need eight deformation filters which are defined as follows

$$\begin{aligned} \mathbf{F}_{\sigma_{\text{sf}}}(\mathbf{F}) &= F_{\text{fs}}, & \mathbf{F}_{\sigma_{\text{fs}}}(\mathbf{F}) &= F_{\text{sf}}, \\ \mathbf{F}_{\sigma_{\text{nf}}}(\mathbf{F}) &= F_{\text{fn}}, & \mathbf{F}_{\sigma_{\text{fn}}}(\mathbf{F}) &= F_{\text{nf}}, \\ \mathbf{F}_{\sigma_{\text{ns}}}(\mathbf{F}) &= F_{\text{sn}}, & \mathbf{F}_{\sigma_{\text{sn}}}(\mathbf{F}) &= F_{\text{ns}}, \\ \mathbf{F}_{\sigma_{\text{ff}}}(\mathbf{F}) &= [F_{\text{ff}}, F_{\text{nn}}]^\top, & \mathbf{F}_{\sigma_{\text{nn}}}(\mathbf{F}) &= [F_{\text{ff}}, F_{\text{nn}}]^\top. \end{aligned} \quad (\text{B.5})$$

Here, the indices refer to the mutually orthogonal directions of the anisotropic human cardiac tissue which are the fiber (f), shear (s) and normal (n) directions.

Appendix C. Centered 95%-intervals and estimated coverage

In this paper, the uncertainty in the discretized stress-deformation functions $\mathbf{f}^{(t,q)}$ is quantified through point-wise 95 %-intervals $\mathcal{C}_{\mathbf{f}}^{(t,q,s)} = [L_{\mathbf{f}}^{(t,q,s)}, U_{\mathbf{f}}^{(t,q,s)}]$. These intervals $\mathcal{C}_{\mathbf{f}}^{(t,q,s)}$ are centered around the mean and contain 95 % of the probability mass, which is formally defined as $P(f^{(t,q,s)} \in \mathcal{C}_{\mathbf{f}}^{(t,q,s)}) = 0.95$. Here, $f^{(t,q,s)}$ is the component s of the vector $\mathbf{f}^{(t,q)} \in \mathbb{R}^{n_s^{(t)}}$.

For the GP posterior, the intervals $\mathcal{C}_{\mathbf{f}}^{(t,q,s)}$ are derived based on the posterior distribution and correspond to credible intervals [57, 31]. For the statistical model, we determine the intervals $\mathcal{C}_{\mathbf{f}}^{(t,q,s)}$ from a finite set of random samples drawn from the statistical model, since the discretized stress-deformation functions are not necessarily normally distributed. In this case, the lower and upper bounds $L_{\mathbf{f}}^{(t,q,s)}$ and $U_{\mathbf{f}}^{(t,q,s)}$ of the interval are set to the values for which 2.5% of the samples lie below or above them, respectively.

As a measure of the validity of the quantified uncertainty in the discretized stress-deformation function $\mathbf{f}^{(t,q)}$, we estimate the coverage in our numerical tests based on the measurement data \mathcal{D} as follows

$$\text{EC}_{95\%}^{(t,q)} = \frac{1}{100} \frac{1}{n_d^{(t)}} \sum_{d=1}^{n_d^{(t)}} 1_{\mathcal{C}_{\mathbf{f}}}(f^{(t,q,d)}) \quad (\text{C.1})$$

where $1_{\mathcal{C}_{\mathbf{f}}}$ is an indicator function defined as

$$1_{\mathcal{C}_{\mathbf{f}}}(f^{(t,q,d)}) = \begin{cases} 1, & \text{if } f^{(t,q,d)} \in \mathcal{C}_{\mathbf{f}} \\ 0, & \text{otherwise} \end{cases}. \quad (\text{C.2})$$

Accordingly, the total estimated coverage for all tests is calculated as follows

$$\text{EC}_{95\%} = \frac{1}{100} \frac{1}{n_t} \sum_{t=1}^{n_t} \frac{1}{n_q^{(t)} n_d^{(t)}} \sum_{q=1}^{n_q^{(t)}} \sum_{d=1}^{n_d^{(t)}} 1_{\mathcal{C}_{\mathbf{f}}}(f^{(t,q,d)}). \quad (\text{C.3})$$

Remark: The term coverage is well-defined in frequentist statistics and is calculated using the true stress value. From a frequentist point of view, the uncertainty is correctly quantified if for $n_d^{(t)} \rightarrow \infty$ the measures $\text{EC}_{95\%}^{(t,q)}$ and $\text{EC}_{95\%}$ converge to 95%. However, since the true stress values are generally unknown for experimental data, we use the measured stress values from the dataset for validation. Consequently, the measures $\text{EC}_{95\%}^{(t,q)}$ and $\text{EC}_{95\%}$ are only estimates for the true coverage. In contrast, in the synthetic numerical test, we use the known true stress values to determine the coverage, which are also calculated according to (C.1)–(C.3) but referred to as $C_{95\%}^{(t,q)}$ and $C_{95\%}$, respectively. Note that even in the synthetic test case, the coverage is only an estimate, since the amount of available data is generally limited in our numerical test cases.

Appendix D. Hyperparameters and scalability

In Table D.2, we summarize the hyperparameters of the GP prior, NF, Wasserstein-1 minimization and the Sobol’ sensitivity analysis involved in the proposed framework for all test cases considered in Section 3. The selection of the hyperparameters is based on the following considerations:

- **GP prior:** We choose a scaled squared-exponential kernel because the sample paths and mean functions of GPs with squared-exponential kernels

are smooth [57]. The results show that the AdamW optimizer with the specified learning rate and number of iterations leads to fast, yet stable, convergence in all numerical tests. As explained in Section 2.4.1, the specified scaling factor for the kernel length scales leads to a reasonable trade-off between physical consistency and our prior knowledge about the variety and uncertainty of the stress-deformation functions.

- **NF:** The standard multivariate normal distribution is a common choice for the base distribution of NFs [42], which we also adopt. We use IAFs since this autoregressive flow is fast to evaluate and scales well to high-dimensional distributions [61], see Section 2.4.2. The NF architecture which includes the number of sub-transformations and the width and depth of the MADE networks was selected based on preliminary tests. Since the width of the MADE network depends on the number of material parameters n_κ , the NF architecture, and thus its capacity, automatically adapts to the size of the model library. Preliminary tests also showed that larger NF architectures with more trainable parameters lead to an increase in training runtime but do not result in a significant improvement in the predictive capabilities of the statistical model.
- **Wasserstein-1 minimization:** The number of function samples for the estimation of the expectation operators in (31) and (32), the number of discretization points $n_s^{(t)}$ per stress-deformation function, and the number of iterations n_{iters}^W were selected systematically by conducting preliminary tests. Further increasing the value of these hyperparameters did not lead to a significant improvement in accuracy. For the remaining hyperparameters, we started with the values used in [43, 70] and adjusted these values to our use case based on the results of preliminary tests. The selected optimizers, learning rates, decay rates and number of iterations n_{iters}^L balance the convergence speed and stability of the iterative optimization procedure. For the Lipschitz-1 penalty coefficient, we found that $\lambda_L = 10$, which is also used as the default value in [70], leads to robust and good results.
- **Sobol' sensitivity analysis:** We use the total-order Sobol' index since it measures the total effect of the corresponding parameter on the variance of the model output and also takes the interactions with the other parameters into account. The total-order Sobol' indices are calculated using the Saltelli sampling method [72, 73] which is a fairly common strategy. The number of samples used to determine the total-order Sobol' indices was chosen to be so large that no significant variation in the indices was observed when the number was increased further. We estimate the minimum and maximum sample bounds from the distilled distribution $p_\kappa(\boldsymbol{\kappa}; \boldsymbol{\Phi})$ to further automate the sensitivity analysis. Furthermore, the threshold for the total-order Sobol' index below which the parameters are considered non-relevant is set to $1 \cdot 10^{-4}$. As explained in Section 2.4.4, there is no

universally suitable threshold. Instead, the threshold must be selected depending on the use case. In Fig. 5, Fig. 9 and Fig. 13, the model selection process is illustrated for the isotropic, the synthetic anisotropic and the experimental anisotropic test case, respectively. These plots show that for all three test cases, the selected threshold for the total-order Sobol’ index achieves a reasonable trade-off between the sparsity of the discovered model and its ability to quantify the uncertainty.

We do not claim to have found the optimal hyperparameters. However, we achieve good results with the selected hyperparameters in all three numerical test cases. In addition, minimization of the Wasserstein-1 distance is robust with the selected hyperparameters, as we show in Appendix E for five different random initializations of the involved NNs for each numerical test case. Furthermore, we note that the research code is freely available in [49] and therefore can be used by the reader for further analysis with different hyperparameters, stress-deformation data, or model libraries.

Finally, we discuss the scalability of the framework presented in this paper in qualitative terms and identify the hyperparameters in Table D.2 that are expected to have the most significant impact on computational costs. The computational costs are mainly influenced by the design of experiments in which the stress-deformation data are collected, the resolution of the discretization, as well as the size of the model library. The larger the number of mechanical tests n_t and discretization points $n_s^{(t)}$ are, the larger the size n_s of the vector with all discretized stress-deformation functions \mathbf{f} defined in (7) is. As the size of \mathbf{f} increases, the size of \mathbf{f}_{GP} in (17) and \mathbf{T}_M in (26) as well as the number of parameters of the NN used as Lipschitz-1 function f_{LN} in (31) and (32) increase. The computational cost for Wasserstein-1 minimization also grows with the number of samples used to estimate the expectation operators in (31) and (32). Furthermore, there is a direct correlation between the size of the model library, on the one hand, and memory consumption and runtime, on the other. The more material parameters κ the model library contains, the larger the dimensionality of their joint probability distribution, which is approximated by the NF. As the complexity of the joint probability distribution of the material parameters increases, the number of trainable parameters of the NF generally must also be increased. In addition, a growing model library also increases the memory consumption and runtime of the sensitivity analysis. However, we found that the Wasserstein-1 minimization is the most computationally intensive step in the proposed framework compared to the inference of the GP posterior and the Sobol’ sensitivity analysis.

Appendix E. Sensitivity with respect to NN initialization

The framework presented in this manuscript uses NNs in both the NF and as Lipschitz-1 function to minimize the Wasserstein-1 distance. Due to the non-convexity of the optimization problem to be solved, the initialization of

Table D.2: Selected hyperparameters of the GP prior, NF, Wasserstein-1 minimization and the Sobol’ sensitivity analysis involved in the proposed framework for each test case considered in Section 3.

hyperparameter	test case		
	Treloar (isotropic)	synthetic anisotropic	experimental anisotropic
Gaussian process (GP) prior			
kernel	scaled squared-exponential [57]		
optimizer for ζ	AdamW [58] learning rate: 0.2		
iterations	10 000		
scaling factor for length scales	0.6		
normalizing flow (NF)			
base distribution	standard multivariate normal		
method	inverse autoregressive flow (IAF) [61]		
sub-transformations	16		
depth / width of MADE network	1 hidden layer / $4n_\kappa$ neurons		
Wasserstein-1 minimization			
samples for estimating expectations	32		
discretization points $n_s^{(t)}$ per stress-deformation function	32		
iterations n_{iters}^L	10		
iterations n_{iters}^W (discovery / refinement step)	20 000 / 10 000		
optimizer for θ	AdamW [58] learning rate: $1 \cdot 10^{-4}$		
optimizer for Φ	RMSprop [90] initial learning rate: $5 \cdot 10^{-4}$ learning rate decay: 0.9999		
Lipschitz-1 penalty coefficient λ_L	10		
Sobol’ sensitivity analysis			
considered sensitivity index	total-order Sobol’ index		
sampling method	Saltelli sampling method [72, 73]		
sampling bounds	minimums and maximums estimated from 8192 samples drawn from $p_\kappa(\boldsymbol{\kappa}; \Phi)$		
threshold	$1 \cdot 10^{-4}$		
samples	$4096(n_\kappa + 2)$		

these NNs may affect the optimization result. For this reason, we test five random initializations of the NNs for each numerical test case. We summarize validation metrics and the structure of the constitutive models discovered in Tables E.3–E.5 for the Treloar, the synthetic anisotropic and the experimental anisotropic test case, respectively. Please note that we always use the same synthetic noisy data in the synthetic anisotropic case and that data generation is not influenced by the random seed. The results presented in this appendix underline that the initialization slightly affects the structure of the discovered models. However, the discovered model structures differ mainly in a few model terms, and no significant differences in structure and validation metrics were found. In summary, the sensitivity analysis shows that the proposed framework is reasonably robust to the initialization of the NNs used within this framework.

Table E.3: Treloar test case: Sensitivity of discovered constitutive model with respect to the random initialization of the involved NNs. This table summarizes the most important results for five different random seeds, such as the validation metrics and the model structure. The results for the random seed 2 are considered representative among the five initializations and are discussed in more detail in Section 3.1.

random seed	0	1	2	3	4
GP posterior					
total EC _{95%} [%]	96.23	96.23	96.23	96.23	96.23
discovered model					
total EC _{95%} [%]	86.79	94.34	92.45	92.45	94.34
total R ²	0.9964	0.9963	0.9964	0.9964	0.9958
total RMSE	0.0947	0.0955	0.0942	0.0942	0.1026
model structure					
$c^{(1,0)}(I_1 - 3)$	✓	✓	✓	✓	✓
$c^{(3,0)}(I_1 - 3)^3$	✓	✓	✓	✓	✓
$c^{(0,1)}(I_2 - 3)$	✓		✓		✓
$c^{(-1)}(\lambda_1^{-1} + \lambda_2^{-1} + \lambda_3^{-1} - 3)$	✓	✓	✓	✓	✓
$c^{(1)}(\lambda_1^1 + \lambda_2^1 + \lambda_3^1 - 3)$	✓	✓	✓	✓	✓

Appendix F. Complementary results

This appendix provides complementary results for the synthetic and experimental anisotropic numerical test cases.

Appendix F.1. Synthetic anisotropic test case

In Fig. F.15, we show the distribution of stress-deformation functions given by the GP posterior. For the discussion of the results for the synthetic anisotropic test case, we refer to Section 3.2.1.

Table E.4: Synthetic anisotropic test case: Sensitivity of discovered constitutive model with respect to the random initialization of the involved NNs. This table summarizes the most important results for five different random seeds, such as the validation metrics and the model structure. The results for the random seed 0 are considered representative among the five initializations and are discussed in more detail in Section 3.2.1. For comparison, the structure of the four-term model [26] used to generate the synthetic dataset is also shown.

random seed	0	1	2	3	4	four-term model [26]
GP posterior						
total $C_{95\%}$ [%]	89.77	89.77	89.77	89.77	89.77	-
discovered model						
total $C_{95\%}$ [%]	96.59	98.86	97.73	95.45	96.02	-
total R^2	0.9997	0.9993	0.9997	0.9996	0.9997	-
total RMSE	0.0207	0.0345	0.0231	0.0239	0.0211	-
model structure						
$c^{(2,1)} [I_1 - 3]$			✓	✓	✓	
$c^{(2,3)} [I_1 - 3]^2$	✓	✓	✓	✓	✓	
$c^{(2,4)} \left(\exp(w^{(1,4)} [I_1 - 3]^2) - 1 \right)$			✓			
$c^{(2,7)} [I_2 - 3]^2$	✓	✓	✓	✓	✓	✓
$c^{(2,8)} \left(\exp(w^{(1,8)} [I_2 - 3]^2) - 1 \right)$	✓	✓	✓	✓	✓	
$c^{(2,12)} \left(\exp(w^{(1,12)} [\bar{I}_{4f} - 1]^2) - 1 \right)$	✓	✓	✓	✓	✓	✓
$c^{(2,19)} [\bar{I}_{4n} - 1]^2$	✓	✓	✓	✓	✓	
$c^{(2,20)} \left(\exp(w^{(1,20)} [\bar{I}_{4n} - 1]^2) - 1 \right)$	✓	✓	✓	✓	✓	✓
$c^{(2,24)} \left(\exp(w^{(1,24)} [I_{8fs}]^2) - 1 \right)$	✓	✓	✓	✓	✓	✓
$c^{(2,27)} [I_{8fn}]^2$	✓					
$c^{(2,28)} \left(\exp(w^{(1,28)} [I_{8fn}]^2) - 1 \right)$		✓	✓	✓	✓	

Table E.5: Experimental anisotropic test case: Sensitivity of discovered constitutive model with respect to the random initialization of the involved NNs. This table summarizes the most important results for five different random seeds, such as the validation metrics and the model structure. The results for the random seed 0 are considered representative among the five initializations and are discussed in more detail in Section 3.2.2. For comparison, the structure of the four-term model previously discovered in [26] using a deterministic model discover approach is also shown.

random seed	0	1	2	3	4	four-term model [26]
GP posterior						
total EC _{95%} [%]	93.75	93.75	93.75	93.75	93.75	-
discovered model						
total EC _{95%} [%]	34.66	34.66	35.23	35.23	34.09	-
total R ²	0.9352	0.9355	0.9358	0.9358	0.9355	0.9239
total RMSE	0.3441	0.3434	0.3426	0.3425	0.3434	0.3729
$c^{(2,5)} [I_2 - 3]$	✓	✓	✓	✓	✓	
$c^{(2,6)} \left(\exp(w^{(1,6)} [I_2 - 3]) - 1 \right)$	✓	✓	✓	✓	✓	
$c^{(2,7)} [I_2 - 3]^2$	✓	✓	✓	✓	✓	✓
$c^{(2,12)} \left(\exp(w^{(1,12)} [\bar{I}_{4f} - 1]^2) - 1 \right)$	✓	✓	✓	✓	✓	✓
$c^{(2,16)} \left(\exp(w^{(1,16)} [\bar{I}_{4s} - 1]^2) - 1 \right)$	✓	✓	✓	✓	✓	
$c^{(2,20)} \left(\exp(w^{(1,20)} [\bar{I}_{4n} - 1]^2) - 1 \right)$	✓	✓	✓	✓	✓	✓
$c^{(2,23)} [I_{8fs}]^2$	✓	✓	✓	✓	✓	
$c^{(2,24)} \left(\exp(w^{(1,24)} [I_{8fs}]^2) - 1 \right)$						✓

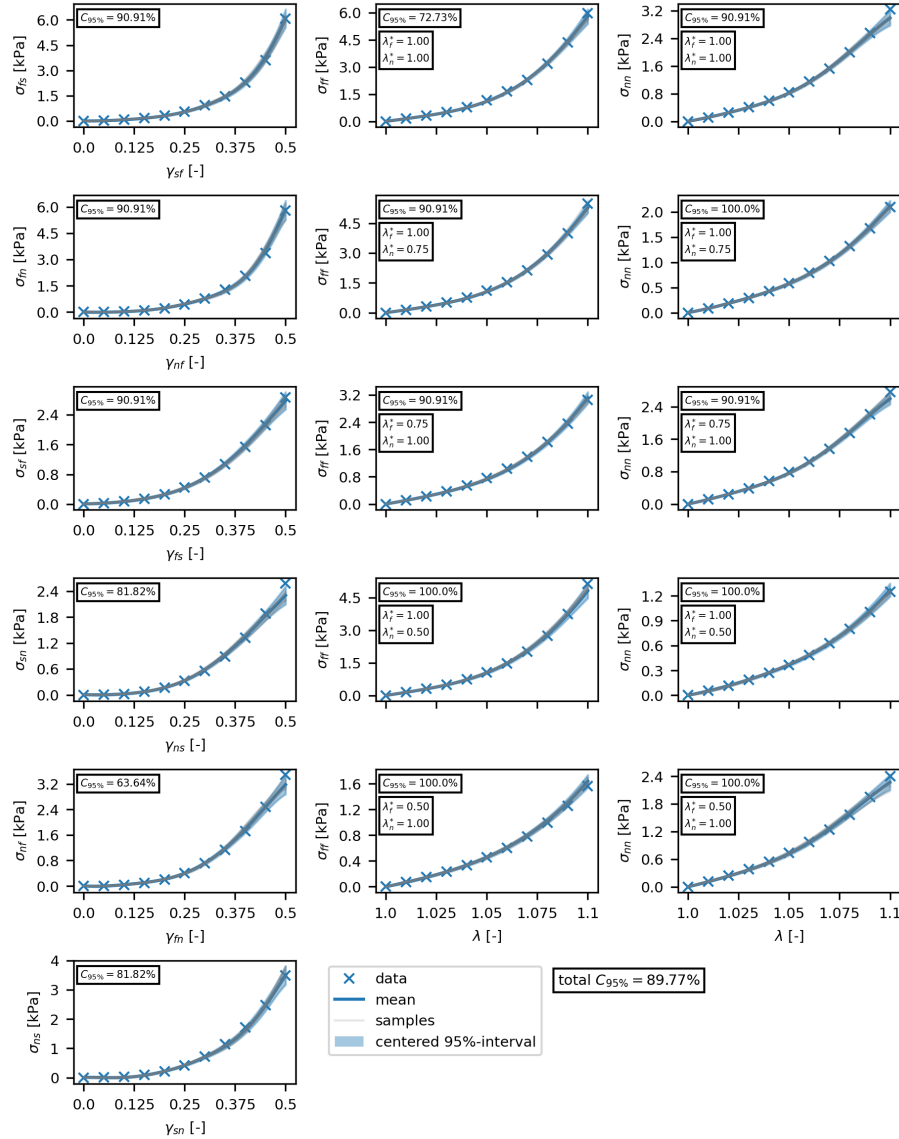


Fig. F.15: Synthetic anisotropic test case: GP posterior. The illustrations show the GP posterior mean, the centered 95 %-intervals, some random stress-deformation function samples and the estimated coverages for the six SS and five BT tests as well as the total estimated coverage. The GP posterior is used for data augmentation in the subsequent steps of the proposed framework.

Appendix F.2. Experimental anisotropic test case

In Fig. F.16, we show the distribution of stress-deformation functions given by the GP posterior. For the discussion of the results for the experimental anisotropic test case, we refer to Section 3.2.2.

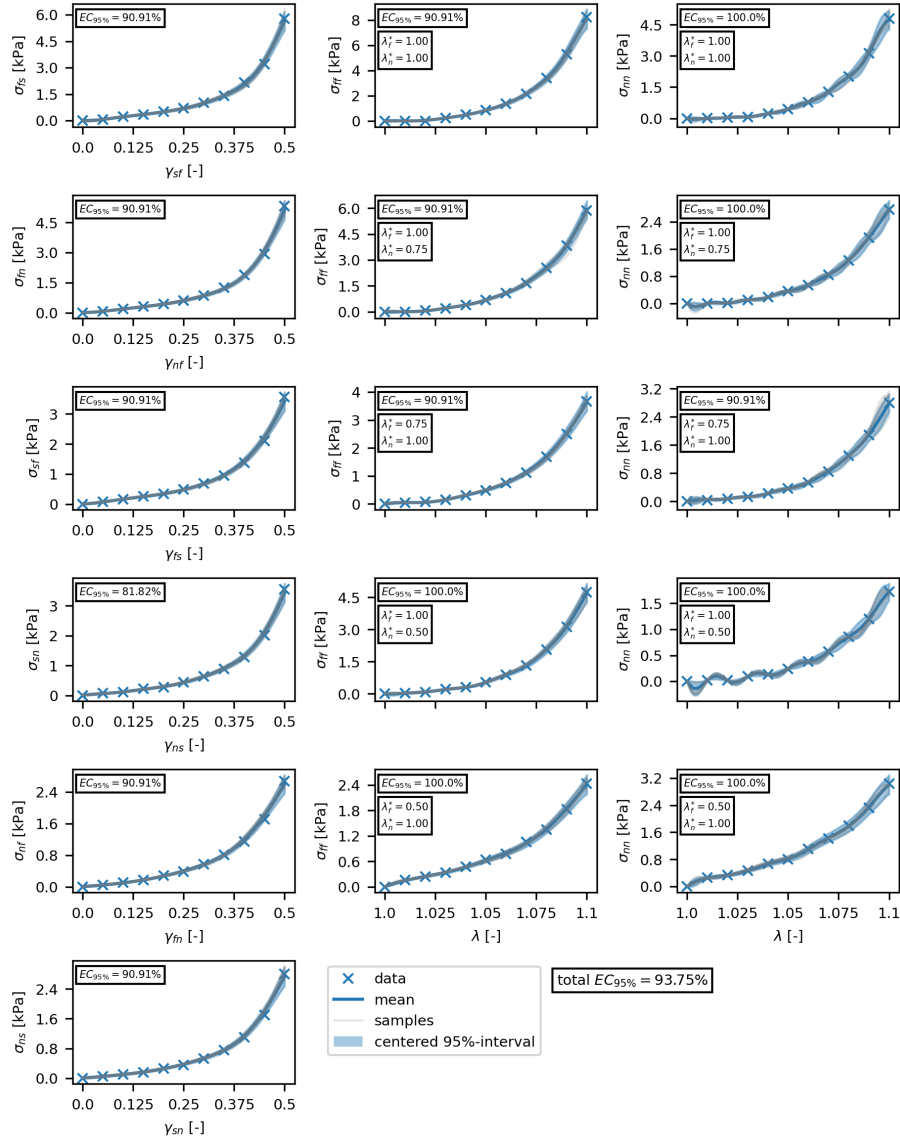


Fig. F.16: Experimental anisotropic test case: GP posterior. The illustrations show the GP posterior mean, the centered 95 %-intervals, some random stress-deformation function samples and the estimated coverages for the six SS and five BT tests as well as the total estimated coverage. The GP posterior is used for data augmentation in the subsequent steps of the proposed framework.

References

- [1] R. W. Ogden, *Non-Linear Elastic Deformations*, Ellis Horwood, Chichester, 1984.
- [2] G. A. Holzapfel, *Nonlinear Solid Mechanics: A Continuum Approach for Engineering*, 1st Edition, Wiley, Chichester, 2000.
- [3] P. Steinmann, M. Hossain, G. Possart, Hyperelastic models for rubber-like materials: consistent tangent operators and suitability for Treloar's data, *Archive of Applied Mechanics* 82 (2012) 1183–1217. doi:<https://doi.org/10.1007/s00419-012-0610-z>.
- [4] A. Ricker, P. Wriggers, Systematic Fitting and Comparison of Hyperelastic Continuum Models for Elastomers, *Archives of Computational Methods in Engineering* 30 (3) (2023) 2257–2288. doi:<https://doi.org/10.1007/s11831-022-09865-x>.
- [5] U. Römer, S. Hartmann, J.-A. Tröger, D. Anton, H. Wessels, M. Flaschel, L. De Lorenzis, Reduced and All-At-Once Approaches for Model Calibration and Discovery in Computational Solid Mechanics, *Applied Mechanics Reviews* 77 (4) (2025) 040801. doi:<https://doi.org/10.1115/1.4066118>.
- [6] M. E. Gurtin, E. Fried, L. Anand, *The Mechanics and Thermodynamics of Continua*, Cambridge University Press, Cambridge, 2010. doi:<https://doi.org/10.1017/CB09780511762956>.
- [7] M. Flaschel, S. Kumar, L. De Lorenzis, Unsupervised discovery of interpretable hyperelastic constitutive laws, *Computer Methods in Applied Mechanics and Engineering* 381 (2021) 113852. doi:<https://doi.org/10.1016/j.cma.2021.113852>.
- [8] R. S. Rivlin, Torsion of a Rubber Cylinder, *Journal of Applied Physics* 18 (5) (1947) 444–449. doi:<https://doi.org/10.1063/1.1697674>.
- [9] R. W. Ogden, Large deformation isotropic elasticity – on the correlation of theory and experiment for incompressible rubberlike solids, *Proceedings of the Royal Society of London. A. Mathematical and Physical Sciences* 326 (1567) (1972) 565–584. doi:<https://doi.org/10.1098/rspa.1972.0026>.
- [10] P. Thakolkaran, A. Joshi, Y. Zheng, M. Flaschel, L. De Lorenzis, S. Kumar, NN-EUCLID: Deep-learning hyperelasticity without stress data, *Journal of the Mechanics and Physics of Solids* 169 (2022) 105076. doi:<https://doi.org/10.1016/j.jmps.2022.105076>.
- [11] M. Flaschel, H. Yu, N. Reiter, J. Hinrichsen, S. Budday, P. Steinmann, S. Kumar, L. De Lorenzis, Automated discovery of interpretable hyperelastic material models for human brain tissue with EUCLID, *Journal*

- of the Mechanics and Physics of Solids 180 (2023) 105404. doi:<https://doi.org/10.1016/j.jmps.2023.105404>.
- [12] M. Flaschel, S. Kumar, L. De Lorenzis, Discovering plasticity models without stress data, *npj Computational Materials* 8 (91) (2022). doi:<https://doi.org/10.1038/s41524-022-00752-4>.
- [13] M. Flaschel, S. Kumar, L. De Lorenzis, Automated discovery of generalized standard material models with EUCLID, *Computer Methods in Applied Mechanics and Engineering* 405 (2023) 115867. doi:<https://doi.org/10.1016/j.cma.2022.115867>.
- [14] E. Marino, M. Flaschel, S. Kumar, L. De Lorenzis, Automated identification of linear viscoelastic constitutive laws with EUCLID, *Mechanics of Materials* 181 (2023) 104643. doi:<https://doi.org/10.1016/j.mechmat.2023.104643>.
- [15] J. N. Fuhg, G. Anantha Padmanabha, N. Bouklas, B. Bahmani, W. Sun, N. N. Vlassis, M. Flaschel, P. Carrara, L. De Lorenzis, A Review on Data-Driven Constitutive Laws for Solids, *Archives of Computational Methods in Engineering* 32 (2025) 1841–1883. doi:<https://doi.org/10.1007/s11831-024-10196-2>.
- [16] K. Linka, M. Hillgärtner, K. P. Abdolazizi, R. C. Aydin, M. Itskov, C. J. Cyron, Constitutive artificial neural networks: A fast and general approach to predictive data-driven constitutive modeling by deep learning, *Journal of Computational Physics* 429 (2021) 110010. doi:<https://doi.org/10.1016/j.jcp.2020.110010>.
- [17] D. K. Klein, M. Fernández, R. J. Martin, P. Neff, O. Weeger, Polyconvex anisotropic hyperelasticity with neural networks, *Journal of the Mechanics and Physics of Solids* 159 (2022) 104703. doi:<https://doi.org/10.1016/j.jmps.2021.104703>.
- [18] L. Linden, D. K. Klein, K. A. Kalina, J. Brummund, O. Weeger, M. Kästner, Neural networks meet hyperelasticity: A guide to enforcing physics, *Journal of the Mechanics and Physics of Solids* 179 (2023) 105363. doi:<https://doi.org/10.1016/j.jmps.2023.105363>.
- [19] J. N. Fuhg, N. Bouklas, R. E. Jones, Learning hyperelastic anisotropy from data via a tensor basis neural network, *Journal of the Mechanics and Physics of Solids* 168 (2022) 105022. doi:<https://doi.org/10.1016/j.jmps.2022.105022>.
- [20] K. A. Kalina, J. Brummund, W. Sun, M. Kästner, Neural networks meet anisotropic hyperelasticity: A framework based on generalized structure tensors and isotropic tensor functions, *Computer Methods in Applied Mechanics and Engineering* 437 (2025) 117725. doi:<https://doi.org/10.1016/j.cma.2024.117725>.

- [21] A. B. Tepole, A. A. Jadoon, M. Rausch, J. N. Fuhg, Polyconvex physics-augmented neural network constitutive models in principal stretches, *International Journal of Solids and Structures* 320 (2025) 113469. doi:<https://doi.org/10.1016/j.ijsolstr.2025.113469>.
- [22] K. Linka, E. Kuhl, A new family of Constitutive Artificial Neural Networks towards automated model discovery, *Computer Methods in Applied Mechanics and Engineering* 403 (2023) 115731. doi:<https://doi.org/10.1016/j.cma.2022.115731>.
- [23] K. Linka, S. R. St. Pierre, E. Kuhl, Automated model discovery for human brain using Constitutive Artificial Neural Networks, *Acta Biomaterialia* 160 (2023) 134–151. doi:<https://doi.org/10.1016/j.actbio.2023.01.055>.
- [24] K. Linka, A. Buganza Tepole, G. A. Holzapfel, E. Kuhl, Automated model discovery for skin: Discovering the best model, data, and experiment, *Computer Methods in Applied Mechanics and Engineering* 410 (2023) 116007. doi:<https://doi.org/10.1016/j.cma.2023.116007>.
- [25] M. Peirlinck, K. Linka, J. A. Hurtado, E. Kuhl, On automated model discovery and a universal material subroutine for hyperelastic materials, *Computer Methods in Applied Mechanics and Engineering* 418 (2024) 116534. doi:<https://doi.org/10.1016/j.cma.2023.116534>.
- [26] D. Martonová, M. Peirlinck, K. Linka, G. A. Holzapfel, S. Leyendecker, E. Kuhl, Automated model discovery for human cardiac tissue: Discovering the best model and parameters, *Computer Methods in Applied Mechanics and Engineering* 428 (2024) 117078. doi:<https://doi.org/10.1016/j.cma.2024.117078>.
- [27] M. Tacke, M. Busch, K. Bali, K. Abdolazizi, K. Linka, C. Cyron, R. Aydin, Constitutive scientific generative agent (CSGA): Leveraging large language models for automated constitutive model discovery, *Machine Learning for Computational Science and Engineering* 1 (23) (2025). doi:<https://doi.org/10.1007/s44379-025-00022-2>.
- [28] P. Thakolkaran, Y. Guo, S. Saini, M. Peirlinck, B. Alheit, S. Kumar, Can KAN CANs? Input-convex Kolmogorov-Arnold Networks (KANs) as hyperelastic constitutive artificial neural networks (CANs), *Computer Methods in Applied Mechanics and Engineering* 443 (2025) 118089. doi:<https://doi.org/10.1016/j.cma.2025.118089>.
- [29] K. P. Abdolazizi, R. C. Aydin, C. J. Cyron, K. Linka, Constitutive Kolmogorov-Arnold Networks (CKANs): Combining accuracy and interpretability in data-driven material modeling, *Journal of the Mechanics and Physics of Solids* 203 (2025) 106212. doi:<https://doi.org/10.1016/j.jmps.2025.106212>.

- [30] N. J. Linden, B. Kramer, P. Rangamani, Bayesian parameter estimation for dynamical models in systems biology, *PLOS Computational Biology* 18 (10) (2022) 1–48. doi:<https://doi.org/10.1371/journal.pcbi.1010651>.
- [31] A. Gelman, J. B. Carlin, H. S. Stern, D. B. Dunson, A. Vehtari, D. B. Rubin, *Bayesian Data Analysis*, 3rd Edition, Texts in Statistical Science, Chapman and Hall/CRC, New York, 2013. doi:<https://doi.org/10.1201/b16018>.
- [32] A. Joshi, P. Thakolkaran, Y. Zheng, M. Escande, M. Flaschel, L. De Lorenzis, S. Kumar, Bayesian-EUCLID: Discovering hyperelastic material laws with uncertainties, *Computer Methods in Applied Mechanics and Engineering* 398 (2022) 115225. doi:<https://doi.org/10.1016/j.cma.2022.115225>.
- [33] K. Linka, G. A. Holzapfel, E. Kuhl, Discovering uncertainty: Bayesian constitutive artificial neural networks, *Computer Methods in Applied Mechanics and Engineering* 433 (2025) 117517. doi:<https://doi.org/10.1016/j.cma.2024.117517>.
- [34] S. M. Hirsh, D. A. Barajas-Solano, J. N. Kutz, Sparsifying priors for Bayesian uncertainty quantification in model discovery, *Royal Society Open Science* 9 (2) (2022) 211823. doi:<https://doi.org/10.1098/rsos.211823>.
- [35] I. Melev, G. Kauermann, Position: There Is No Free Bayesian Uncertainty Quantification, *arXiv Preprint* (2025). doi:<https://doi.org/10.48550/arXiv.2506.03670>.
- [36] J. A. McCulloch, E. Kuhl, Discovering uncertainty: Gaussian constitutive neural networks with correlated weights, *Computational Mechanics* (2025). doi:<https://doi.org/10.1007/s00466-025-02660-y>.
- [37] A. Aggarwal, B. S. Jensen, S. Pant, C.-H. Lee, Strain energy density as a Gaussian process and its utilization in stochastic finite element analysis: Application to planar soft tissues, *Computer Methods in Applied Mechanics and Engineering* 404 (2023) 115812. doi:<https://doi.org/10.1016/j.cma.2022.115812>.
- [38] V. Taç, M. K. Rausch, I. Bilonis, F. S. Costabal, A. B. Tepole, Generative hyperelasticity with physics-informed probabilistic diffusion fields, *Engineering with Computers* 41 (2025) 51–69. doi:<https://doi.org/10.1007/s00366-024-01984-2>.
- [39] U. Römer, J. Liu, M. Böl, Surrogate-based Bayesian calibration of biomechanical models with isotropic material behavior, *International Journal for Numerical Methods in Biomedical Engineering* 38 (4) (2022) e3575. doi:<https://doi.org/10.1002/cnm.3575>.

- [40] E. G. Tabak, C. V. Turner, A Family of Nonparametric Density Estimation Algorithms, *Communications on Pure and Applied Mathematics* 66 (2) (2013) 145–164. doi:<https://doi.org/10.1002/cpa.21423>.
- [41] D. Rezende, S. Mohamed, Variational Inference with Normalizing Flows, in: F. Bach, D. Blei (Eds.), *Proceedings of the 32nd International Conference on Machine Learning*, Vol. 37 of *Proceedings of Machine Learning Research*, PMLR, Lille, France, 2015, pp. 1530–1538.
URL <https://proceedings.mlr.press/v37/rezende15.html>
- [42] G. Papamakarios, E. Nalisnick, D. J. Rezende, S. Mohamed, B. Lakshminarayanan, Normalizing Flows for Probabilistic Modeling and Inference, *Journal of Machine Learning Research* 22 (1) (2021) 2617–2680.
URL <https://dl.acm.org/doi/abs/10.5555/3546258.3546315>
- [43] Y. Wang, F. Liu, D. E. Schiavazzi, Variational inference with NoFAS: Normalizing flow with adaptive surrogate for computationally expensive models, *Journal of Computational Physics* 467 (2022) 111454. doi:<https://doi.org/10.1016/j.jcp.2022.111454>.
- [44] I. M. Sobol’, Global sensitivity indices for nonlinear mathematical models and their Monte Carlo estimates, *Mathematics and Computers in Simulation* 55 (1) (2001) 271–280. doi:[https://doi.org/10.1016/S0378-4754\(00\)00270-6](https://doi.org/10.1016/S0378-4754(00)00270-6).
- [45] B.-H. Tran, S. Rossi, D. Milios, M. Filippone, All You Need is a Good Functional Prior for Bayesian Deep Learning, *Journal of Machine Learning Research* 23 (1) (2022) 3210–3265.
URL <https://dl.acm.org/doi/abs/10.5555/3586589.3586663>
- [46] M. Schmidt, H. Lipson, Distilling Free-Form Natural Laws from Experimental Data, *Science* 324 (5923) (2009) 81–85. doi:<https://doi.org/10.1126/science.1165893>.
- [47] L. R. G. Treloar, Stress-strain data for vulcanised rubber under various types of deformation, *Transactions of the Faraday Society* 40 (1944) 59–70. doi:<http://dx.doi.org/10.1039/TF9444000059>.
- [48] G. Sommer, A. J. Schriefl, M. Andrä, M. Sacherer, C. Viertler, H. Wolinski, G. A. Holzapfel, Biomechanical properties and microstructure of human ventricular myocardium, *Acta Biomaterialia* 24 (2015) 172–192. doi:<https://doi.org/10.1016/j.actbio.2015.06.031>.
- [49] D. Anton, Code for the publication: Uncertainty quantification in model discovery by distilling interpretable material constitutive models from Gaussian process posteriors, code available from <https://github.com/david-anton/UQInModelDiscovery> (2025). doi:<https://doi.org/10.5281/zenodo.17442182>.

- [50] A. Paszke, S. Gross, F. Massa, A. Lerer, J. Bradbury, G. Chanan, T. Killeen, Z. Lin, N. Gimelshein, L. Antiga, A. Desmaison, A. Köpf, E. Yang, Z. DeVito, M. Raison, A. Tejani, S. Chilamkurthy, B. Steiner, L. Fang, J. Bai, S. Chintala, PyTorch: An Imperative Style, High-Performance Deep Learning Library, in: H. Wallach, H. Larochelle, A. Beygelzimer, F. d'Alché-Buc, E. Fox, R. Garnett (Eds.), *Advances in Neural Information Processing Systems*, Vol. 32, Curran Associates, Inc., Red Hook, NY, USA, 2019, pp. 1–12, software available from pytorch.org. URL https://proceedings.neurips.cc/paper_files/paper/2019/file/bdbca288fee7f92f2bfa9f7012727740-Paper.pdf
- [51] J. R. Gardner, G. Pleiss, D. Bindel, K. Q. Weinberger, A. G. Wilson, GPyTorch: Blackbox Matrix-Matrix Gaussian Process Inference with GPU Acceleration , in: S. Bengio, H. M. Wallach, H. Larochelle, K. Grauman, N. Cesa-Bianchi, R. Garnett (Eds.), *Advances in Neural Information Processing Systems*, Vol. 31, Curran Associates Inc., Red Hook, NY, USA, 2018, p. 7587–7597. URL https://proceedings.neurips.cc/paper_files/paper/2018/file/27e8e17134dd7083b050476733207ea1-Paper.pdf
- [52] V. Stimper, D. Liu, A. Campbell, V. Berenz, L. Ryll, B. Schölkopf, J. M. Hernández-Lobato, normflows: A PyTorch Package for Normalizing Flows, *Journal of Open Source Software* 8 (86) (2023) 5361. doi:<https://doi.org/10.21105/joss.05361>.
- [53] J. Herman, W. Usher, SALib: An open-source Python library for Sensitivity Analysis, *Journal of Open Source Software* 2 (9) (2017) 97. doi:<https://doi.org/10.21105/joss.00097>.
- [54] T. Iwanaga, W. Usher, J. Herman, Toward SALib 2.0: Advancing the accessibility and interpretability of global sensitivity analyses, *Socio-Environmental Systems Modelling* 4 (2022) 18155. doi:<https://doi.org/10.18174/sesmo.18155>.
- [55] N. P. Lemoine, Moving beyond noninformative priors: why and how to choose weakly informative priors in Bayesian analyses, *Oikos* 128 (7) (2019) 912–928. doi:<https://doi.org/10.1111/oik.05985>.
- [56] J.-H. Urrea-Quintero, D. Anton, L. De Lorenzis, H. Wessels, Automated constitutive model discovery by pairing sparse regression algorithms with model selection criteria, *Computer Methods in Applied Mechanics and Engineering* 449 (2026) 118551. doi:<https://doi.org/10.1016/j.cma.2025.118551>.
- [57] C. E. Rasmussen, C. K. I. Williams, *Gaussian Processes for Machine Learning*, 1st Edition, MIT Press, Cambridge, 2005. doi:<https://doi.org/10.7551/mitpress/3206.001.0001>.

- [58] I. Loshchilov, F. Hutter, Decoupled Weight Decay Regularization, in: International Conference on Learning Representations, OpenReview.net, 2019, pp. 1–8.
URL <https://openreview.net/forum?id=Bkg6RiCqY7>
- [59] W. Rudin, Real And Complex Analysis, 3rd Edition, Mathematics Series, McGraw-Hill, Inc., New York, 1987.
- [60] V. I. Bogachev, Measure Theory, 1st Edition, Springer, Berlin, 2007. doi: <https://doi.org/10.1007/978-3-540-34514-5>.
- [61] D. P. Kingma, T. Salimans, R. Jozefowicz, X. Chen, I. Sutskever, M. Welling, Improved variational inference with inverse autoregressive flow, in: D. D. Lee, M. Sugiyama, U. Von Luxburg, R. a. Guyon, Isabelle Garnett (Eds.), Advances in Neural Information Processing Systems, Vol. 29, Curran Associates Inc., Red Hook, NY, USA, 2016, p. 4743–4751.
URL https://proceedings.neurips.cc/paper_files/paper/2016/file/ddeebdeefdb7e7e7a697e1c3e3d8ef54-Paper.pdf
- [62] M. Germain, K. Gregor, I. Murray, H. Larochelle, MADE: Masked Autoencoder for Distribution Estimation, in: F. Bach, D. Blei (Eds.), Proceedings of the 32nd International Conference on Machine Learning, Vol. 37 of Proceedings of Machine Learning Research, PMLR, Lille, France, 2015, pp. 881–889.
URL <https://proceedings.mlr.press/v37/germain15.html>
- [63] V. I. Bogachev, A. V. Kolesnikov, K. V. Medvedev, Triangular transformations of measures, Sbornik: Mathematics 196 (3) (2005) 309–335. doi: <https://doi.org/10.1070/SM2005v196n03ABEH000882>.
- [64] G. Papamakarios, T. Pavlakou, I. Murray, Masked Autoregressive Flow for Density Estimation, in: I. Guyon, U. Von Luxburg, S. Bengio, H. Wallach, S. Fergus, R. Vishwanathan, R. Garnett (Eds.), Advances in Neural Information Processing Systems, Vol. 30, Curran Associates, Inc., Red Hook, NY, USA, 2017, pp. 1–10.
URL https://proceedings.neurips.cc/paper_files/paper/2017/file/6c1da886822c67822bcf3679d04369fa-Paper.pdf
- [65] L. Dinh, J. Sohl-Dickstein, S. Bengio, Density estimation using Real NVP, in: International Conference on Learning Representations, OpenReview.net, 2017, pp. 1–32.
URL <https://openreview.net/forum?id=HkpbnH91x>
- [66] R. T. Q. Chen, J. Behrmann, D. K. Duvenaud, J.-H. Jacobsen, Residual Flows for Invertible Generative Modeling, in: H. Wallach, H. Larochelle, A. Beygelzimer, F. d’Alché Buc, E. Fox, R. Garnett (Eds.), Advances in Neural Information Processing Systems, Vol. 32, Curran Associates, Inc., Red Hook, NY, USA, 2019, pp. 1–11.

- URL https://proceedings.neurips.cc/paper_files/paper/2019/file/5d0d5594d24f0f955548f0fc0ff83d10-Paper.pdf
- [67] C. Villani, *Optimal Transport: Old and New*, 1st Edition, Grundlehren der mathematischen Wissenschaften, Springer, Berlin, Heidelberg, 2009. doi:<https://doi.org/10.1007/978-3-540-71050-9>.
- [68] I. J. Goodfellow, J. Pouget-Abadie, M. Mirza, B. Xu, D. Warde-Farley, S. Ozair, A. Courville, Y. Bengio, Generative Adversarial Nets, in: Z. Ghahramani, M. Welling, C. Cortes, N. Lawrence, W. K. Q. (Eds.), *Advances in Neural Information Processing Systems*, Vol. 27, Curran Associates, Inc., Red Hook, NY, USA, 2014, pp. 1–9. URL https://proceedings.neurips.cc/paper_files/paper/2014/file/f033ed80deb0234979a61f95710dbe25-Paper.pdf
- [69] M. Arjovsky, S. Chintala, L. Bottou, Wasserstein Generative Adversarial Networks, in: D. Precup, Y. W. Teh (Eds.), *Proceedings of the 34th International Conference on Machine Learning*, Vol. 70 of *Proceedings of Machine Learning Research*, PMLR, Sydney, Australia, 2017, pp. 214–223. URL <https://proceedings.mlr.press/v70/arjovsky17a.html>
- [70] I. Gulrajani, F. Ahmed, M. Arjovsky, V. Dumoulin, A. C. Courville, Improved Training of Wasserstein GANs, in: I. Guyon, U. Von Luxburg, S. Bengio, H. Wallach, R. Fergus, S. Vishwanathan, R. Garnett (Eds.), *Advances in Neural Information Processing Systems*, Vol. 30, Curran Associates, Inc., Red Hook, NY, USA, 2017, pp. 1–11. URL https://proceedings.neurips.cc/paper_files/paper/2017/file/892c3b1c6dcd52936e27cbd0ff683d6-Paper.pdf
- [71] T. Miyato, T. Kataoka, M. Koyama, Y. Yoshida, Spectral Normalization for Generative Adversarial Networks, in: *International Conference on Learning Representations*, OpenReview.net, 2018, pp. 1–26. URL <https://openreview.net/forum?id=B1QRgziT->
- [72] A. Saltelli, Making best use of model evaluations to compute sensitivity indices, *Computer Physics Communications* 145 (2) (2002) 280–297. doi:[https://doi.org/10.1016/S0010-4655\(02\)00280-1](https://doi.org/10.1016/S0010-4655(02)00280-1).
- [73] A. Saltelli, P. Annoni, I. Azzini, F. Campolongo, M. Ratto, S. Tarantola, Variance based sensitivity analysis of model output. Design and estimator for the total sensitivity index, *Computer Physics Communications* 181 (2) (2010) 259–270. doi:<https://doi.org/10.1016/j.cpc.2009.09.018>.
- [74] J. N. Fuhg, R. E. Jones, N. Bouklas, Extreme sparsification of physics-augmented neural networks for interpretable model discovery in mechanics, *Computer Methods in Applied Mechanics and Engineering* 426 (2024) 116973. doi:<https://doi.org/10.1016/j.cma.2024.116973>.

- [75] M. P. Wollner, M. Rolf-Pissarczyk, G. A. Holzapfel, A reparameterization-invariant Bayesian framework for uncertainty estimation and calibration of simple materials, *Computational Mechanics* (2025). doi:<https://doi.org/10.1007/s00466-024-02573-2>.
- [76] L. R. G. Treloar, *The Physics of Rubber Elasticity*, 3rd Edition, Oxford Classic Texts in the Physical Sciences, Oxford University Press, Oxford, 2005. doi:<https://doi.org/10.1093/oso/9780198570271.001.0001>.
- [77] E. M. Arruda, M. C. Boyce, A three-dimensional constitutive model for the large stretch behavior of rubber elastic materials, *Journal of the Mechanics and Physics of Solids* 41 (2) (1993) 389–412. doi:[https://doi.org/10.1016/0022-5096\(93\)90013-6](https://doi.org/10.1016/0022-5096(93)90013-6).
- [78] M. Tosaka, S. Kohjiya, Y. Ikeda, S. Toki, B. S. Hsiao, Molecular orientation and stress relaxation during strain-induced crystallization of vulcanized natural rubber, *Polymer Journal* 42 (6) (2010) 474–481. doi:<https://doi.org/10.1038/pj.2010.22>.
- [79] J. A. McCulloch, S. R. St. Pierre, K. Linka, E. Kuhl, On sparse regression, Lp-regularization, and automated model discovery, *International Journal for Numerical Methods in Engineering* 125 (14) (2024) e7481. doi:<https://doi.org/10.1002/nme.7481>.
- [80] S. Hartmann, R. R. Gilbert, Identifiability of material parameters in solid mechanics, *Archive of Applied Mechanics* 88 (1) (2018) 3–26. doi:<https://doi.org/10.1007/s00419-017-1259-4>.
- [81] J. Vaverka, J. Burša, A modification of Holzapfel–Ogden hyperelastic model of myocardium better describing its passive mechanical behavior, *European Journal of Mechanics - A/Solids* 111 (2025) 105586. doi:<https://doi.org/10.1016/j.euromechsol.2025.105586>.
- [82] A. L. Brown, J. Liu, D. B. Ennis, A. L. Marsden, Cardiac mechanics modeling: recent developments and current challenges, *arXiv Preprint* (2025). doi:<https://doi.org/10.48550/arXiv.2509.07971>.
- [83] G. A. Holzapfel, R. W. Ogden, Constitutive modelling of passive myocardium: a structurally based framework for material characterization, *Philosophical Transactions of the Royal Society A: Mathematical, Physical and Engineering Sciences* 367 (1902) (2009) 3445–3475. doi:<https://doi.org/10.1098/rsta.2009.0091>.
- [84] N. Laita, M. A. Martínez, M. Doblaré, E. Peña, On the myocardium modeling under multimodal deformations: a comparison between costa’s, Holzapfel and Ogden’s formulations, *Meccanica* 60 (8) (2025) 2291–2324. doi:<https://doi.org/10.1007/s11012-025-01959-7>.

- [85] S. Dokos, B. H. Smail, A. A. Young, I. J. LeGrice, Shear properties of passive ventricular myocardium, *American Journal of Physiology-Heart and Circulatory Physiology* 283 (6) (2002) H2650–H2659. doi:<https://doi.org/10.1152/ajpheart.00111.2002>.
- [86] B. Owen, N. Bojdo, A. Jivkov, B. Keavney, A. Revell, Structural modelling of the cardiovascular system, *Biomechanics and Modeling in Mechanobiology* 17 (5) (2018) 1217–1242. doi:<https://doi.org/10.1007/s10237-018-1024-9>.
- [87] D. Martonová, S. Leyendecker, G. A. Holzapfel, E. Kuhl, Discovering dispersion: How robust is automated model discovery for human myocardial tissue?, *Biomechanics and Modeling in Mechanobiology* (2025). doi:<https://doi.org/10.1007/s10237-025-02005-x>.
- [88] I. Ustyuzhaninov, I. Kazlauskaitė, C. H. Ek, N. Campbell, Monotonic Gaussian Process Flows, in: S. Chiappa, R. Calandra (Eds.), *Proceedings of the Twenty Third International Conference on Artificial Intelligence and Statistics*, Vol. 108 of *Proceedings of Machine Learning Research*, PMLR, online, 2020, pp. 3057–3067.
URL <https://proceedings.mlr.press/v108/ustyuzhaninov20a.html>
- [89] V. Narouie, H. Wessels, F. Cirak, U. Römer, Mechanical state estimation with a Polynomial-Chaos-Based Statistical Finite Element Method, *Computer Methods in Applied Mechanics and Engineering* 441 (2025) 117970. doi:<https://doi.org/10.1016/j.cma.2025.117970>.
- [90] T. Tieleman, G. Hinton, Lecture 6.5-rmsprop: Divide the Gradient by a Running Average of Its Recent Magnitude, online, COURSERA: Neural Networks for Machine Learning, 4, 26-31 (2012).